

**Photonic crystal intermediate reflective layer
for micromorph tandem solar cells**

Dissertation

zur Erlangung des akademischen Grades
doctor rerum naturalium (Dr. rer. nat.)

vorgelegt der

Mathematisch-Naturwissenschaftlich-Technischen Fakultät
(mathematisch-naturwissenschaftlicher Bereich)
der Martin-Luther-Universität Halle-Wittenberg

von

Herrn Dipl. Phys. Andreas Bielawny
(geboren am 30. März 1979 in Paderborn)

angefertigt an der

Martin-Luther-Universität Halle-Wittenberg,
06120 Halle (Saale), Germany

und der

Universität Paderborn,
33098 Paderborn, Germany

Gutachter:

Herr Prof. Dr. R. B. Wehrspohn, Universität Halle
Herr Prof. Dr. H. Gräner, Universität Halle
Herr Prof. Dr. U. Rau, Forschungszentrum Jülich

Vorgelegt am: 2. Juni 2009

Verteidigung am: 9. Juli 2009

To Anna

You spin the sun around
And the stars will all come out

Whosoever wishes to know about the world
must learn about it in its particular details.

Heraclitus, ~ 500 BC

Contents

1	Introduction	1
1.1	Introduction to photovoltaics	1
1.1.1	Photovoltaic cells	1
1.1.2	Interaction of radiation with matter	3
1.1.3	Efficiency of photovoltaic power conversion	4
1.1.4	Improvement of efficiency	8
1.1.5	Thin-film silicon tandem cells	11
1.1.6	Micromorph silicon tandem cell	14
1.2	Intermediate reflectors	15
1.2.1	Current state-of-the-art in intermediate reflectors	16
1.3	Introduction to photonic crystals	17
1.3.1	The photonic master equations	17
1.3.2	1D photonic crystals	19
1.3.3	Effective medium	20
1.3.4	Structure of opaline photonic crystals	21
1.3.5	Photonic bandstructure of opaline PhC	25
1.3.6	Optical properties of artificial opals	27
1.4	Aim of this thesis and IRL requirements	30
1.4.1	Classification of the proposed enhancement	30
1.4.2	Requirements of the photonic intermediate reflective layer	31
2	Experimental and numerical methods	33
2.1	Optical methods	33
2.1.1	Microscopy	33
2.1.2	Spectroscopy	33
2.1.3	NSOM	34
2.2	Scanning electron microscopy	34
2.3	Preparation methods	35
2.3.1	Vertical deposition	35
2.3.2	Knife coating	36
2.3.3	Replication method: ALD, CVD	37
2.3.4	Wet chemical methods	38
2.4	Simulation methods	38
2.4.1	Plane wave	38
2.4.2	RCWA, FMM	39
2.4.3	Scattering matrix method	40
3	Results	41
3.1	Numerical simulation of 3D photonic crystal IRL	41

3.1.1	Bandstructure calculation of 3D inverted opal PhC	41
3.1.2	Simulation of optical properties of inv. opal IRL	49
3.1.3	Top cell calculation: towards enhancement	53
3.1.4	3D PhC IRL enhancement potential	56
3.1.5	Tandem cell calculation: towards current matching	58
3.2	Fabrication of the photonic crystal IRL	63
3.2.1	Developed technical solutions	63
3.2.2	Thin-film samples from rapid opal layer assembly setup	64
3.2.3	Template removal	64
3.2.4	Size parameters	65
3.3	Structural investigation	66
3.3.1	Structural disorder in opal samples	66
3.3.2	Drying cracks	66
3.3.3	Inverted opals	68
3.4	Optical characterization	71
3.4.1	Reflectance of thin-film PHC samples	71
3.4.2	Reflectivity vs. crystal thickness	72
3.4.3	Angular spectroscopy: Bragg reflection	74
3.4.4	Optical thin-film properties and effective index	79
3.4.5	Impact of disorder in opal thin-films	81
3.4.6	NSOM	82
3.5	Electrical characterization	84
3.5.1	Electrochemical impedance spectroscopy	84
3.6	Integration into thin-film solar cell	88
3.6.1	Transmission through the PhC to solar cell absorber	88
3.6.2	Integration on thin-film top-cell	89
4	Discussion	93
4.1	Comparison with other IRL concepts	93
4.1.1	Numerical comparison of different intermediate reflectors	93
4.1.2	Comparison with state-of-the-art IRL	95
4.2	IRL properties & fabrication methods	97
4.2.1	Properties in numerical analysis: coating thickness	97
4.2.2	Spectral positions in simulations and experiment	97
4.2.3	Imperfections of the inverted opal IRL	99
4.2.4	Electrical resistivity	99
4.2.5	Materials and processes: technology transfer	100
4.3	Compatibility with textured substrates: roughness	101
4.4	The prototype	102
4.5	Compliance of results with requirements	103
5	Summary	105
6	Outlook	107
A	Acknowledgements	i
B	Optical Properties: Technical Details	iii

B.1 Measured amplitudes of reflection	iii
B.2 Effects of numerical aperture	iii
B.3 Reflectance and transmittance	iv
C Publications and Presentations	v
C.1 Publications related to this thesis	v
C.2 Selected talks and posters	vi
D Curriculum Vitae	vii
E Eidesstattliche Erklärung	ix
Bibliography	xi

Zusammenfassung

Ziel dieser Arbeit ist die Untersuchung und Herstellung einer optischen Zwischenschicht für Tandemsolarzellen aus Silizium. Eine Wirkungsgradsteigerung der Vorderzelle soll durch gezielte Rückreflexion von Photonen mit spektral begrenzter Wellenlängenverteilung erreicht werden. Das Funktionsprinzip dieser Schicht basiert auf der Physik der photonischen Kristalle und ihren Möglichkeiten, die Ausbreitung von Licht in bestimmten Spektralbereichen und Raumwinkeln zu beeinflussen und zu unterdrücken. Unter Verwendung verschiedener numerischer Verfahren werden Berechnungen zur Ermittlung der benötigten spezifischen Eigenschaften einer solchen Schicht durchgeführt. Die zu erwartenden optischen Eigenschaften endlicher Kristallschichten werden simuliert und mit experimentellen Ergebnissen verglichen. Zu erwartende Wirkungsgradsteigerungen für die Solarzelle und mögliche Arbeitsparameter der Zwischenschicht werden ermittelt. Eine 3D photonische Zwischenreflektorschicht wird als invertierter Opal experimentell hergestellt und optisch und elektrisch charakterisiert. Hierzu benötigte Verfahren werden weiterentwickelt. Die Realisierung einer integrierten photonischen Reflektorschicht auf der Rückseite einer amorphen Siliziumsolarzelle ist erfolgt und erste Untersuchungen der Struktur und der externen Quanteneffizienz werden ausgeführt. Die Kombination von selbstorganisierenden Opalkristallen und rauen Solarzellenoberflächen wird experimentell untersucht.

Abstract

The aim of this work is the investigation and experimental realization of an optical interlayer for silicon tandem solar cells. The spectrally selective back reflection of photons into the front cell is being used to achieve an enhancement of efficiency in the front cell. The operation of this layer is based on the physics of photonic crystals and their potential of molding the flow and inhibiting the propagation of light in certain spectral and spatial domains. Using various numerical methods, requirements for this interlayer are being elucidated, optical properties of finite crystal thin-films are being simulated and compared to experimental results. Expected enhancements of the top cell and possible modes of operation of the photonic interlayer are obtained. A 3D photonic inverted opal intermediate reflector is fabricated and characterized optically and electrically. The realization of an integrated photonic layer on an amorphous silicon solar cell is carried out and first investigations of such device and its quantum efficiency are performed. A combination of randomly rough textured solar cell surfaces and self-organized artificial opals is being approached experimentally.

1 Introduction

1.1 Introduction to photovoltaics

From the beginning, photovoltaics has been both - a field of fundamental research and a promising field of applications for electrical power generation. It is capable of providing a significant share of our energy needs today and in the future. It has become an applied field of research and development, where cost efficiency and practical considerations have also entered the scientific scope. It has developed into serious business, with millions of cells and modules sold and new investments in fabrication facilities and production capacity every year. As a consequence of decreasing cost, photovoltaic solar power generation has become affordable for many households worldwide. This has led to an increased interest in this technology - and in the science behind it.

Literature on the basic principles of photovoltaics has been written, for example, by Würfel[1], Green[2] and Luqué[3].

The first chapter briefly describes the basics of photovoltaic energy conversion which will be helpful for a thorough understanding of this thesis, starting with an overview of the available PV technology. It introduces the different processes and efficiencies of the photovoltaic energy conversion. Particular emphasis is laid upon the so-called micromorph (silicon) tandem cell. This photovoltaic thin-film device, its limitations and potential, are the basis for the work presented in this thesis. I also introduce the principles of such tandem cells and the enhancements of efficiency that they offer. In particular, I describe the concept of intermediate filters between the two separate cells of a tandem. This leads towards the main issue of this thesis: the use of novel energy-selective photonic structures. Important requirements of such intermediate filters are deduced that lead through to the process of design and fabrication later.

1.1.1 Photovoltaic cells

The variety of available PV absorber materials and cell concepts on the market and in the laboratories is vast. After the exponential growth of sales and production of PV modules in recent years, the research for new concepts has increased. Next to high efficiencies, solar cell development aims for production of cheaper modules. Figure 1.1 shows photographs of four types of silicon cells and one organic device¹.

¹images: (1-3) Westermann & Wörner GmbH; (4) FhG ISE, Freiburg; (5) Bosch/Heliatek

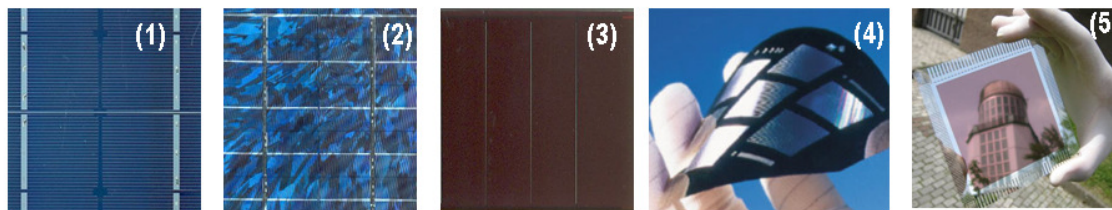


Figure 1.1: Photographs of different cells: (1) mono crystalline Si, (2) multi/poly crystalline Si, (3) amorphous Si, (4) crystalline thin Si and (5) organic material.

With Green's classification of first, second and third generation PV solar cells, we can address them as bulk (1st gen.) and thin-film (2nd gen.) cells from a technological point of view. This leaves the wide range of novel approaches (3rd gen) to more detailed terminology. While 1st generation cells are pushing towards the limits of single-junction efficiency with wafers as thin as 40 microns, 2nd generation cells aim at a minimized cost-per-power ratio. Beyond these issues, everything is considered 3rd generation. Concepts and technologies within this classification are exemplified in Tab. 1.1.

1st Generation	crystalline silicon cells <i>Czochalski, float-zone, multicryst.</i>
2nd Generation	thin-film cells a-Si, μ c-Si, CdTe, CIS, CIGS, CSG
3rd Generation	high efficiency devices \sim limits above $\eta = 30\%$ <i>tandems, spectrum splitting, thermo PV, hot carriers, intermediate band gaps</i>

Tab.1.1: Classification by generations of celltypes and their technological realisation.

Bulk silicon cells dominate the market due to their well established technology. Module efficiencies reach values of about 20% with monocrystalline cells but the average module efficiency on the German market in 2007 is 13.0% for crystalline silicon (mono, multi). The average thin-film module efficiency is about 6.3%, with CdTe dominating². An overview of thin-film technologies has been reported by Forschungszentrum Jülich in 2003 [4]. Silicon-based thin-film solar cells are made of amorphous (a-Si) and microcrystalline (μ c-Si) modules or the silicon is crystallized on glass (CSG). Gallium arsenide (GaAs) cells, cadmium telluride (CdTe) and copper-indium-(di)selenide (CIS) are also thin-film cells with industrial fabrication technology. Every technology has special properties: modules made of CdTe offer for example the best cost effectiveness, while a-Si has advantages in low illumination areas or areas with less direct irradiation.

Among the third generation concepts, especially III/V tandem and triple cells are used for space applications, where the watt per weight ratio of components is much more important than the pure cost of a device. They contain the rare element gallium, and are too expensive for large areas. However, 2D tracked concentrator arrays are used in terrestrial

²from correspondence with Prof. G. Willeke, Fraunhofer CSP

solar plants [5], for example fabricated by Concentrix Solar. Current certified world-record cells in 2007 are III/V multi-junction cells, the reported 40% cell was fabricated by Spectrolab and achieved 40.7% at 240 suns [6].

The model system addressed within the scope of this thesis is the ‘micromorph’ thin-film silicon tandem cell: a 2nd generation (thin-film) cell that uses the 3rd generation tandem concept (see section 1.1.4) to achieve higher efficiencies at promising cost effectiveness. Because of its importance for the presented work, this cell type is discussed separately and in more detail in section 1.1.6 of this chapter.

1.1.2 Interaction of radiation with matter

Some basic terminology of the interaction between photons in the Tera hertz spectral range and matter that is likely to be used in PV technology is being treated briefly in this section. The probability of **absorption** for a photon is characterized by the absorption coefficient $\alpha(h\nu)$ (with $0 \leq \alpha \leq \sim 10^6 \text{ cm}^{-1}$), being typically a function of the photon energy. Lambert-Beer’s law (1.1) states the transmitted part of light (ratio of intensities) through a medium which is called the transmittance, T :

$$T = \frac{I_1}{I_0} = \exp(-\alpha x) \quad (1.1)$$

I_0 and I_1 are the intensities before and after passing through the material of thickness x . Dependent on the material, α can be a function of concentration (e.g. mol^{-1}) or of cross-section character (e.g. for gases). The term $A = -\ln I_1/I_0 = \alpha d$ is describing the absorbance A of incident radiation. This neglects all other effects on the transmitted intensities. From calibrated half space measurements of reflectance R and transmittance T , conclusions on A are possible for certain systems, as all light is collected and contributes to the measurement. For specularly measured R and T , which are influenced by unquantified scattering S (diffracted and scattered intensity ratios) in back and forward directions, it is convenient to use the term extinction X instead of absorbance:

$$A + S = X = 1 - R - T = 1 - R - \exp(-\alpha d) \quad (1.2)$$

Unfortunately the term ‘extinction’ is also widely used for the expression $-\ln(T)$ equal to ‘absorbance’, so $X = 1 - R - T$ can be addressed as ‘absorbance’ for clarity.

Reflection at an optical interface was described by Fresnel in 1821 in his theory of reflection, refraction and polarization for transparent and isotropous media, even for the general case of non normal incidence. For the case of a planar interface from n_1 to n_2 , the Fresnel equations Eq.(1.3) express the reflectance R for a dielectric interface, distinguishing between s- and p-polarization.

$$\begin{aligned} R_s &= \left(\frac{n_1 \cos(\Theta_1) - n_2 \cos(\Theta_2)}{n_1 \cos(\Theta_1) + n_2 \cos(\Theta_2)} \right)^2 \\ R_p &= \left(\frac{n_1 \cos(\Theta_2) - n_2 \cos(\Theta_1)}{n_1 \cos(\Theta_2) + n_2 \cos(\Theta_1)} \right)^2 \end{aligned} \quad (1.3)$$

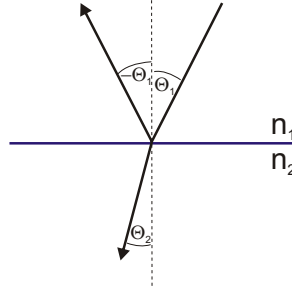


Figure 1.2: Interface of refractive indices n_1 , n_2 with light incident from n_1 .

Reflectance is the fraction of incident radiation intensity that is reflected. In case of p-polarization, the electric field is parallel to the sketched plane. S-polarized light is perpendicular to it, thus always parallel to the interface and independent of the angles. Mixed polarized light averages over both polarizations via $R = 1/2 (R_s + R_p)$.

Scattering is the deviation from a proposed propagation trajectory and is caused by non-uniformities of a medium, e.g. a particle in free space. Besides the fundamental processes of conservation of energy and momentum, the optical scattering knows different mechanisms like Mie- and Rayleigh-scattering. Within this thesis, scattering has only been considered as the above mentioned contribution to measurements of absorptance and to identify structural peculiarities in dark-field microscopy.

1.1.3 Efficiency of photovoltaic power conversion

The fundamental limits are the same for any solar power conversion. From thermodynamics, the Carnot-efficiency yields with 95% as an upper limit η_{\max} , while several loss mechanisms and conversion efficiencies significantly reduce the resulting value for η_{\max} . In order to describe the basic principles for the supply of electrical power from incident sunlight, the processes and their particular efficiencies have to be discussed. The absorption of solar irradiation in a semiconductor PV cell and the generation of mobile electrical charge carriers, will be followed by thermalization of electrons and holes. With the conversion efficiency of the electrochemical energy of generated charge pairs to usable electrical power and the extraction efficiency of this power from the cell as an electrical device, these processes sum up to the four separate loss mechanisms.

The efficiency of a solar cell is the ratio of extractable electrical power P_{el} and incident energy flux $J_{E,inc}$ from the sun.

$$\eta = \frac{P_{el}}{J_{E,inc}} = \frac{-V_{mp} j_{mp}}{\int_0^{\infty} \hbar\omega dj_{\gamma,sun}} \quad (1.4)$$

The total efficiency is the product of the efficiencies of absorption (η_{abs}), thermalization (η_{tn}), thermodynamic conversion from chemical to electrical energy (η_{td}) and the fill factor

FF.

$$\begin{aligned}\eta &= \eta_{abs} \cdot \eta_{tn} \cdot \eta_{td} \cdot FF \\ \eta &= \frac{j_{E,abs}}{j_{E,inc}} \cdot \frac{\langle \epsilon_e + \epsilon_h \rangle}{\langle \hbar\omega_{abs} \rangle} \cdot \frac{q_e V_{oc}}{\langle \epsilon_e + \epsilon_h \rangle} \cdot \frac{-j_{mp} V_{mp}}{j_{sc} V_{oc}} = \frac{-j_{mp} V_{mp}}{j_{E,inc}}\end{aligned}\quad (1.5)$$

Herein is $j_{E,inc}$ the energy flux incident on the solar cell, $\langle \epsilon \rangle$ the mean values of energy of e^-/h^+ (in nomenclature of Würfel [1]) and the mean absorbed radiation is $\langle \hbar\omega_{abs} \rangle$. The j_{mp} and V_{mp} are current and voltage, respectively at the point of maximum power, while j_{sc} and V_{oc} are the short-circuit current and open-circuit voltage. For a high-efficiency silicon cell of 20 μm thickness[7], values for conversion processes are: $\eta_{abs}=74\%$, $\eta_{thermal}=67\%$, $\eta_{thermodyn}=64\%$, $\eta_{FF}=89\%$. These processes will be discussed in the following sections. Silicon thin-film cells are addressed in Detail in section 1.6.

Absorption efficiency (η_{abs})

Semiconductors absorb only photons with energy larger than their electronic band gap, $h\nu \geq E_g$. Photons of lower energy are not absorbed and the material is transparent for $h\nu < E_g$ (see Fig.1.3).

During absorption of a photon, the inner photo effect occurs: the radiation energy is used to separate a pair of charge carriers, electron and hole (e^-/h^+). The different signs of their electrical charges lead to a strong ambition to recombine and the generated charge carriers recombine after their lifetime τ . A characteristic property of PV materials is the diffusion length for electrons and holes $L_{e,h} = \sqrt{D_{e,h}\tau_{e,h}}$, with $D_{e,h}$ being the diffusion constant of electrons or holes respectively. A large diffusion length allows thick absorbers and promises low recombination rates. The thickness should be larger than the reciprocal absorption coefficient α^{-1} . In some cell types like organic cells or the amorphous silicon cell, the poor diffusion length limits the thickness of cells to reasonable values. As a rule of thumb, the diffusion length for minority carriers must be larger than the thickness of the cell, in order to build a diffusion driven solar cell. In consequence, electrical drift is used to carry mobile charge carriers across the intrinsic semiconductor layers in amorphous silicon cells or organic cells, reducing the fillfactor (1.2.8). The absorption efficiency of Eq.(1.6) is dependent of E_g and it is strongly influenced by the technological aspects of light collection.

$$\eta_{abs} = \frac{j_{E,abs}(E_g)}{j_{E,inc}}\quad (1.6)$$

Thermalization efficiency (η_{th})

Initially, the energy of photo-generated e^-/h^+ pairs corresponds to the energy of the photon. Photon energies higher than the band gap of the absorber will thus generate ‘hot’ carriers with excess energy after absorption. The process of thermalization is the sum of all phonon generating interactions between the cell’s atomic lattice and the iniatially ‘hot’ charge carriers. They distribute their kinetic energy to the atomic lattice of the cell, cooling down to a state near $E_{kin} = 3/2 k_B T$. The duration of this process is

1 Introduction

short ($\sim 10^{-12}s$), compared with the e^-/h^+ lifetime in semiconductors. The important temperature is the lattice temperature (the temperature of the cell, assumed equal or close to the ambient temperature) in contrast to the much higher temperature of the sun. The efficiency of thermalization as denoted in Eq.(1.7) is defined by the ratio of average electrochemical energy of the charge pairs after thermalization by their mean energy directly after generation by absorption of radiation:

$$\eta_{tn} = \frac{\langle \epsilon_e + \epsilon_h \rangle}{\langle \hbar\omega_{abs} \rangle} \quad (1.7)$$

Band gap dependence (η_{abs} , η_{th})

The electronic band gap E_g has great influence on the efficiency. It determines the cut-off from a spectrum, the part of the solar spectrum that is visible to a solar cell. It decides about the spectral onset of absorption and the average energy of absorbed photons. Thus, it has direct influence on current and voltage of a cell.

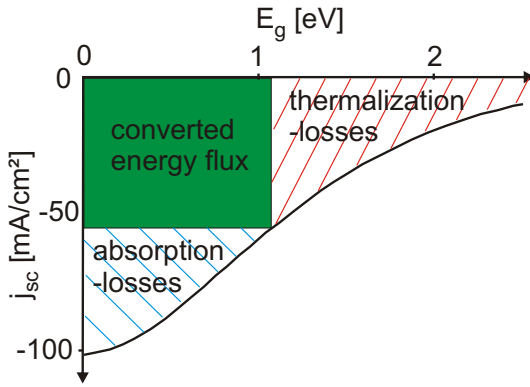


Figure 1.3: j_{sc} as a function of E_g : losses of absorption and thermalization are defined.

In figure 1.3, the dependence of j_{sc} on E_g is plotted[1]. The cell is illuminated with a 5800K black body spectrum. The silicon band gap of 1.12eV covers the rectangular area of the absorbed ratio of the full spectrum. Here, the theoretical efficiency of the Si cell would be 42%, assuming $\eta_{td} \cdot \eta_{ff} = 1$, $T_{cell} = 0 K$ and concentration (Shockley-Queisser: $\eta_u = 40.8\%$). E_g discriminates between the fundamental losses of absorption and thermalization.

Higher band gap energy of the material leads to higher voltage of the solar cell but also to lower currents as a larger fraction of the spectrum is lost: see Eq.(1.8).

$$\eta_u = E_g \cdot \int_{E_g}^{\infty} dj_{\gamma,abs}(\hbar\omega) \cdot \left(\int_0^{\infty} \hbar\omega dj_{\gamma,S}(\hbar\omega) \right)^{-1} \quad (1.8)$$

When Shockley and Queisser defined the *ultimate efficiency* of about 31% [8] for (grey body) single-junction cells in 1961 they assumed a step function in absorbance (0..1) at E_g , with a voltage of $V_{oc} \approx 0.65 E_g/q_e$.

Electro-chemical conversion efficiency (η_{td})

The third process is the conversion of the chemical energy of electrons and holes into electrical energy that can be extracted from the device. Therefore, it is necessary to quickly separate the charges spatially, to prevent recombination, radiative and non-radiative. This separation is provided by the built-in potential.

The thermodynamic efficiency quantifies the conversion from mean energy $\langle \epsilon_e + \epsilon_h \rangle$ of the charge carrier pairs to electrical energy $q_e V_{oc}$:

$$\eta_{td} = \frac{q_e V_{oc}}{\langle \epsilon_e + \epsilon_h \rangle} \quad (1.9)$$

Electrical limits - the fill factor (FF)

Each photovoltaic cell is an electric device characterized by its open circuit voltage (V_{oc}) and its short-circuit current (j_{sc}). Their values can be obtained directly in measurements, the product P_0 is the theoretical power of a lossless electrical device. A negative sign of j_{sc} defines that the cell is an electrical power source. PV cells are diodes and possess diode I-V characteristics, the saturation current density j_{sp} obeys Eq.(1.10).

$$V_{oc} = \frac{k_B T}{q_e} \ln \left(\frac{j_{sc}}{j_{sp}} - 1 \right) \quad (1.10)$$

$$j = j_{sp} \left(\exp \left(\frac{eU}{nk_B T} \right) - 1 \right) + j_{sc} \quad (1.11)$$

Here, n introduces the diode ideality factor of the cell. A small magnitude of j_{sp} is essential for a high voltage. Its influence becomes larger for small band gap energies and depends on voltage and temperature as it is not driven by optically generated charges but only by thermally generated ones. The extracted power is the rectangular area in Fig. 1.4 spanned up by the maximum power point (mpp).

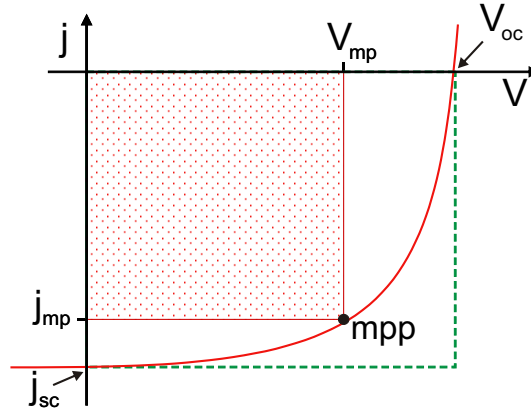


Figure 1.4: Schematic I-V characteristic of a solar cell: the mpp defines the maximum efficiency for extraction of electrical energy from the cell.

The fill factor (FF) is the ratio of the area covered by this rectangle and the area of the curve, as shown in Eq.(1.12).

$$FF = \frac{j_{mp} V_{mp}}{j_{sc} V_{oc}} \quad (1.12)$$

A typical value of the FF is about 63% for a-Si:H cells or 71% in a micromorph tandem.

External quantum efficiency

The ratio of the generated additional charge carriers in the PV cell per absorbed photons is called the quantum efficiency (QE). If the current (j_{sc}) is measured externally, it is called external quantum efficiency (EQE). This EQE of an ideal cell would be a step-function, while a realistic EQE contains the losses that take place during energy conversion and affect the current (see Fig. 1.5). Note, the EQE does not contain losses from thermalization or the difference between band gap voltage (E_g/q_e) and output voltage. These effects are not included in the bare photon and charge currents.

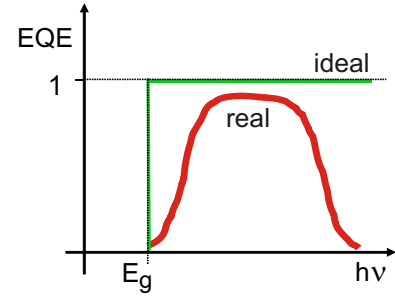


Figure 1.5: ideal/real EQE

The EQE can be measured directly with a known spectral intensity distribution - or relatively when compared to a calibrated detector of documented sensitivity. It is a function of the photon energy $h\nu$ as shown in Fig. 1.5

1.1.4 Improvement of efficiency

Any efficiency improvement of PV solar cells starts at one or more of the above mentioned losses. So-called third generation approaches discuss hot-carriers, up- and down-conversion [9] [10], multi-junction devices, intermediate bands or Bragg-stack filters in III/V cells for space applications [11]. Possible approaches for enhancement of absorption and thermalization efficiency of PV systems are shown in Tab.1.2.

	Electron management	Photon management
Thermalization	Hot carriers Tandem cells	'Quantum-cutting' -downconversion
Absorption	Intermediate bands Tandem cells	Up-conversion

Tab.1.2: Improvement of the efficiency by advanced photonic and electron designs.

Tandem cells are treated in more detail in the following section. The photon conversion approaches are also touching the scope of this thesis because they can be combined with intermediate filters as soon as highly efficient materials become available. Therefore, they will also be briefly addressed here.

Conversion of photons with energies below the onset of absorption of a cell into the absorption range is called up-conversion. Conversion of photons that possess too much energy into the absorption range is called down-conversion. Converters do not directly change the properties of the solar cell they are attached to. They alter the irradiance on the absorber and thus increase the efficiency. Fundamental limits of down-conversion and up-conversion have been shown by Trupke [9, 10]. Possible materials are rare earth doped

glasses or transparent ceramics as suggested by Ahrens[12] (up, down), novel dyes for fluorescent collectors (down) or quantum dots (down). Down-conversion essentially forces thermalization losses to take place somewhere else, other than in the solar cell - which improves the spectral answer of the PV system in blue and UV range. Up-converters extend the spectral sensitivity range below the band gap, also directly increasing the photocurrent. Within down-conversion, the conversion of a single high energy photon down to two (or more) low energy photons is called quantum-cutting. The quantum efficiencies of such a process are therefore limited by 200% or 300% for two- or three-photon processes.

Tandem cells: the multigap advantage

Tandem cells are a third generation approach to enhance the efficiency above the single-junction limit. The expression ‘tandem’ is widely used for all multi-junction cells, independent of the number of junctions or absorbers. ‘Tandem’ also refers to a two-junction device, while ‘triple’ defines a three-junction cell. As stated in Tab. 1.1, any multi-junction device improves the two primary efficiencies, absorption and thermalization.

The maximum of j_{sc} for a single junction is limited by the incident photon flux and the gap energy (1.13).

$$j_{sc,max} = q_e \int_{E_g}^{\infty} h\nu d\Phi(h\nu) \quad (1.13)$$

Thus, the use of more than one bandgap (a multi-gap device), is well-suited for the conversion of the full solar spectrum. The solar flux has then to be shared appropriately between the separate cells. Basically, higher energy photons can generate charges of higher energy. These can therefore be extracted at higher voltages from a material of sufficiently large electronic bandgap. Lower bandgaps absorb also low energy photons but deliver lower voltages (see also section 1.4.4). Figure 1.6 shows the solar spectrum and the shares of power that can be extracted by two different band gap energies, single and tandem (if combined). Two cells A and B with $E_{g,B} < E_{g,A}$ are placed on top of each other, cell A facing the sun. They form a tandem configuration. High energy photons ($h\nu \geq E_{g,A}$) are absorbed first by cell A . For all photons with less energy, cell A is transparent. They are absorbed by cell B for $E_{g,A} > h\nu \geq E_{g,B}$. Photons with energies below even $E_{g,B}$ are transmitted and not converted. The photon flux is now spectrally split by the filtering properties of the high band gap cell absorption edge. The inverse arrangement of B on top is not expedient, since B is also sensitive to high energy photons and would shade cell A if it was on top. Such a setup would simply be a single-junction cell of type B (with an expensive diode at its back contact - cell A). Between the two junctions in Eq.(1.14), the current is split up (theoretically lossless), but the voltages E_g/q_e sum up. Since $E_{g,A} > E_{g,B}$, or more importantly $V_{oc,A} > V_{oc,B}$, the summarized voltages $V_{oc,A} + V_{oc,B}$ are larger than twice $V_{oc,B}$ and contain a potentially large increase in efficiency, assumed all other conversion processes are not affected. In analogy to Eq.(1.8), the tandem power reads:

$$P_{tandem} = q_e E_{g,B} \int_{E_{g,B}}^{E_{g,A}} h\nu d\Phi(h\nu) + q_e E_{g,A} \int_{E_{g,A}}^{\infty} h\nu d\Phi(h\nu) \quad (1.14)$$

The above Eq.(1.14) assumes sharp absorption edges. Tab. 1.3 shows an overview of theoretical efficiencies of single- and multi-junctions devices.

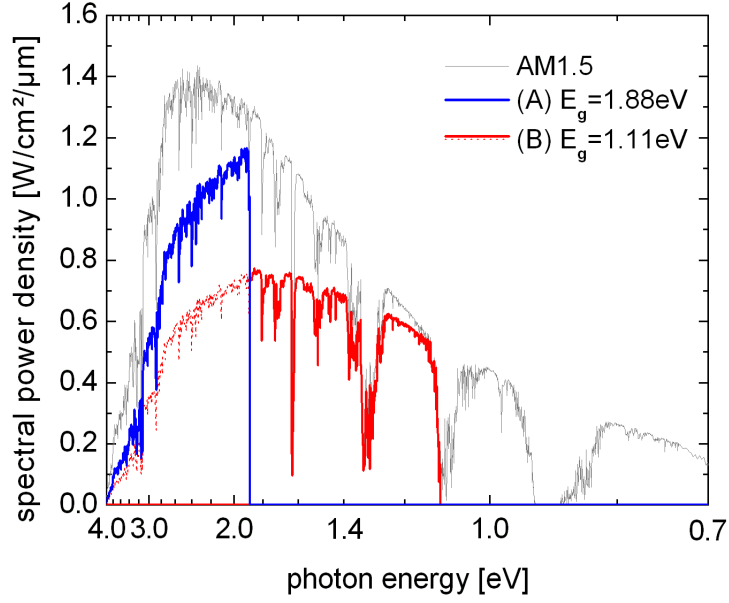


Figure 1.6: Irradiant spectral power density of the AM1.5 spectrum (thin, grey) and the (ultimate) spectral power density of a tandem configuration; the thin dotted line shows a single cell B without cell A. In the high energy range of 1.88 eV to 4 eV, high-gap cell A delivers higher voltage than low-gap cell B. Assuming the same photocurrent density this directly increases the power density.

junctions	E_g [eV] (ideal)	η (ideal)	E_g [eV] (monolit.)	η (monolit.)
1	1.06	40.6%	1.31	28.4%
2	0.74, 1.63	55.6%	1.00, 1.67	39.3%
3	0.59, 1.21, 2.02	63.6%	0.85, 1.41, 2.18	45.8%

Tab.1.3: Multijunction cells and their ideal and monolithic efficiencies in a 5762K black body spectrum [13]. Cell temperature is 298.15K, the monolithic results are for series-connected cells without back mirror, ideal results are for independent contacts and ideal coupling (optical and electrical).

The theoretical tandem efficiency for a perfect two junction device in AM1.5 spectrum is 39.8%. This equals the theoretical efficiency of an ideal single-junction up-conversion enhanced device. The tandem approach has already been used in 1978 by Moon [14], achieving a record of 28.5% in efficiency with spectral beamsplitting (Si, AlGaAs). Optimum band gap energies for a series-connected tandem cell have been suggested as 1.0eV and 1.67eV [13] by Tobias and Luque.

Frontside and backside improvements

Important enhancement can be provided not only by altering the major processes in absorber materials. Optical and electrical improvements at the ends of a cell have proven to be crucial to achieve high efficiencies - especially for harvesting of light.

Frontside improvements :

Front-side improvements reduce back reflection and surface recombination and enhance light-trapping of photons in the cell. Each photon lost at the front interface does not contribute to energy conversion. Optimized rugate filters [15] or the influence of front glass on thin-film cells [16] have been studied. Coatings and grating couplers have been investigated to improve the harvest of light[17–19]. Roughness generally leads to light harvesting: scattering enlarges optical paths in the solar cell. For silicon thin-films, Asahi-U (ITO) or HCl etched ZnO are widely used roughness types. Recent effort to engineer randomness from theoretical considerations[20] or to analyze the localization of light at random structures[21] are very promising. Extreme aspect ratios can be used to fabricate ‘black silicon’ [22]. A control of the angular distribution of light could achieve a concentration effect by limiting the angle of re-emission and re-balancing the radiative equilibrium[23].

Backside improvements :

At the back-end of a cell, reflection of long wavelength photons is able to increase the optical path inside silicon. In particular for thin-film silicon cells this is of interest. Other concepts address distributed Bragg-reflectors (DBR), backside diffraction gratings or $\lambda/4$ layers of TCO to allow thinner cells. Conformal structuring in thin-film cells, like grating couplers [24] can be applied on the front and rear side. Combined approaches of front, intermediate and backside devices have been discussed in recent literature[25].

1.1.5 Thin-film silicon tandem cells

Hydrogenated amorphous silicon cell

The first publication on deposition and properties of a-Si from a radio frequency glow discharge in silane (SiH_4) was written in 1969 [26]. The photovoltaic properties were soon recognized, especially the high absorption coefficient for visible light, as for example discussed by Pankove and Carlson [27]. The first amorphous silicon solar cell was reported by Carlson and Wronski in 1976 with an efficiency of about 2.4%. A-Si:H cells are widely spread as power supplies for small electrical devices, like electronic calculators. They are well suited for these applications, because they are relatively low-cost products and provide a higher output voltage than crystalline silicon cells.

Fabrication of the cells is mainly done via glow discharge deposition methods like plasma-enhanced chemical vapor deposition Although (single junction) a-Si cells do not count as high-efficiency cells among other silicon based PV devices, they are to some extent made

1 Introduction

of a unique material. Amorphous silicon shows a variation of the binding length, which is fixed in the crystalline phase. The amorphous phase of silicon allows transitions like a direct band gap semiconductor because of the breakdown of k-selection rules without a long-range crystalline order. It enables photons to be absorbed via direct optical transitions from the valence band into vacant states of the conduction band. This increases the absorption coefficient, so a-Si cells can be produced at significantly smaller thicknesses while still providing high absorbance. While thicker cells have a higher absorbance which means a higher short-circuit current, the open-circuit voltage of a-Si cells is only weakly dependent of the cell thickness. A-Si:H is typically hydrogenated for photovoltaic applications in order to counteract two characteristics of the amorphous phase that are limiting the charge carrier lifetime and diffusion length: dangling bonds and tail states. Dangling bonds are unsaturated valences in the electron shell of silicon atoms. They are a typical defect in the amorphous phase where not all electronic bonds are satisfied - unlike in crystalline silicon where each atom is bound to its four next neighbors. If not saturated with hydrogen, they also tend to make the doping of amorphous silicon more difficult. Tail states that reach into the band gap introduce traps for charge carriers. These trap states within the band gap act as centers for non-radiative recombination. The incorporation of hydrogen leads to a relaxation of the lattice and eliminates tail states.

Speaking of one band gap for a-Si is physically incorrect, since it is disordered. But typical values for the E_{04} of amorphous silicon (where $\alpha = 10^4 \text{ cm}^{-1}$) are about $E_{g,a-Si} = 1.7 \text{ eV} \pm 0.2 \text{ eV}$ [27]. Dopants for a-Si are boron (p-type) and phosphor (n-type), similar to crystalline silicon. The diffusion length is very small, in doped a-Si:H it is nearly zero. Therefore, ‘p-i-n’ diodes are used instead of p-n junctions. The ‘p-i-n’ (or ‘n-i-p’) devices have an intrinsic (undoped) zone which is enclosed with one p-type layer on top and one n-type layer at the bottom. The doped layers are very thin, typically about 20nm in thickness, whereas the intrinsic layer is larger. The built-in electric field is used to create a drift between the p and n layers. In contrast to p-n junctions with only a small spatial depletion layer, the drift contributes in p-i-n cells to charge transport across the complete thickness. This is responsible for a reduction of the fill factor in a-Si:H cells. The main share of absorption occurs in the intrinsic layer. A doped front-layer is designed as a so-called ‘window’ that despite its dopant concentrations has to let as much of the incident sunlight as possible pass into the intrinsic layer. Silicon carbide (p-SiC) window layers have been proposed for this purpose[28, 29]. The cell is mechanically supported by a substrate such as glass, stainless steel foils or plastic foils. The discussed tandem cells are of ‘superstrate’ (p-i-n) design: light enters the cell through the glass substrate.

Degradation occurs during the first few hundred hours of exposure to sunlight. The initial efficiency is reduced by about 10%-30% within 1000 hours of illumination, expressed by significant reduction of the fill factor. This behavior is common among all amorphous silicon solar cells and is worse at higher thicknesses. It is explained by the Staebler-Wronski effect [30], describing the light-induced changes in the hydrogenated a-Si of the cells. The effects can partially be healed out after the first illumination by tempering at 150°C . Also, a very slow annealing at operational temperatures has been suspected to temporarily counteract the Staebler-Wronski effect[3]. In field studies, a-Si cells show smaller temperature dependence in their the efficiency, smaller losses with rising temperature. The high band gap of a-Si:H makes the cells less vulnerable to any increase of the temperature dependent

dark current, because the influence of j_{sp} in (1.10) is smaller.

Microcrystalline silicon cell

The electronic band gap of microcrystalline silicon hardly differs from that in a monocrystalline phase. It is close to 1.1eV. As deposited μc -Si is typically n-type, originating from donor doping by incorporation of impurities such as oxygen or nitrogen. The impurity level has to be kept below certain limits in order to achieve intrinsic material. Deposition is done via PECVD, VHF-GD (very high frequency glow discharge) or ‘hot-wire’ technique (catalytic CVD).

The μc -Si cells are thin film cells of few microns in thickness, delivering about $20mA/cm^2$ at about 0.5V with efficiencies of up to 10%. Also $3.5\mu m$ thin films of this type have been reported with current densities up to typically $26mA/cm^2$ [31]. Unlike a-Si:H, the microcrystalline form of silicon does not generally suffer from degradation after light soaking but is stable. A review of thin-film cells made of μc -Si and micromorph tandems is found in Ref.[32]. In 2003, more than 25MW (peak) power of amorphous and microcrystalline cells have been produced.

Transparent conductive oxides

In thin-film cells, three transparent conductive oxides (TCO) are used: zinc-oxide ($ZnO : Al$), tin-oxide ($SnO_2 : F$) and indium-tin-oxide ($In_2O_3 : SnO_2$, ‘ITO’). Tin-oxide will not be addressed in detail. The TCO mainly serve as transparent front contacts and will be important materials for the design and fabrication of photonic IRL in this thesis.

Zinc oxide serves as TCO in thin film solar cells. Its density is $\rho_{ZnO} = 5.67g/cm^3$. It is thermally stable with a melting point at $1975^\circ C$. ZnO is a wide band gap semiconductor and absorbs in the UV, its band gap is at 3.4eV. Refractive indices are reported from $n=1.7$ to $n=2.0$ in the visible spectral range, depending on the method of preparation and porosity. The specific resistance has been reported as low as $8 \cdot 10^{-4}\Omega cm$. Sheet resistance is about $6 - 8\Omega/\square$. [33]. Conformal films from ALD have been reported with resistivities of down to $3.5 \cdot 10^{-3}\Omega cm$ [34]. Wet chemically prepared films from sol-gel processes for ZnO:Al are known with resistivities of about $1.5 \cdot 10^{-4}\Omega cm$ [35]. Zinc oxide is well-suited for transparent contacts in thin-film solar cells: etching in HCl leads to randomly structured surfaces which improve light-trapping. It is the TCO used at the Research center Jülich and at the University of Neu-Châtel.

Indium tin oxide is a widely used TCO for displays of all kinds, organic LED and touchscreen devices and thin-film solar cells. It is mostly composed as $In_2O_3 : SnO_2$ (90%wt,10%wt). ITO is remarkable for its high refractive index of about 2-2.5 depending on deposition technique. The melting point is about $1900^\circ C$. The density is $\rho_{ITO} =$

$7.4g/cm^3$. Although vapor deposition and sputtering are common, also wet-chemical synthesis is possible. Typical commercial ITO coated glasses and plastics offer sheet resistances of about $5 - 100\Omega/\square$. Drawback of this TCO is the use of the rare and expensive element indium. ITO is used for example by USSC in a-SiGe alloy triple cells.

1.1.6 Micromorph silicon tandem cell

In the 1980's, tandem cells have been theoretically and experimentally studied in great detail [36]. In particular, thin-film a-Si has been investigated as a top absorber, while c-Si or μc -Si / nc-Si (nanocrystalline Si) were suggested as bottom cells. Tandem or triple cells made of a-Si and a-SiGe alloys have shown outstanding performance in long-term outdoor testing. Their performance ratio of actual power to peak power was above that of crystalline silicon cells in Middle-European climate conditions[37]. Module efficiencies reach 10.4%[6].

In recent years, research has focused on so-called micromorph silicon solar cells, built from one amorphous and one microcrystalline junction, for example by University of Neuchâtel [31] (Switzerland) and Forschungszentrum Jülich (FZJ) (Germany). The combination of a-Si:H and μc -Si:H cells to build a tandem is motivated by the already discussed multi-junction efficiency. Here, the large difference in band gap (1.7 eV - 1.1 eV) should be noticed, as it contains the multigap advantage. According to Green [2], ideal bandgaps for a series-connected two cell tandem in diffuse sunlight are 0.97eV and 1.70eV⁴. The a-Si:H top cell is typically about 150 nm - 250 nm in thickness, the μc -Si bottom cell roughly between 1 μm and 2 μm thick. Figure 1.7 shows a schematic design of a micromorph silicon cell from FZJ. The front cell is deposited directly onto a textured ZnO front glass, which serves as a transparent front contact and superstrate. In between the junctions, doped tunneling layers terminate the n- and p- regions of the junctions against each other. The bottom cell follows conformally and is typically finalized with a (TCO-connected) metal backside reflector and contact.

The experimental EQE of two junctions from the same tandem are shown in the right Fig. 1.7. It has been fabricated at FZJ as published by Roschek[38]. The spectral overlap of the EQE offers an opportunity to tailor the photon distribution between the two junctions by intermediate optical filters. High energy photons are being absorbed completely in the a-Si:H top cell, while red and infrared light is transmitted to the bottom cell, being absorbed by the μc -silicon. In the spectral range between 550 and 700 nm the top cell suffers from decreasing absorption coefficient of a-Si:H towards longer wavelengths. But due to its higher open circuit voltage V_{OC} the a-Si:H top cell delivers a higher electrical power per absorbed photon. Therefore, the absorption of the amorphous cell should be maximized. This imperative is guided by the required current matching in the series-connected tandem[39]. Thicker μc -Si films can increase the absorbance in the bottom cell. An enhanced top cell current could therefore be matched by a thicker μc -Si cell. However, this is not economically feasible because of the low growth rates in deposition.

³Ref.: Sigma-Aldrich

⁴Table 5.1., pp.61

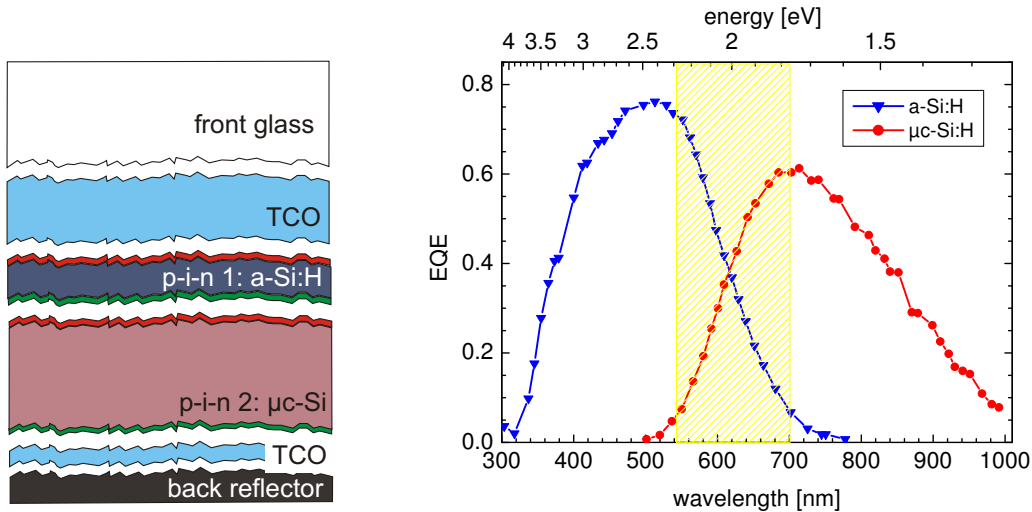


Figure 1.7: (left) schematic of micromorph tandem cell in p-i-n superstrate configuration, deposited directly on front glass; (right) measured EQE of a micromorph tandem, the spectral region of interest (roi) is marked between 550nm and 700nm.

State-of-the-art fabrication techniques have been reported for example by Meier in 2005 [40], using Unaxis reactors for module production. Japanese Kaneka corporation has been publishing promising developments in efficiency on their tandem cells, 11.7% efficiency have been certified by AIST [6] in a submodule. The highest (initial) efficiency of a micromorph cell was reported to be 15% for a small cell of 1cm^2 size[41] - using an innovative optical interlayer. The concept behind this success is discussed in the following section 1.2 and the discussion chapter, and it will be pursued towards novel approaches using photonic crystals in section 1.4.

1.2 Intermediate reflectors

One major drawback of the amorphous silicon solar cell is its limited thickness. It is not a fancy solution to reduce the thickness of the bottom cell accordingly. Surely, this would reduce the current mismatch but also it would not increase efficiency of the cell. Far more practical is the approach to operate the a-Si:H cell not at its MPP. A reduction of the a-Si:H filling factor can pay back by an enhancement of the tandem filling factor. Lower voltage at the a-Si:H cell allows higher current, following the I/V characteristic. Thus, current matching can be improved at the cost of output voltage.

To counteract the current-mismatch in the micromorph tandem cell without affecting the proper operation of both absorbers, an optical matching of the photon distribution between the two cells must be achieved. Therefore, an optical filter is introduced between the top and bottom absorber: the intermediate reflector. The task of this device is to reflect a certain ratio of the incident light after passing the top cell back into the top cell, improving

its absorption and increasing the short-circuit current. The illumination of the $\mu\text{c-Si}$ cell is reduced by the same ratio, thus its current is lowered. Appropriate design of the tandem with an intermediate reflective layer (IRL) should result in current matching. In detail, the spectral sensitivities of the junctions have to be considered: the absorption edge of a-Si:H defines the spectral region of interest to about 550 nm to 700 nm (see Fig.1.7).

1.2.1 Current state-of-the-art in intermediate reflectors

In order to increase the current of the top-cell optically by managing the photon distribution the intermediate reflective layer (IRL) concept has been pursued for example by Dominé [42–44] (University of Neu-Châtel) and Yamamoto [41] (Kaneka Corp.). In 2007, micromorph cells on flexible plastic substrates were reported by Haug[45], with incorporated IRL of a silicon oxide compound. They achieved current matching improvement up to $\Delta j_{sc} = 0.2 \text{ mA/cm}^2$ at about $j_{sc} = 11.2 \text{ mA/cm}^2$. The common approach is the use of a homogeneous or porous TCO layer of about 100 nm in thickness. It leads to reflection at the interface between the top cell and the IRL, as well as between the IRL and the bottom cell. This reflectance is mainly described by Fresnel’s equations, uses Fabry-Pérot oscillations (FPO) and strongly depends on the thickness of the interlayer. The homogeneous IRL is very attractive because of its compatibility with available deposition technologies. Remarkable enhancements have been achieved: Kaneka reported initial efficiencies of 13.4% in a small module and 15% for a lab cell of 1 cm². This shows the potential of the photonmanagement approach. A stable efficiency of $\eta=11.7\%$ is listed in the solar cell efficiency tables of 2007.

Investigations of such layers by Krc et al. in 2006 revealed: “Optical analysis of the interlayer revealed possibilities for significant improvements of J_{SCtop} (>25%) or thickness reductions $\Delta d_{i\ top}$ (>50%) for interlayers with small refractive index ($n_{inter} < 2.0$)”[46]⁵. Low refractive index of the IRL is in any case favored by Krc, as low as even $n_{IRL} = 1.2$. Their results included also the observation that strong enhancements of the top cell will significantly reduce bottom cell illumination when using massive or rather homogeneous interlayers. This is caused by the overall reflectance leading to back-reflection losses also in the red regime.

Shah et al from the Swiss IMT stated in 2005: “Various laboratories fabricate today “micromorp” tandem cells (with or without ZIR) with initial efficiencies of 13 to (almost) 15% and stabilized efficiencies in the 11 to 12% range. Such results are being achieved now since several years. In general, Voc-values achieved for the tandems are about 1.4 V and fill factors just above 70%. There appears to be no straightforward method for further increasing these 2 parameters” [32]⁶. The IRL is denoted here a ZnO intermediate reflector (ZIR). As one possible issue of enhancement however, they identify the optimization of the ZIR / IRL.

⁵p. 1894, Conclusions

⁶2nd paragraph after Fig. 5 in section Micromorph Tandems

1.3 Introduction to photonic crystals

This chapter introduces the concept, selected properties and theoretical basics of photonic crystals (PhC), which is necessary for the concepts of a photonic crystal IRL developed in this thesis. A great deal of literature is already available, covering their theory and numerical treatment from introductory to graduate level and more specialized research. Therefore I will only cover those aspects of this fascinating field of modern physics, that are directly related to my work. Fundamental publications [47] and books, as for example written by Joannopoulos [48] and Sakoda [49] provide detailed understanding and the straight forward development of PhC on different levels. The fundamentals of optics and the interaction of light with periodic dielectric matter are presented briefly in this chapter to provide a helpful familiarity with terminology and physical background. The nature of artificial opaline PhC will then be examined.

1.3.1 The photonic master equations

Everything about photonics is based on the fundamental equations of electrodynamics, developed and published in 1865 by J. C. Maxwell, entitled “A Dynamical Theory of the Electromagnetic Field”[50]. The macroscopic Maxwell equations in their differential expressions read:

$$\begin{aligned} \nabla \cdot \vec{D} &= \rho & (1.15) & & \nabla \times \vec{E} &= -\frac{\partial \vec{B}}{\partial t} & (1.17) \\ \nabla \cdot \vec{B} &= 0 & (1.16) & & \nabla \times \vec{H} &= \frac{\partial \vec{D}}{\partial t} + \vec{j} & (1.18) \end{aligned}$$

Herein the electrical displacement \vec{D} is a function of (\vec{r}, t) as are the magnetic induction \vec{B} and the electrical and magnetic fields \vec{E} and \vec{H} , while ρ is the density of free electrical charges and \vec{j} is the electrical current density. In general, the equation $\vec{B} = \mu_0 \mu_r \vec{H}$ is space-dependent, since the permeability is a function $\mu_r(\vec{r})$.

For homogenous and dielectric materials with a dielectric constant ϵ_r and a constant magnetic permeability μ_r , the displacement and induction are easily linked to their fields.

$$\vec{D} = \epsilon_0 \epsilon_r \vec{E} \quad (1.19)$$

$$\vec{B} = \mu_0 \mu_r \vec{H} \quad (1.20)$$

We assume the absence of free charge carriers ($\rho = 0$) and electrical currents ($\vec{j} = 0$) and a magnetic permeability of unity as well ($\mu_r(\vec{r}) \equiv 1$). The fields are small so that only linear terms occur. Eliminating the magnetic field \vec{H} from equations (1.17) and (1.18) by means of rotation and deviation and with the help of equations (1.19) and (1.20) and the relation $1/c^2 = \mu_0 \epsilon_0$, we get to the wave-equation of the electrical field \vec{E} .

$$\vec{\nabla} \times \vec{\nabla} \times \vec{E}(\vec{r}, t) = -\epsilon(\vec{r}) \frac{1}{c^2} \frac{\partial^2}{\partial t^2} \vec{E}(\vec{r}, t) \quad (1.21)$$

For the magnetic field the wave-equation is found analogously:

$$\vec{\nabla} \times \frac{1}{\epsilon(\vec{r})} \vec{\nabla} \times \vec{H}(\vec{r}, t) = -\frac{1}{c^2} \frac{\partial^2}{\partial t^2} \vec{E}(\vec{r}, t) \quad (1.22)$$

Assuming the fields as harmonic waves with separation of time dependence and spacial development, which is allowed for due to the linearity of Maxwell's equations, the electric and magnetic fields can be written as:

$$\vec{E}(\vec{r}, t) = \vec{E}(\vec{r}) \exp(-i\omega t) \quad (1.23)$$

$$\vec{H}(\vec{r}, t) = \vec{H}(\vec{r}) \exp(-i\omega t) \quad (1.24)$$

and the master-equations of photonics for both fields are obtained:

$$\frac{1}{\epsilon(\vec{r})} \nabla \times \nabla \times \vec{E}(\vec{r}, t) = \left(\frac{\omega}{c}\right)^2 \vec{E}(\vec{r}, t) \quad (1.25)$$

$$\nabla \times \left(\frac{1}{\epsilon_r(\vec{r})} \nabla \times \vec{H}(\vec{r}) \right) = \left(\frac{\omega}{c}\right)^2 \vec{H}(\vec{r}) \quad (1.26)$$

The operations on the left side of (1.26) performed on the fields \vec{E} and \vec{H} can be combined in one mathematical operator each, usually named Ξ and Θ , which make the Eigenvalue nature of this problem obvious.

$$\frac{1}{\epsilon(\vec{r})} \nabla \times \nabla \times \vec{E}(\vec{r}, t) = \Theta \vec{E}(\vec{r}, t) = \frac{\omega^2}{c^2} \vec{E}(\vec{r}, t) \quad (1.27)$$

$$\nabla \times \left(\frac{1}{\epsilon_r(\vec{r})} \nabla \times \vec{H}(\vec{r}) \right) = \Xi \vec{H}(\vec{r}, t) = \frac{\omega^2}{c^2} \vec{H}(\vec{r}, t) \quad (1.28)$$

The solution of the magnetic field is being preferred, as its operator is Hermitian and so the solutions will be orthogonal, and the Eigenvalues real.

Scalability

The dielectric function $\epsilon(\vec{r})$ is the only scaling element within the master equations (1.27), (1.28). One solution of the master equations yields for all wavelengths and all frequencies, provided the structural size is adjusted accordingly. In other words “there is no fundamental length scale”⁷. The photonic master equations are scalable and so are the structures based on Maxwell's laws beneath them. This brings plenty of advantages with it, especially from the experimentalist's point of view.

⁷[48], p.20

1.3.2 1D photonic crystals

The so-called Bragg-stacks belong to the class of dichroic mirrors, interference-based reflective filters. The term ‘dichroic’ refers to the color selective optical filtering properties. Sophisticated specimens of this class consist of a sequence of braggstacks with different periodicities or materials. A single Bragg stack is a periodic optical layer structure with a repeating one-dimensional unit cell. This unit cell consists of two layers of two different materials of thicknesses d_1, d_2 ($d_1 + d_2 = a$) and refractive indices n_1, n_2 . Thus, the well-known Bragg stacks can be considered 1D photonic crystals with finite thickness. This section uses a 1D example to sketch the treatment of PhC and also the relation between stop gap bandstructure features and optical band stop filtering. The periodic variation of the permittivity $\epsilon(z)$ is only along the z -axis. With a lattice constant a , the thickness of the unit cell, it can be written as $\epsilon(z) = \epsilon(z + a)$. In x - and y - directions, the 1D PhC is considered infinitely extended. The 1D wave equation Eq. (1.29) reads:

$$\frac{c^2}{\epsilon(z)} \frac{\partial^2}{\partial z^2} E = \frac{\partial^2 E}{\partial t^2} \quad (1.29)$$

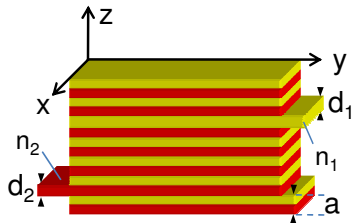


Figure 1.8: Schematic 1D PhC.

With a Bloch-function $u_k(z)$ and the Eigenmodes of the PhC being expressed by the term $E_k(z, t) = u_k(z) \exp i(kz - \omega_k t)$, after Fourier expansion and restriction to its dominant terms solutions to the dispersion relation $\omega(k)$ for the normalized frequency $\omega = a/\lambda$ are obtained. A 1D PhC of two materials with indices of refraction n_1 and n_2 and layer thicknesses $d_1 = d_2 = 0.5a$ is shown in Fig.1.8 schematically.

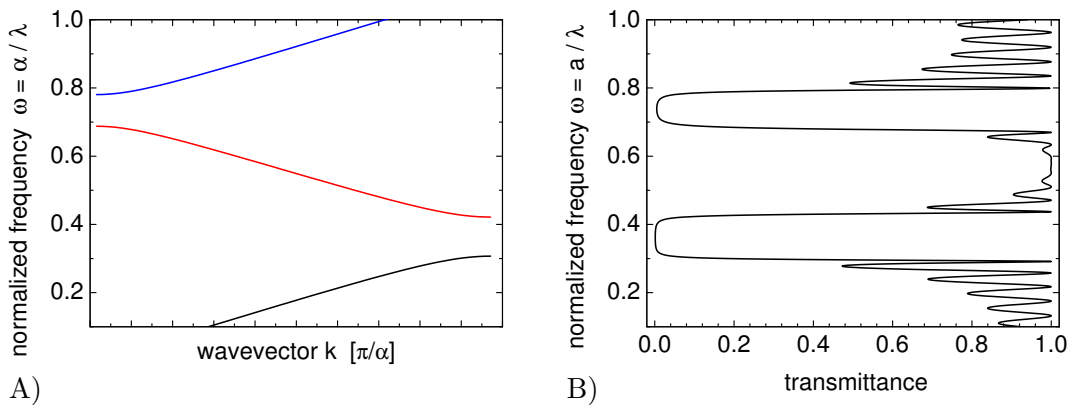


Figure 1.9: Band structure diagram (A) of a 1D PhC (Bragg-stack) composed of two layers of $n_1 = 1.0$, $n_2 = 3.0$, $d_1 = d_2 = 0.5a$. (B) shows the spectral answer in transmission of the 1D PhC of finite thickness $d_z = 8a$, calculated with FEM[51].

The obtained dispersion relation of the 1D PhC is shown in Fig.1.9(A). It plots the allowed frequencies (bands) over the Bloch mode k -vector. Where no solutions are found, the

1 Introduction

according reflectance spectrum in Fig.1.9(B) shows a drop in transmittance. The photonic band gaps force a reflection of light within these frequencies. The spectrum has been calculated with finite element methods [51] for a Bragg-stack of six unit cells (double layers) in thickness. The finite thickness is sufficient for a strong suppression of transmittance within the stop gap. However, the *sinc*-envelope for the occurring thin-film oscillations is still pronounced. Photonic Bragg-filtering can be realized with only a few contributing layers of the PhC if a sufficiently high refractive index contrast is provided.

1.3.3 Effective medium

If a medium consists of three materials of refractive indices n_a , n_b and n_c the simplest of all estimations is mostly termed the (geometrical) effective index approximation (1.30):

$$n_{\text{eff}} = f_a n_a + f_b n_b + f_c n_c \quad (1.30)$$

It only weights the volume filling fractions f of a material with its refractive index $n = \sqrt{\epsilon}$. Filling fractions always sum up to unity: $f_a + f_b + f_c = 1$.

A second approximation is the squared index approximation, applying a stronger impact of the index over the filling fractions, as shown in (1.31) for three materials that fill the complete volume, again adding up to unity.

$$n_{\text{eff}}^2 = f_a n_a^2 + f_b n_b^2 + (1 - f_a - f_b) n_c^2 \quad (1.31)$$

Herein, f_a of a typical opal template of hard spheres would be $f_a = 0.74$ and $f_b = 0$, leaving a volume of $1 - f_a = 0.26$ for the air voids.

Detailed considerations towards the application of effective index models and their errors in describing e.g. Bragg-reflection from opals have been conducted by Abrarov [52].

In general, any structured medium can be considered as an n_{eff} , if the wavelength of light is sufficiently larger than the structure or any spacial anisotropy of a material: the long-wavelength regime. Periodic media like PhC may be described with effective indices in certain spectral domains but not within the vicinity of a resonance, for example a stop gap or coupling modes. In such cases, the imaginary part of the refractive index has to be taken into account[53].

1.3.4 Structure of opaline photonic crystals

Three dimensional photonic crystals are mathematically treated similarly to atomic crystals in solid state physics. They are characterized by their lattice structure and its influence on the movement of photons in certain directions within a crystal. Various lattice models for 3D PhC exist. There are diamond or simple cubic structures, artificially drilled lattices, designed for practical production or woodpile stacks formed via two-photon absorption with high accuracy. Among the PhC that can be found in nature, opal is perhaps the most famous 3D PhC. Opals are gemstones with characteristic optical appearance and unique structure. They may be referred to as a mineraloid gel because they consist of ordered sub-micron scaled silica spheres (SiO_2) of 150nm to 350nm in diameter. The nano- or microspheres form a colloidal crystal, building blocks are the elements of a colloidal suspension (the spheres or beads), while the structure is a crystal lattice. This gives the opal its iridescent look and allows the play of colors when a stone is turned. The estimated duration of the self-organization process for opals in nature is about five million years. The impression of rough and polished opal stones is given in fig. 1.10 below. The shown gemstones are the highly valued black opals⁸. Synthetic opals are of interest



Figure 1.10: Photographs (left) of rough unset opals as found, (right) of polished black opals with very bright 'fire'.

not only as gemstones, but as candidates for optical (photonic) devices or as monolayered templates for nano-fabrication processes. This was investigated in 1969 as ordered suspensions were tested for their optical response[54]. Microgravity experiments for perfect opal growth have even been conducted by NASA⁹. Numerous publications cover this research area including hetero-structures and defect engineering [55–67].

Examples of theoretically possible opal lattices are the simple-cubic (sc) and the face-centered-cubic (fcc) structures. The sc lattice places one atom - or more generally one element - on each of the eight corners of the cubic unit cell. This results in a lattice, where $8 \cdot \frac{1}{8} = 1$ exactly one element is present in the unit cell: the corner elements count only as $\frac{1}{8}$ into the cube's volume. The length of the edges of the unit cell is the lattice constant a . This is also the primitive unit cell, it is not reducible. In the fcc lattice, also a cubic structure, each of the six faces of the cube carries another element, which will each count as half into the volume of the unit cell. So the fcc structure is a lattice

⁸source: UK's Black Opal,

⁹NASA/TM-2002-211287, available via <http://gltrs.grc.nasa.gov/GLTRS>

1 Introduction

with four atoms per cubical unit cell: the primitive unit cell with only one element would than measure $1/a^3$. Since in contrast to the sc, the closest neighbors to an element in the corner are now the face centered atoms, their vectors being diagonally oriented. Other structures are the body-centered-cubic lattice and the diamond lattice, both are of interest for photonic crystals, especially the diamond lattice. With sufficiently high index contrast it also exhibits a complete photonic band gap. Figure (1.11) shows simple, face-centered and body-centered cubic lattices. In this thesis, the focus lies on the fcc structures.

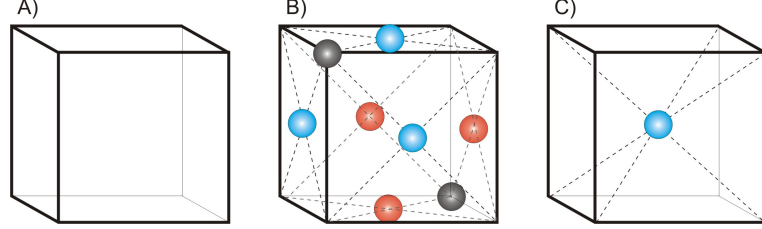


Figure 1.11: Cubic lattice types: A) simple (sc), B) face-centered (fcc) with diagonal face elements, C) body-centered (bcc) with the triagonally placed center element; for the fcc unit cell, frontside visible face elements are colored blue, while hidden elements are red. This is consistent with the axial sketch in figure (1.13).

The planes of a crystal are addressed via Miller indices. They characterize the orientation of a plane by the smallest all-integer multiples of the inverse crossing coordinates with the axes of the vectorial basis system. The three capital planes are the $\langle 111 \rangle$ (triagonal), $\langle 110 \rangle$ (diagonal) and $\langle 100 \rangle$ (facial).

Reciprocal lattice of fcc crystals

The construction of a reciprocal space (k-space or frequency space) from the real space structure leads to reciprocal lattice vectors $\vec{G} = v_1\vec{b}_1 + v_2\vec{b}_2 + v_3\vec{b}_3$. Transitions between reciprocal space and real space are performed via Fourier transformation. Lattice vectors in k-space differ by a phase of $m 2\pi$ ($m \in \mathbb{Z}$) from those in normal space, and the reciprocal equivalent of the Wiegner-Seitz-Cell is the Brillouin zone. Its boundaries are the planes normal to the reciprocal lattice vectors \vec{b} in both directions $\pm\vec{b}_1, \pm\vec{b}_2, \pm\vec{b}_3$. The base of the reciprocal lattice is generated from the real-space lattice according to the following equations (1.32), while the fcc lattice vectors become triagonally oriented in reciprocal space.

$$\begin{aligned} \vec{b}_1 &= 2\pi \frac{\vec{a}_2 \times \vec{a}_3}{\vec{a}_1 \cdot \vec{a}_2 \times \vec{a}_3} = \frac{2\pi}{a} (\vec{x} + \vec{y} - \vec{z}) \\ \vec{b}_2 &= 2\pi \frac{\vec{a}_3 \times \vec{a}_1}{\vec{a}_1 \cdot \vec{a}_2 \times \vec{a}_3} = \frac{2\pi}{a} (-\vec{x} + \vec{y} + \vec{z}) \\ \vec{b}_3 &= 2\pi \frac{\vec{a}_1 \times \vec{a}_2}{\vec{a}_1 \cdot \vec{a}_2 \times \vec{a}_3} = \frac{2\pi}{a} (\vec{x} - \vec{y} + \vec{z}) \end{aligned} \quad (1.32)$$

This is the description of a body-centered-cubic (bcc) crystal's Wiegner-Seitz-cell. The fcc and bcc lattice are Fourier transforms of each other. The length of the vectors of

high symmetry axes in fcc are given in the following table. They express the distances in reciprocal space between the points of high symmetry (P) and the Γ point, the center of the first BZ as shown in figure 1.12.

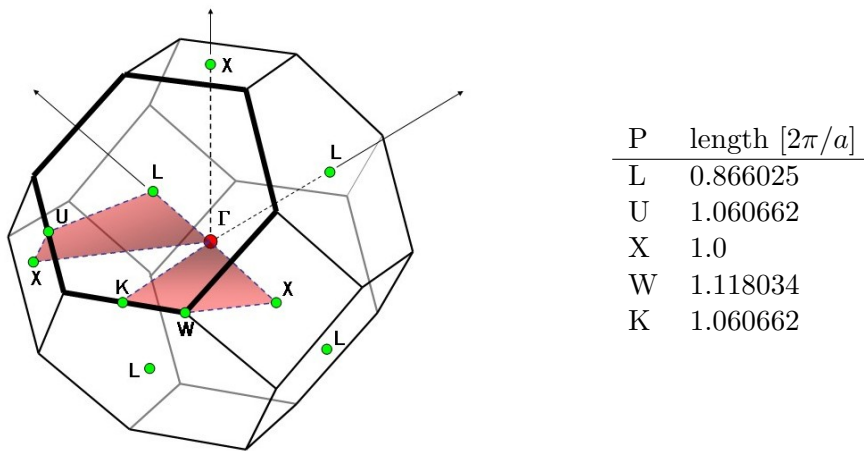


Figure 1.12: The Brillouin-zone of the fcc crystal has bcc symmetries: Main axis of interest is ΓL , with a hexagonal surface BZ (bold). The distances of high-symmetry points 'P' from the central Γ point are shown.

Face centered cubic vs. hexagonal close packed

With the same photonic scatterers as the fcc lattice, the hexagonal close packed (hcp) lattice is formed. They have many similarities, both produce sixfold rotational symmetries along certain crystallographic axes in diffractoin experiments. Their surfaces are sometimes both referred to as hexagonal. They both satisfy the condition of maximum volume filling fraction of 74% for a 3D hard-sphere arrangement, the 'close package'.

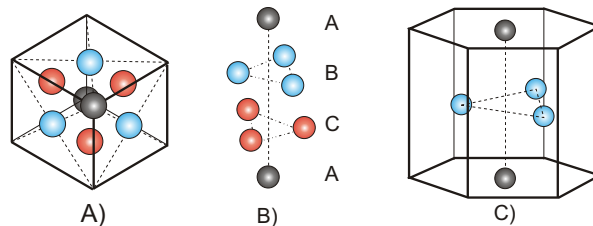


Figure 1.13: Slightly tilted view on one corner, along the trigonal 111 axis of the fcc (A): the layer sequence ABCA becomes obvious with the color coding from the previous figure (1.11) in the schematic axial sequence (B). The hcp unit cell exposes the layer sequence ABA (C), the sixfold 2D surface symmetry is shared by both crystal types.

However, the layer sequence is different, because in hexagonal lattices there are only two layers, A and B, with a periodic sequence of ABABA. The fcc crystal is built up from

1 Introduction

three layers in sequence ABCABCA. Figure (1.13) shows two sketches of fcc and hcp unit cells. This has no influence on packing density but can show unequal behavior when the different lattices are built as photonic crystals.

During crystallization of artificial opals, the chance of forming hcp structures instead of fcc is not negligible. A small difference in the relative free energy between both structures makes $\langle fcc \rangle$ lattices more favorable than $\langle hcp \rangle$ ones. This is useful for a thermal transition between the lattices in atomic crystals. The growth of artificial opals suffers from this rather small energetic difference as stacking faults that appear will introduce regions of hcp symmetry into an fcc crystal.

Driving forces of self-organization

Thin opaline photonic crystals are grown by self-organization. The two driving forces of self-organization in wet films have been identified by Higo et al. [68]: lateral capillary forces and convective flow. The capillary forces can be influenced chemically, by altering the acidity or adding different salts. For a detailed understanding of convective flow, it is necessary to consider the different flows and speeds in the dynamics of the crystallization process. Dimitrov and Nagayama [69] concluded that the presence of a monolayer of nanospheres, aligned on a substrate with the solvent in between them, increases the surface for evaporation. This increases evaporation itself proportionally (j_e) and results in a flow of solvent into the ordered array of spheres. During solvent evaporation, the nanospheres are forced into this region, which triggers self-organization. With these considerations, the velocity of the substrate (the coating speed v_c) can be determined for growth of a so called k-layer: a crystal of constant thickness consisting of k monolayers (with $k\epsilon N$).

$$v_c^{(k)} = \frac{\beta l j_{\text{evap}} \phi}{(1 - \psi) k d (1 - \phi)} \quad (1.33)$$

The coating velocity v_c in Eq.1.33 depends on the desired number of layers k , evaporation flux j_{evap} , meniscus length l , concentration ϕ , porosity ψ , particle velocity factor β and the particle diameter d . The formal description starts at a flow of solvent, accompanied by a flow of particles which aggregate into an ordered array. The driving force is the increased evaporation flux j_{evap} from the ordered colloidal array in Eq.(1.33). The ratio between the velocities of the particles and the solvent molecules is defined as $\beta = \frac{v_p}{v_w} \approx 1$ and is commonly assumed to be unity. β an ideality factor consisting of unknowns of the exact processes at microscopic scale. It is, however, possible to determine it experimentally for a set of fixed parameters, e.g. a certain suspension, environmental (\rightarrow section 3.1). The parameters of the colloidal solution are its volume fraction and the porosity ψ of the developing opal layer. The geometrical filling factor is $1 - \psi$. The latter is known to be $(1 - \psi^{(1)})=0.605$ for a monolayer of hard spheres. For the growth of a k-layer film, it converges to $(1 - \psi^{(\infty)})=0.74$, for an infinite three-dimensional crystal of closely packed hard spheres. Thus, the influence of the boundary monolayers (top and bottom) will vanish with increasing number of layers. This is closely related via $\psi \propto h/k$ to the thickness h of

an opal with finite size along the z-axis, according to Eq.(1.34).

$$h^{(k)} = \left(1 + \sqrt{\frac{2}{3}}(k-1) \right) d \quad (1.34)$$

Here the geometrical thickness of a monolayer would be d while the thickness of an nearly infinite 3D crystal ($k \gg 1$) would be $0.82kd$. Since the lateral dimensions (x/y) of the discussed structure can be accepted as being infinite in our case, the variation of porosity or filling fraction is only a matter of thickness.

Application of external forces

To influence the self-organization process, there are two possibilities, either the driving forces of self-organization by controlling the environmental conditions and other parameters of crystal growth can be modified, as already stated in this chapter - or additional external forces can be applied. Well-known examples of the latter are centrifugal forces assisting in the sedimentation of silica spheres into bulk 3D PhC and the use of noise to apply an artificial temperature to accelerate the formation of a crystalline phase. Both methods have been combined to optimize opal sedimentation with violet noise delivered by sound [70]. Electrostatical forces can assist in crystallization of charged colloids, while modulated electrical fields can apply noises. Electrically patterned surfaces can direct the growth and enable hetero-structures made of differently charged spheres. Strong mechanical forces of shear and strain can significantly shift the lowest energy level of crystallization to other structures, so the natural fcc crystal lattice can be changed to simple cubic (sc), as has proved successful in spin-coating processes[71, 72].

1.3.5 Photonic bandstructure of opaline PhC

The mathematically ideal case of an infinitely extended lattice has been used in solid state physics to describe the electronic properties of solids. The common model uses bands that develop from the interaction of a large number of atomic electron orbitals. As this number of participating atoms delivers a huge amount of allowed states, these states asymptotically develop into a continuum, into the bands. Initially, photonic crystals that are infinite in space will be described, PhC that are flawless in structure and that are defect-free. Thus, periodicity is constant and independent of spacial coordinates. Each Brillouin-zone (BZ) can be translated by a set of (reciprocal) lattice vectors and will exactly match another cell. Vectors outside the BZ can be folded back into the cell with the aid of appropriate lattice vectors. As a result, the knowledge of certain vectors within the Brillouin zone is sufficient to have knowledge of all related vectors and will make it possible to describe the properties related to each vector only within the BZ. The infinity of the crystal reduces the need of investigation to the Brillouin-zone.

The reciprocal space is a space of momentum - and since the wave vector \vec{k} is an element of momentum, it is not only convenient but also helpful to use $\frac{1}{\lambda}$ scalings. We are looking for the dispersion relation, the relation between a wave vector \vec{k} and the frequency ω , which is proportional to the energy of a photon. The relation $\omega(\vec{k})$ is called the band structure.

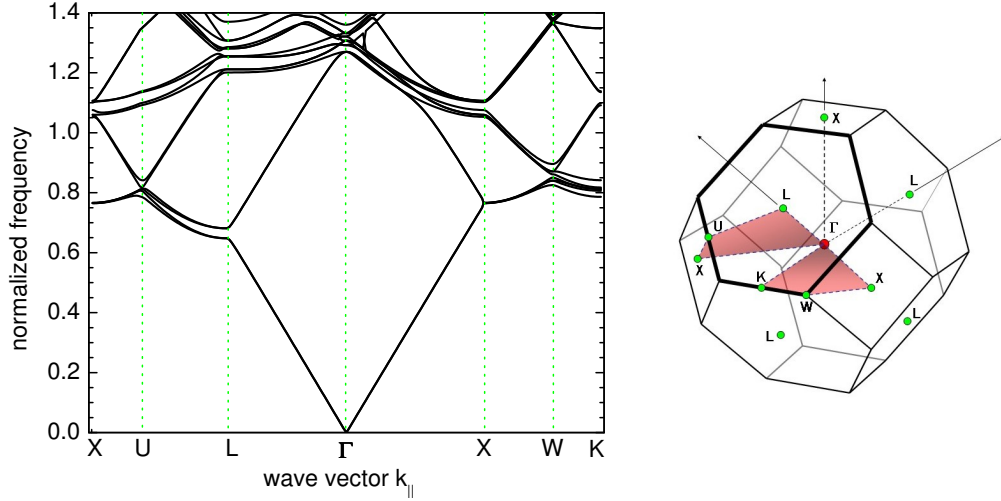


Figure 1.14: Photonic band structure of the opal fcc: $\epsilon_{\text{sphere}} = 2.0, \epsilon_{\text{host}} = 1.0$. The BZ from Fig.1.12 describes the crystallographic axes. The scan along $(\Gamma\text{-})\text{X-U-L-}\Gamma\text{-X-W-K(-}\Gamma\text{)}$ forms a closed path.

It is typically solved in between the high symmetry axes of a crystal, since these bands represent the extrema. A continuous curve of points where solutions of the same order exist for $\omega(\vec{k})$ form a band. Their order is counted from lowest energy: all lowest solutions form the first band. Commercially or freely distributed software to solve eigenproblems of the kind found in the master equations (1.26) can be used to solve equations for $\omega(\vec{k})$.

The photonic band structure (BS) of an opal is presented in Fig. 1.14. It shows the primary photonic stop-gap of opal structure in ΓL -direction. Light incident along this axis passes perpendicularly through the hexagonal surface of Fig.1.12. Below the frequency of the stop gap at $0.665a/\lambda$ there are no additional effects as there are only flat bands below. Tilting the opal against incident light, moves from ΓL in the BS towards X,W or U points. A rotation of the opal along ΓL decides on the exact tilt direction. Doing so, the complete BZ can be scanned by optical spectroscopy.

In this thesis, the software package from Steven G. Johnson, the MIT Photonic Bands (MPB) has been used to calculate all the bandstructures[73]. A brief description can be found in the experimental chapter among the computational methods. For homogenous and isotrope media, where $\epsilon(\vec{r})$ will not change spatially, the solutions (1.26) will be the so-called ‘light linet’: a straight line for $\omega(\vec{k})$, with a slope according to the refractive index.

$$\omega(\vec{k}) = \frac{c}{\sqrt{\epsilon(\vec{r})}}|\vec{k}| \quad (1.35)$$

To build up a photonic crystal for the BS calculations, the geometry and permittivities have to be defined, as well as a choice of wave vectors \vec{k} where we are interested in the frequencies. The k-vectors set the crystallographic directions in which information on the

allowed or forbidden modes of the PhC will be obtained. The impact of the refractive index on the band structure (BS) is divided into two parts: the overall mean (or effective) refractive index, a measure of the averaged optical density - and the refractive index contrast n_2/n_1 . The opal consists of dielectric spheres surrounded by air, typically the permittivities are $\epsilon_1 = 2.0$ (e.g. SiO_2) and $\epsilon_2 = 1.0$ (air). Changing the permittivities will lead to altered photonic properties. In case of $\epsilon_2 > \epsilon_1$, the structure is called inverted, like the contrast. The inverted opal (IO) consists of a dielectric host that surrounds spherical air voids. Although structurally the same crystal lattice, the inverted opal differs in filling fraction and allows the use of various materials, leading to a variety of possible contrasts. This is particularly important since they are no longer limited to matter that can be shaped perfectly spherical on the sub-micron scale. The filling of all voids of an opal template (26% of the volume) with a second material and the removal of the original opal (74%) after that, is called ‘inversion’ or ‘replication’. Inverted opals are widely used for photonic research and applications, sensing or light emitting applications [34, 74–78].

All the considerations and calculations so far are valid for infinite and defect-free PhC. In this thesis, three-dimensional thin-film PhC are treated. They are of finite thickness but have effectively infinite lateral dimensions. Their optical properties are investigated by solving Maxwell’s equations in real space using for example scattering methods. The numerical methods are addressed in section 3.5.

1.3.6 Optical properties of artificial opals

Optical properties of opals and photonic crystals alike have been investigated in numerous publications [53, 79–82] in the last decade. Here I will focus only on the relevant optical parameters for the photonic IRL.

Primary stop-gap: specular filtering

As the band structure in Fig.1.14 shows, the first stop gap is located at a normalized frequency ω_{gap} of Eq.(1.36) which links it to the lattice constant a and the optical wavelength λ_{gap} .

$$\omega_{\text{gap}} = a/\lambda_{\text{gap}} \quad (1.36)$$

For opals of $\epsilon = 2.0$, the gap is at a frequency of $\omega_{\text{gap}} = 0.665$ (gap center). The first stop band is the best pronounced feature of opals and their main feature used in this thesis. Within the spectral vicinity of this stop-gap, propagation of light is forbidden through the crystal. This is because there are no allowed non-evanescent photon modes in this direction and frequency range present. Thus, the opal is essentially a high-grade stop-band filter. The scalability of photonics makes it easy to match structural sizes to a desired spectral region. For a wavelength in visible regime, set at $\lambda = 600\text{nm}$, the required opal lattice constant is 0.665λ and with $a = \sqrt{2}d$ the diameter d of the nanospheres has to be 262nm . The stop gap has a certain width, in this case of about $\Delta(a/\lambda) = 0.033$ or $\Delta\omega/\omega_{\text{gap}} = 5\%$ relative. Optically this results in a spectrally narrow reflectance by opals, as shown in Fig.1.15 as photograph and reflectance spectrum.

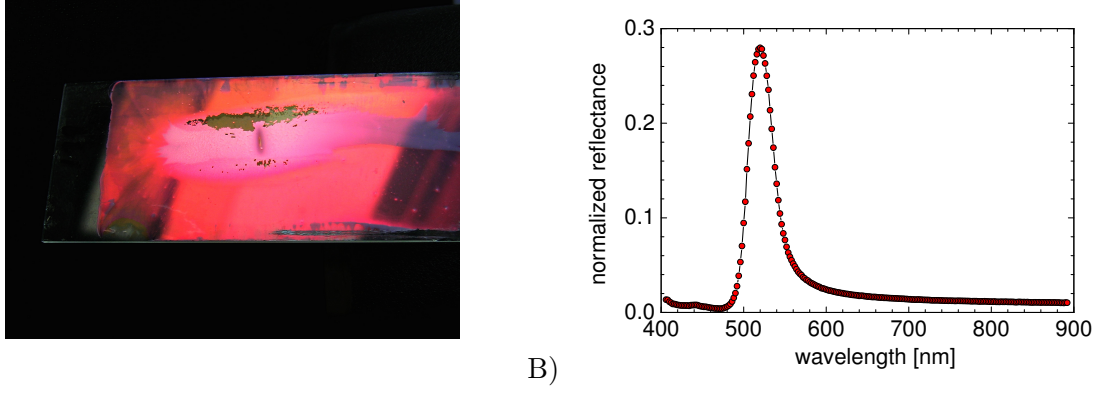


Figure 1.15: Photograph (A) of a $d = 300$ nm sample and spectrum (B) of the reflection from an artificial opal sample ($d = 250$ nm), both fabricated on microslide glass.

The creation of this stop gap can also be explained by the stacking of separate layers of spheres on top of each other. With reference to the model describing x-ray reflection on atomic lattices, the opal reflection peak is often referred to as Bragg peak [54]. The reflection peak depends on the angle of incidence, as does the photonic stop gap. The latter can be seen in the BS: from Γ -L to Γ -U, the lowest four photonic bands, which are delimiting the stop gap, move to higher energies. This equals a blue-shift of the stop gap center frequency. Angular dependence is incorporated in the Bragg Eq.(1.37) for the reflection peak.

$$\lambda_{111} = 2d_{111} \sqrt{n_{fit}^2 - \sin^2 \Theta} \quad (1.37)$$

The sphere diameter d is the capital parameter defining the spectral properties. The influence of refractive indices is discussed with the results of BS calculations in chapter 4.1.

Diffraction

The diffraction at 2D periodic structures, as any lattice plane of the 3D PhC represents, requires conservation of the wave vector \vec{k} .

$$k_{\parallel,inc.} = k_{\parallel,diff.} + m \cdot \vec{K} \quad (1.38)$$

In Eq.1.38, the incident parallel components of \vec{k} must be conserved. It equals the sum of the components of diffraction and an integer multiple m of the 2D lattice vector \vec{K} of the plane. No (in-plane) momentum can be generated or destroyed. An example is shown in Fig.1.16. Here, a sample made of large diameter spheres ($d = 560$ nm). The 3D crystal axes within the $\langle 111 \rangle$ plane are sketched in Fig.1.16(B). The 2D lattice constant of Γ -U and Γ -K are the same in fcc. Therefore, diffraction at $\langle 111 \rangle$ planes shows sixfold 60° rotational symmetry, instead of the 120° symmetry of the 3D fcc lattice. Tilted lattice

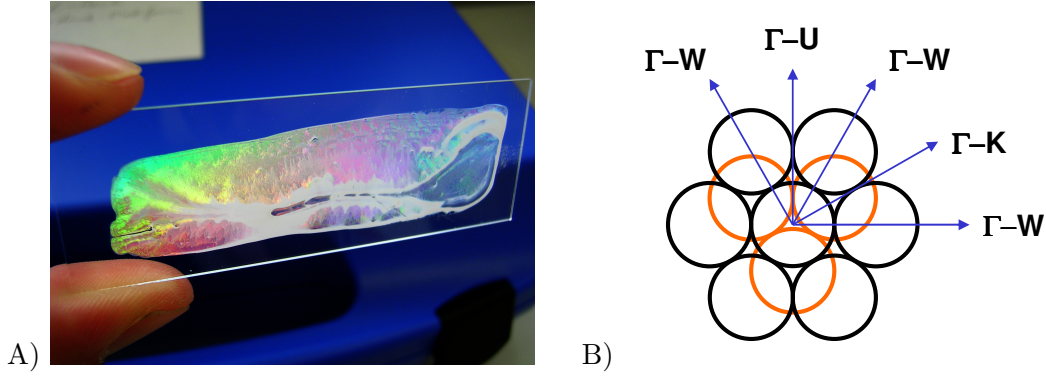


Figure 1.16: Photograph (A) of diffraction, PMMA opal sample ($d = 560$ nm) on glass, (B) crystal axes within the $\langle 111 \rangle$ plane, view along Γ -L direction.

planes in the 3D PhC can be treated by the cosine of their angles and thus like any 2D plane. Diffraction in transmission is angle limited by total internal reflection inside a substrate. For example, diffracted light cannot leave a microslide glass behind a sample unless the lattice period is large enough to produce sufficiently small deviation angles for a certain order of diffraction to exit the glass.

Thickness dependence of photonic properties

Theoretically, each additional lattice plane should contribute to the logarithmic decay of transmission modes. In real samples however, a saturation of this effect is reached at a certain number of layers. 1D scalar wave approximation (SWA) analysis of the optical density of opal-type PhC by Bertone[66] derived the following equation for an opaline crystals critical number of layers N_C :

$$N_C = \frac{1}{\pi} \left[\sqrt{4 + \left(\frac{K\psi_0}{1 - \psi_0} \right)^2} - 2 \right]^{-\frac{1}{2}} \quad (1.39)$$

with the constant $K = (2/\beta^3)(\sin \beta - \beta \cos \beta)$, and $\beta = 2\pi\sqrt{3/8}$; for close-packed spheres, incidence along $\langle 111 \rangle$ axis. In general, the superposition of incident and reflected modes, as well as reflected modes from next lattice planes, must produce maximum amplitudes to obtain strong reflection. Thus, the phase difference has to be an integer multiple of 2π between these modes. In that case, the transmitted modes will experience logarithmic decay. It has been shown experimentally, that this effect equals an increase of the imaginary part of the effective refractive index within the photonic stop gap. The actual thickness dependence can be described in analogy to the 1D case[83].

1.4 Aim of this thesis and IRL requirements

The aim of this thesis is the investigation of a photonic crystal approach to the intermediate reflector concept, specialized for the micromorph solar cell. The designated PhC is a thin-film of inverted opal. This investigation has to be followed along two paths, one being theoretical and the other of experimental nature. On one hand, it is necessary to perform numerical analyses of the potential of photonic crystals for this specific task and to identify possible drawbacks of the resulting devices. On the other hand, it is also the aim of the presented work, to develop aforesaid photonic device and to prepare specimen of such thin-films to analyse the desired properties experimentally. Together, both paths allow to develop a consistent design process from numerical predictions and their verification in experimental results.

The following sections at the end of the first chapter treat the classification of the presented work in terms of the photovoltaic processes and derive the most important properties of the proposed photonic IRL.

Considerations on the design of a current matched tandem cell start at the bottom absorber. It should be capable of providing twice the desired output current, even if half of it is shared with the top absorber later. This ensures the correct thickness for a sufficiently high absorbance in the long wavelength regime. The value of the current density however, is in this case obtained from consideration of the top cell that is limited in thickness and thus limited in output current. A representative (single) a-Si:H cell with $\eta = 9.5\%$ is capable of providing $V_{oc} = 0.86V$ and $j_{sc} = 17.5mA/cm^2$ (FF=0.63) or about $V = 0.6V$ and nearly $j = 16mA/cm^2$ at the MPP [6]. This current density will in best case be that of the tandem. Consequently the single bottom cell should deliver $32mA/cm^2$. The single a-Si:H cell features a metal back mirror, which is not present in the tandem. An ideal IRL would imitate this mirror without affecting the bottom cell, e.g. a heavy-side function in reflectance.

1.4.1 Classification of the proposed enhancement

In order to classify the aim of this thesis and to distinguish technical improvements from fundamental ones, it is useful to introduce two additional efficiencies: those of optics (light-trapping) and current matching, included in Eq.1.40. The optical efficiency of collecting and trapping light η_{opt} modifies the absorption efficiency, but contains only those effects and processes before photons are absorbed: e.g. frontside reflection losses, scattering on a structured interface, impact of anti-reflective coatings and also backside improvements to enlarge optical paths inside the absorber layer. All absorbance-related effects, like frontside-recombination, are part of the (new) η'_{abs} . The tandem efficiency of current matching η_{cm} introduces the losses from imperfectly matched electrical currents of series-connected junctions in multi-junction cells ('tandems'). It is expressed by the ratio of the output power of a tandem ($j_{tan} \cdot (V_1 + V_2)$) and the summarized power of the two junctions which are each driven at mpp. It is therefore unity in all single junction devices. The

efficiency of Eq.(1.5) can now be written for tandem cells ($i = \{1, 2\}$) as:

$$\begin{aligned} \eta &= \eta_{opt} \cdot \eta'_{abs} \cdot \eta_{tn} \cdot \eta_{td} \cdot FF' \cdot \eta_{cm} \\ \eta &= \frac{\phi_{coll}}{\phi_{inc}} \cdot \frac{j_{E,abs}}{j_{E,coll}} \cdot \frac{\langle \epsilon_e + \epsilon_h \rangle}{\langle \hbar\omega_{abs} \rangle} \cdot \frac{-q_e V_{oc}}{\langle \epsilon_e + \epsilon_h \rangle} \cdot \frac{\sum j_{mp,i} V_{mp,i}}{\sum j_{sc,i} V_{oc,i}} \cdot \frac{j_{tan} \sum V_i}{\sum j_{mp,i} V_{mp,i}} \end{aligned} \quad (1.40)$$

In this context, the focus of this thesis (and thus the impact of a spectrally selective intermediate reflector) can be classified. We can identify the task of the IRL as an enhancement of current matching in micromorph tandem cells (increase of η_{cm}). It is accompanied by minor improvements of thermalization efficiency in the bottom cell due to the IRL spectrally altering the photon distribution between the absorber layers.

1.4.2 Requirements of the photonic intermediate reflective layer

For an intermediate reflector of a micromorph silicon tandem cell, three fundamental requirements are needed:

- ◇ First, the IRL should deliver a spectrally limited back-reflectance (R) for the a-Si top cell where the EQE of both junctions is defining our spectral region of interest.
- ◇ Second, the IRL has to be sufficiently transparent (T) for red and infrared light.
- ◇ Third, the IRL must exhibit a sufficient electrical conductivity (σ), as the micromorph tandem is a series-connected 2-terminal device.

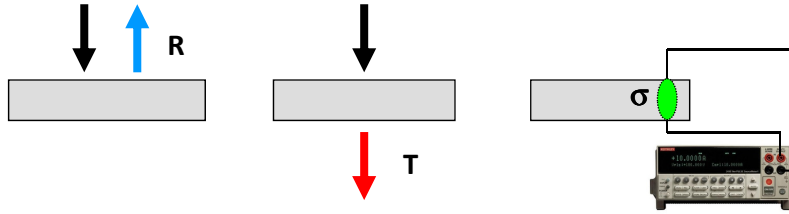


Figure 1.17: Schematic requirements of the IRL: selective reflectance, long-wavelength transmittance and electrical conductivity.

Considerations towards precise numbers should reflect that there is no standard micromorph cell. The thickness of both junctions is used to control absorption and especially the thickness of the μ c-Si cell can tune the tandem to any possible IRL that achieves promising photon management.

The a-Si:H absorbance is very high for short wavelengths, and we can narrow down the **reflectivity** requirement to the spectral range between 550nm and about 700nm. High reflectance is desired to increase the top cell current: This is the primary goal. Reflection losses through the front have to be avoided in the ROI and in the red/infrared regime. Any form of back-diffraction or back-scattering in reflection could contribute to enhancement of top cell current.

In **transmission** high values from 700nm to 1100nm have to be achieved. The better

1 Introduction

this feature is produced, the thinner the bottom cell can be made. Realistic marks can be set to a transmittance of $T=90\%$ demanded, 95% desired - losses at this point can be encountered to some extent with appropriate backside improvements.

Electrical **conductivity** limits are defined assuming a current density of about $j_{\text{mpp}} = 10\text{mA}/\text{cm}^2$ and choosing the critical limit $\Delta V_{\text{mpp}} = 20\text{mV}$ for the voltage drop at the IRL. Thus we arrive at 2Ω to be a terminal limit of sheet resistance. This leads to a critical resistivity in order of magnitude of $1\text{k}\Omega\text{cm}$ at $2\mu\text{m}$ of IRL thickness.

Intermediate summary I : Introduction

The **micromorph tandem solar cell** is a photovoltaic thin-film device. It can be produced at low cost and is theoretically capable of high efficiency. But, the micromorph cell suffers from imperfect current matching that reduces the fill factor and thus, efficiency. To achieve current matching, the photon absorption in the a-Si:H top cell has to be improved. Unfortunately, the a-Si:H cell is limited in thickness because of intrinsic material properties.

Intermediate reflective layers (IRL) can be used to manipulate the photon distribution between top and bottom cell. State-of-the-art IRL concepts make use of homogeneous TCO layers creating reflection at the interface between the absorbers. From the EQE profile of a-Si:H, an IRL with spectrally selective reflectance between 550 nm and 700 nm in wavelength is considered a very promising approach. The additional requirements of long-wavelength transmittance and sufficient electrical conductivity are identified.

A thin film of 3D **photonic crystal** is capable of providing spectrally selective reflectance - also from crystal films of finite thickness. Self-organized opaline systems grow an fcc lattice structure that develops not only the band-stop, but also shows no indication of inhibited long-wavelength transmission so far. In the short-wavelength range, there are undesired higher band features of the PhC. Additionally to Bragg filtering, diffractive contributions to reflected intensity can be expected, depending on the actual structural size parameters. The opal filling fraction of 74% leaves sufficient volume for infiltration and thus allows the use of various electrically conductive materials to form inverted opal structures

2 Experimental and numerical methods

2.1 Optical methods

To determine the optical properties of fabricated samples, three different experimental methods have been applied: optical microscopy, spectroscopy, and near-field microscopy give access to different properties of 3D PhC.

2.1.1 Microscopy

For investigations of artificial opal samples, their inverted counterparts, and samples with optical peculiarities in the visible regime in general optical microscopy has been performed using an Olympus BX51 microscope. The spectral properties of single crystallites or large areas have been measured with a fiber-attached spectrometer (R,T). Dark-field images have been shot to show surface information, especially scattering and roughness.

2.1.2 Spectroscopy

Spectroscopy in the visible to near-infrared range was performed on a lab-built spectrometer system (see Fig. 2.1). Using an iHR550 monochromator by Jobin Yvon, I measured angular reflectance with a goniometer system that allows to keep the 2Θ -condition for the angle of incidence. As light sources, 250W halogen bulbs or 75W xenon lights (Oriel) have been used according to the investigated spectral region. For angular reflection measurements, the setup has been measured without sample, but with an aluminium front mirror in its place, to normalize the measurements for each individual configuration. This leads to the dependence on the quality and lifetime of the used standard, but makes the results of separate focal configurations for different measurements comparable. Also, it eliminates deviations in the spatial intensity distribution afterwards, since no squared glass rod was used to homogenize the illuminated field. The used detector is a silicon photodiode of type Thorlabs DET210 (Si) fed into a Stanford Research system model SR830 DSP lock-in amplifier, the signal being chopped at 377Hz. The goniometer detection arm leads an ocean-optics ultra-low OH fiber of $500\mu\text{m}$ core diameter and with good transmission from 300nm to 1200nm, directly coupled to the monochromator entrance in front of the slit. The numerical aperture of the fibre is $NA_F=0.22$ matching the NA of the entrance of the monochromator.

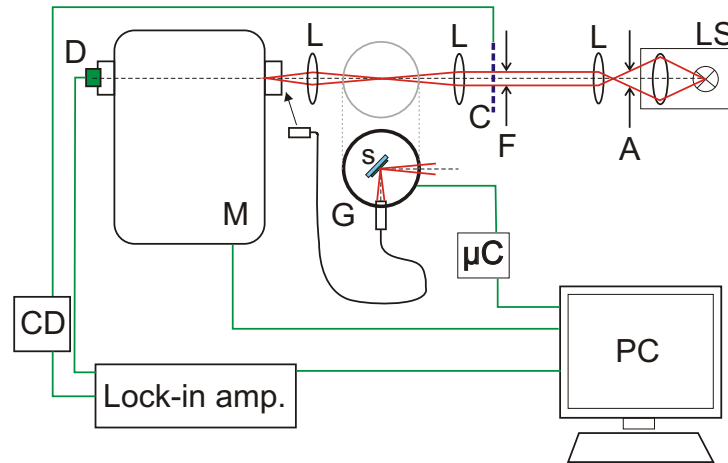


Figure 2.1: Scheme of the spectroscopy setup for specular transmittance and reflectance. It consists of exchangeable light source (LS), collimating setup with lenses (L), apertures (A,F) and chopper (C), the optional goniometer (G) with attached optical fibre holds the sample (s) for angular spectroscopy. Detection is at the monochromator's (M) exit with a photodiode (D), diode signal and reference from the chopper driver (CD) are fed into the lock-in amplifier. The motorized goniometer is controlled by an external microcontroller (μC), triggered by a personal computer which is also collecting the amplifier output data.

2.1.3 NSOM

Near-field scanning optical microscopy has been performed on opal and inverted samples at the Forschungszentrum Jülich at the NSOM setup of Dr. Bittkau¹. The LT-NSOM IV was built at the Max-Born-Institute (MBI), Berlin. The microscope allows multi-wavelength scans in 'contact mode' with the sample while topography is measured (WD of 20nm), or at fixed heights above. Measurements have been performed in transmission mode.

2.2 Scanning electron microscopy

To characterize the structures of samples, different types of scanning electron microscopes (SEM) have been used, mainly types JEOL6060, 6300F, and 6700F. For statistical analysis of sphere diameters etc., low magnification overview pictures have been shot while high magnifications provide surface observations and thickness measurements, e.g. of depositions. Samples have been sputtered with gold if insufficient conductivity inhibited good photographs at exposure to the necessary acceleration voltages. SEM pictures allow for the monitoring of local and long-range order as well as defects. At cleaved edges, the depth of samples has been investigated.

¹Forschungszentrum Jülich GmbH, IEF-5, group of Dr. Carius

2.3 Preparation methods

The inverted opal thin-film samples that serve as intermediate reflectors are prepared from opal templates, are then infiltrated with vapor-based methods and finalized with chemical and thermal treatment to obtain inverted opal films. The methods and processes are presented in this section. Firstly, two lab scale methods for template fabrication are presented. Secondly, the atomic layer deposition process for zinc oxide is illustrated. Also, the wet chemical treatments are sketched briefly.

A highly monodisperse aqueous suspension of PMMA spheres with $d = 300\text{nm}$ has mainly been used for the sample fabrication. It was obtained from a single large volume polymerization process to ensure sufficient supply of nanosphere suspension with constant size distribution.

2.3.1 Vertical deposition

For thin-films, all kinds of coating processes can be used. The essential point however, is that the film must crystallize to become an opal. Up to now, this is achieved by using extremely slow velocities of film deposition, providing enough time for the beads to find their lattice positions. This is in literature often addressed as thermodynamic equilibrium of growth. Vertical deposition covers all methods aligning substrates more or less perpendicular to the surface of a reservoir of colloidal suspension. In Fig. 2.2, the principal setup of a vertical deposition (crystallization) setup is shown (A), along with the drying meniscus on the coated substrate (B). The driving forces are discussed in the introduction to PhC in chapter 1.2.

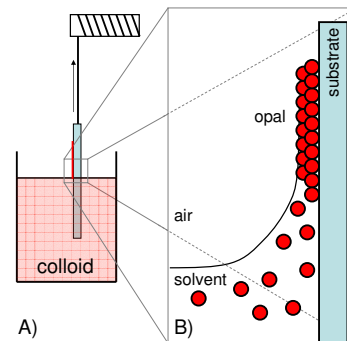


Figure 2.2: *Dip-coating*
 A) *setup scheme*
 B) *meniscus.*

The introduction of a motor drive or other mechanical means to pull a substrate out of the colloidal solution adds an additional parameter to the vertical deposition method. This makes high temperatures obsolete, at least for an acceleration of the crystallization speed. Consequently, it is possible to choose temperatures appropriately for colloid aggregation - and select the velocity of the substrate movement independently (technically speaking). The relation between these two, however, influences the thickness of the resulting crystal [84–86] as well as the crystal quality. At high coating speed for example, disorder is created in the opal film from motor vibrations. Therefore, the fabrication machinery has been designed with care and sophisticated dampening and protection from external disturbance (see chapter 3).

2.3.2 Knife coating

A slightly different method for the production of thin-films is knife coating. In contrast to common knife coating application for non-crystalline films, the drying process is here the essential step from a colloidal suspension to the final thin-film crystal. Key features are the coating thickness, coating velocity and environmental factors, which define the velocity of crystallization. Thus, the processes of deposition and crystallization are technically decoupled in such method. In Fig. 2.3, a schematic knife coating setup is shown. From a reservoir, the coating knife (or ‘blade’) deposits a colloidal film of mechanically defined thickness on the substrate. After the drying and crystallization, the opal film of final thickness is obtained.

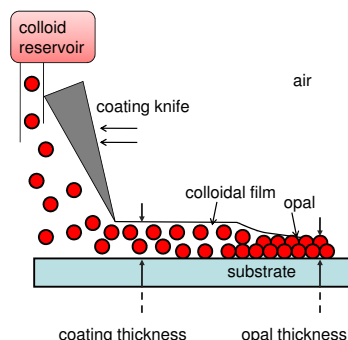


Figure 2.3: *Schematic knife coating setup.*

In analogy to the principles of vertical deposition, the crystallization process is determined by many variables. The decoupling of deposition and drying process however, allows to focus on high velocities of the coating knife, aiming at rapid thin-film fabrication. A knife coating setup has been built for the purpose of rapid sample production, as briefly described in chapter 3. It uses only a very small amount of colloidal suspension.

Required amount of colloidal suspension

Thickness control of knife-coated thin-film samples is quite possible, but also the amount of colloidal suspension of known concentration (volume fraction) can be determined. The final average thickness is simply calculated from the used amount of suspension V , the concentration c and the covered substrate area A by (2.1).

$$d_{film} = V/A \cdot c \quad (2.1)$$

An example for typical samples is the microscope slide: it measures $75\text{mm} \times 25\text{mm} = 1875\text{mm}^2$. Partially covered, the sample is perhaps 1500mm^2 in size. A desired thickness of $d_{film} = 1.5\mu\text{m}$ with a (volume) concentration of $c = 0.05$ would result in the needed amount of suspension of about $45\text{mm}^3 = 45\mu\text{L}$. I used mainly concentrations of 5%-10% for the manual preparation of thin film samples. Usually, the concentration is determined as ‘wt’, the weight share of the solid component in a suspension after drying. Then the density ratio between sphere material and solvent will be applied. The density of massive PMMA is about $1.19\text{g}/\text{cm}^3$, while water would be at $1.0\text{g}/\text{cm}^3$. Additionally, the volume fraction of the opaline PhC (74%) has to be taken into account, which leads to (2.2) for the calculation of the necessary solvent for thin PMMA opals from aqueous solutions.

$$V[\mu\text{L}] = A[\text{mm}^2] d_{film}[\text{mm}] \frac{100}{c[\%WT]} 0.74 \frac{1.19 \frac{\text{g}}{\text{cm}^3}}{1.0 \frac{\text{g}}{\text{cm}^3}} \quad (2.2)$$

The related number of opal monolayers for a certain thickness has been developed in 1.34 in the photonics chapter.

2.3.3 Replication method: ALD, CVD

For infiltration from gas phase (vapor), the methods of chemical vapor deposition (CVD) and atomic layer deposition[87] (ALD) were used. The CVD processing has been carried out by B. Lange and L. Steidl², while ALD procedures have been performed by S-M. Lee³. ALD is a technically more sophisticated type of CVD. It uses pure precursors and controls pulse durations and actual gas-flow in a time-scale of seconds and lower. This technical effort allows the deposition of single-molecular or single-atomic films on a substrate. It is a real layer-by-layer technique. The thickness of a single layer is in the case of zinc-oxide about 0.2nm.

The main advantage of chemical vapor methods is their self-terminating nature that allows outstanding control of thickness at almost perfectly conformal deposition characteristics. For the formation of zinc oxide, two precursors are used: Diethylzinc ($ZnEt_2$) and water (H_2O).

The reaction cycle consists of four steps. After exposure to water vapor (1), the specimen chamber of the reactor is purged with nitrogen (N_2) (2), removing all water not adsorbed on the sample's surface. The input of $ZnEt_2$ (3) exposes the adsorbed water molecules to a reaction partner and allows every two different precursor molecules to form zincoxide and surplus ethanolic solvent. Step (3) is schematically shown in figure 2.4. A second purge step with N_2 removes surplus $ZnEt_2$. The complete cycle is shown schematically in Fig.2.5.

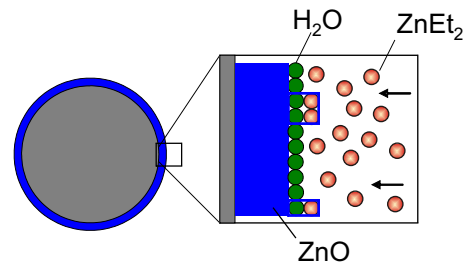


Figure 2.4: Schematic deposition of $ZnEt_2$ molecules with surface adsorbed H_2O .

Typical deposition parameters for low temperature ZnO synthesis are shown in Tab. 2.1.

	material	pulse [s]	exposure [s]	purge [s]
precursor 1	$ZnEt_2$	0.1	5	10
precursor 2	H_2O	1.5	15	150
temperature	substrate 60°C	wall 60°C	precursor 40°C	wall 80°C

Tab.2.1 (ALD) Parameters of low-temperature ZnO Deposition.

The very long purge time after water vapor pulses are a necessity caused by the low temperatures. The H_2O has to be purged out completely before the next deposition cycle starts, in order to avoid unwanted chemical reaction, CVD-type deposition, and other parasitic ZnO formation. Deposition temperatures (substrate temperatures) of up to 90°C have been applied, limited by the glass temperature of the latex beads.

²University of Mainz, Institute of Chemistry and Earth Science, group of Prof. Zentel

³Max Planck Institute of Microstructure Physics, Halle, group of Dr. M. Knez

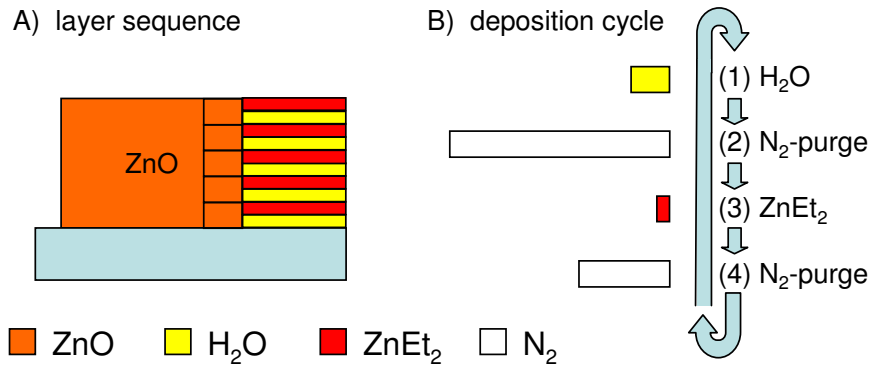


Figure 2.5: Deposition sequence and pulse cycle of ALD process for ZnO, schematic.

2.3.4 Wet chemical methods

Wet chemistry involves preparation of substrates, infiltration with nanoparticles from liquid phase and post-processing of samples.

Substrates of silicon have been hydrophilized with ‘piranha’ ($H_2SO_4 + H_2O_2, 3 : 1$) while for glass substrates cleaning with ethanol is sufficient in most cases, although KCl bathing can also be used. To remove the polymeric templates, tetra hydro furane (THF) is used. All processing has been limited to temperatures significantly below $200^\circ C$ to ensure compatibility with a-Si:H cell processing.

2.4 Simulation methods

The properties of infinite PhC have been obtained by the plane wave method with MPB by the calculation of photonic bandstructures. Reflectance and transmittance of finite samples, especially thin opal films, into the forward and backward half-space are simulated with several numerical methods, such as FMM and scattering matrix method for reflection and transmission. For final calculations, the results from rigorous methods have been applied, while for all tests and estimations, the faster approximative algorithms have been used. In figure 2.6 the three paths of optical simulations are shown.

2.4.1 Plane wave

The MIT Photonic Bands (MPB) Package has been developed by Steven G. Johnson and J. D. Joannopoulos, and is a software that is freely distributed under the terms of the GNU General Public License . It is based on their publication “Block-iterative frequency-domain methods for Maxwell’s equations in a planewave basis” [73] ⁴. It is a commonly

⁴<http://www.opticsexpress.org/abstract.cfm?URI=OPEX-8-3-173>

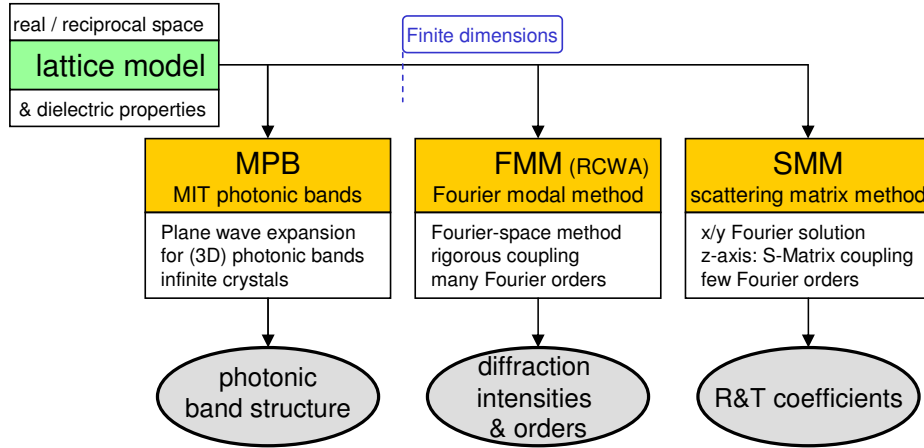


Figure 2.6: *Simulation methods: solving for photonic bandstructures of infinite crystals (MPB), complete diffraction intensity distributions (FMM) or half-space coefficients of reflectance and transmittance (SMM) for finite PhC.*

used and versatile solving method for 2D and 3D photonic bands. For artificial opals, the 3D unit cell has been implemented according to the reciprocal fcc-lattice vectors using the face diagonals of the unit cell as basis vectors. Most band structures have been solved with a resolution of 16 or 32 and a mesh-size of 15, while 19 points between the high symmetry axes are sufficient for smooth band structure plots.

2.4.2 RCWA, FMM

The coupled-wave analysis (RCWA) or Fourier matrix method (FMM) is a rigorous method to solve Maxwell's equations [88–90]. It describes the propagation of light through a grating, in this case a thin photonic crystal and determines the diffraction orders and intensities. These solutions allow to separate specular and diffracted light for transmission or reflection. It is a Fourier implementation to rigorously solve the diffraction efficiencies in different orders of a grating, or more generally a periodic optical structure. The method is not specialized to match certain problems, but uses planar waves to describe the field distribution in front of the PhC and behind. Therefore it can be used as a universal simulation tool but requires calculation time. Typically, spectra have been calculated with 101 points of resolution, in order to limit solving time. The RCWA method has been used by M. Peters⁵ to independently confirm selected results from my simulations in SMM (see below) with a second method.

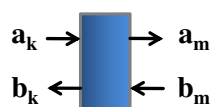
KKR is the acronym for (layer) Korringa-Kohn-Rostocker, a method that makes use of the expansion of the fields into spherical waves, if the surroundings are of spherical symmetry, while it uses plane-waves for non-spherical environments. This gives a special symmetry advantage for opals and their replicas: It is a specially suited variation of the FMM. The

⁵Fraunhofer ISE, Freiburg

KKR simulations referred to in this thesis have been performed by Dr. C. Rockstuhl⁶.

2.4.3 Scattering matrix method

The scattering matrix (SMM) algorithm uses a real space lattice model and only within defined x/y planes Maxwell's equations are solved in Fourier space. It is used to simulate scattering processes in general where no detailed knowledge on the scatterers is given. Briefly, the method derives the complex coefficients of transmission and reflection of a mode (plus the phase) - provided that the relation between incoming and outgoing mode (reflected and transmitted) are known. In contrast to transfer matrix methods, the incident modes on both sides are known and the outgoing modes are calculated (2.3), see Fig. 2.4.3. In detail, the SMM truncates the simulated structure in plane parallel layers



$$\begin{pmatrix} a_m \\ b_m \end{pmatrix} = S(k, m) \begin{pmatrix} a_k \\ b_k \end{pmatrix} = \begin{pmatrix} S_{11} & S_{12} \\ S_{21} & S_{22} \end{pmatrix} \begin{pmatrix} a_k \\ b_k \end{pmatrix} \quad (2.3)$$

Figure 2.7: *Sketch of the Scattering matrix principle: the blackbox links incoming (a_k, b_m) and outgoing amplitudes (a_m, b_k) from both sides, not 'left' or 'right' sides.*

(x, y) which are each being divided into a 2D mesh. The SMM couples every two of these 'chunks' via the S-Matrix recursion (in real space) to receive the z -component. Therefore, the number of chunks $(N-1)$ define the vertical (z -) resolution, their 2D mesh represents the lateral resolution. In front of the first layer (0) is the forward halfspace, behind the last one (N) the backward halfspace. The number of solved fourier orders (m) defines the precision of approximation. In case of a large number of orders $(m \rightarrow \infty)$, the approximation asymptotically closes in on the exact solution to the problem. If a problem can be solved with a small number of Fourier orders, this method provides a huge advantage in calculation speed compared to RCWA. In this thesis, our own SMM code⁷ has been used, based on the work of Whittaker and Culshaw[91].

⁶Institute for solid state physics and optics, University of Jena

⁷originally implemented by Dr. A. von Rhein

3 Results

3.1 Numerical simulation of 3D photonic crystal IRL

The aim of this thesis is to incorporate a photonic intermediate reflective layer within two silicon-based solar cells, which is bound by the requirements stated at the end of chapter 1. The search for filters that are energy-selective (spectrally limited reflectivity), diffractive and electrically conductive leads directly to 3D inverted opal structures. In this section, I present the simulation of photonic bandstructures and optical properties of inverted opal structures as well as their impact on the solar cell efficiency. Also, a numerical method to determine reasonable spectral positions of the reflection band of a selective filter will be treated within the numerical results.

3.1.1 Bandstructure calculation of 3D inverted opal PhC

The first step of investigation of photonic crystals is typically the calculation and analysis of band structures (BS). Therefore, inverted and also composite PhC have been calculated with the plane wave method. Since the crystal lattice and the symmetries are the same between the templates, composites and inverted opals, two types of parameters of the infinite model are left: refractive indices and filling fractions. These are considered for composite and inverted cases. In particular, conformally inverted opals are investigated to bridge the gap between the usually treated perfectly inverted opals and the imperfect infiltration that has to be expected in experiment.

Inverted opals

Examination of the BS of an inverted opal made of $\epsilon_h = 6.25$ and air with $\epsilon_h = 1.00$ (Figure 3.1) shows the stop-gap in the crystallographic L direction at a normalized frequency of $0.582 a/\lambda$. The lattice constant a is related to the diameter of the spheres via $a = \sqrt{2}d$. Within this stop-gap, propagation of light is inhibited through the crystal, so the inverted opal is essentially a high-grade stop-band filter. In Fig. 3.1 the angular behaviour of the stop-gap is shown from L to U (left path) and into X-direction (right). Parameters are $\epsilon_{\text{host}} = 6.25$, $\epsilon_{\text{voids}} = 1$. Since the photonic master equations are scalable, a diameter of the spheres can be adjusted to locate the stop gap of an inverted opal in the spectral region of overlap of the EQE in the micromorph tandem cell. The center of the reflection peak follows $\lambda = \sqrt{2}d/\omega_{\text{gap}}$, see Eq. (1.36). For the permittivities used in Fig.3.1, spheres between $d = 250\text{nm}$ ($\epsilon_h = 6.25$) and $d = 300\text{nm}$ ($\epsilon_h = 2.89$) appear suited.

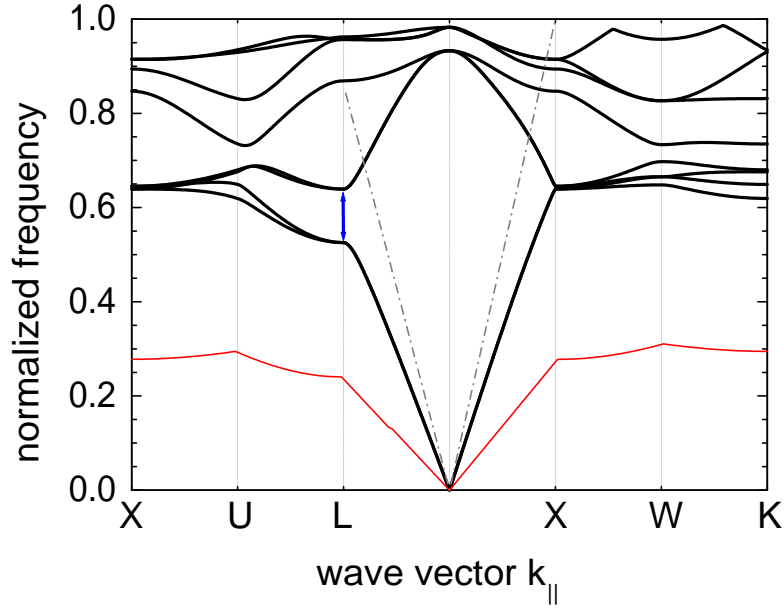


Figure 3.1: *Band structure of an inverted opal with $\epsilon_{host} = 6.25$, $\epsilon_{voids} = 1$; with light lines for Γ -L, Γ -X (dot+dash) and onset of diffraction at low frequencies (thin, red curve). The 19% wide first stop-gap is found in Γ -L-direction.*

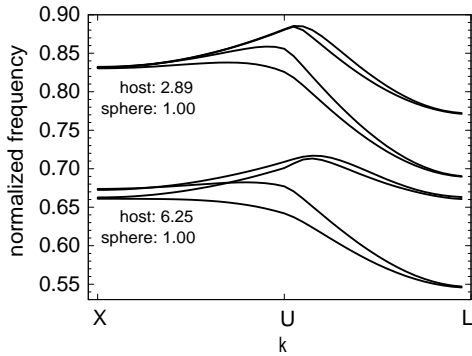


Figure 3.2: *Zoom into the band structure of an inv. opal for two different materials (see graph).*

For a different material, the bands shift according to a changed refractive index. The Fig.3.2 shows the stop gaps along the L-U-X path for permittivities of 2.89 and 6.25 comparatively. The stop gaps occur at normalized frequencies of $0.69 a/\lambda$ and $0.547 a/\lambda$. The L-U-X path equals a scan of the angle of incidence from $0^\circ - 54.7^\circ$. The larger the index contrast, the more the stop gap width is pronounced and it shifts to lower frequencies. The ratio between the stop gap positions is 5:4. With the two different permittivities the same spectral region would be affected, if the lattice constant was changed by this factor.

For example, if the stop gap center for $d = 250nm$ and $\epsilon_h = 6.25$ is found at $\omega_{gap} 0.582a/\lambda$, this equals a wavelength of $\lambda_0 = 607nm$. Although these PhC are no omni-directional reflectors with a full band gap, they can show similar properties for the discussed applications. With non-normal incidence only a slight blue-shift occurs accompanied by a

narrowing of the spectral width. However, the stop band remains because the angle of incidence on the PhC is limited by the refractive index contrast with the silicon cells. The overall onset of diffraction from k-vector conservation at the interface silicon / ITO of the inverted opal is given by:

$$\frac{\omega a}{2\pi c} \geq \frac{1}{n} = 0.294 \quad (3.1)$$

This onset is inserted into Fig. 3.1 for each crystallographic direction (solid thin, red).

Angles of incidence on 3D PhC

In the BS there is a low slope of bands when turning from Γ -L to the adjacent Γ -U direction. This differs only slightly from Γ -K and Γ -W axes in terms of angular behavior of reflectivity for sufficiently small angles. In Fig. 3.3 a section of the BS is plotted with the angles of incidence corresponding to the in-plane vector k_{\parallel} .

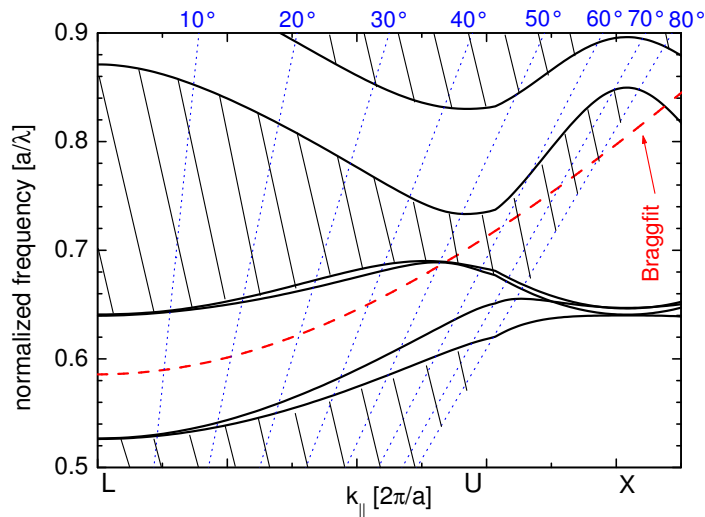


Figure 3.3: Angular mode through a section of the BS from Γ -L towards Γ -X direction ($\epsilon_{host}=6.25$, $\epsilon_{voids}=1.00$). The stop-gap follows a slight blue-shift, Bragg reflection remains significant with an increasing angle (Braggfit: dashed). Angles of incidence for an inv. opal surrounded by silicon are drawn dotted. The plotted angles of incidence from air ($0^\circ..80^\circ$) lead to angles in Si of $0^\circ..17^\circ$.

The stop-gap center at $0.58 a/\lambda$ in Γ -L direction is shifted towards $0.65 a/\lambda$. This corresponds to a blue shift of the Bragg peak. Although the central frequency of the pertinent stop gap shifts towards shorter wavelengths and its spectral width decreases at larger angles of incidence, as the BS clearly shows, both properties are of minor importance. For light incident on the cell the propagation angle within the a-Si:H layer follows Snell's law. Assuming the extremum of a flat angle of incidence $\alpha_{air} \rightarrow 90^\circ$, the angle inside the absorber layer and therefore the angle hitting the interface with the PhC is always

3 Results

smaller than $\alpha_{\text{Si}} = \arcsin(n_{\text{Si}}/n_{\text{air}}) = \arcsin(3.6) = 17^\circ$. This is equal to the escape cone. In the ROI, a-Si:H shows even higher indices of refraction. For transmission through the PhC, its effective index is valid. Incident light will hit the PhC inside the cell only within a limited distribution of angles, planar interfaces assumed. Since a narrowing stop-gap remains even for high angles, the photonic layer in this configuration does not differ much from an omnidirectional reflector.

Composite crystals

The volume filling fraction ζ is filled to 26% with a high indexed material to build the composite structure. For the permittivity, values of 6.25 and 2.89 have been considered, representing squared indices of refraction of ITO and nanoporous ZnO. The influence of the refractive index of the cores at fixed host index can be seen in Fig. 3.4.

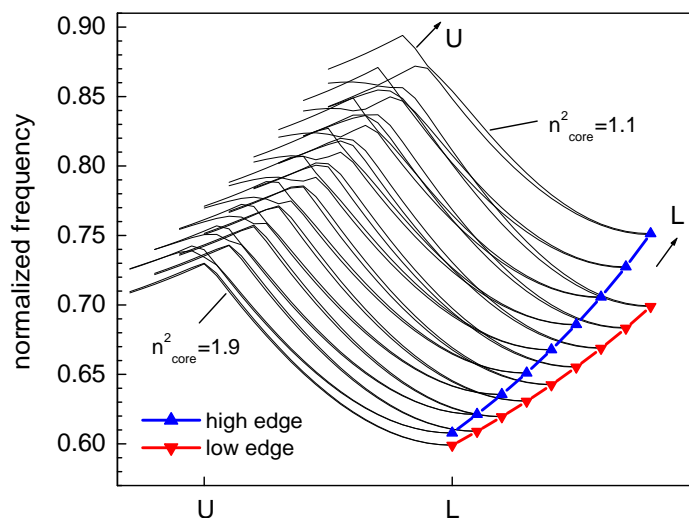


Figure 3.4: *Band structure section with the lower bands (1-4) of composite PhC $\epsilon_{\text{host}} = 2.89$, $\epsilon_{\text{spheres}} = 1.1 - 1.9$: the stop gap in Γ -L direction is observed as the core index is changed between the calculations; this happens during template removal. The curves (directions) have been shifted for clarity.*

Here, the core permittivities were varied from 1.1 to 1.9. Exactly this effect will also occur during the finalization of inverted samples. The removal of the template will reduce the effective index of the core while the template material is chemically dissolved or burned away. With ongoing removal, the photonic stop gap will blue-shift and widen up: the reflectance will become stronger. The possibility of tuning the stop gap width and matching it to the spectral demands of a solar cell will become obvious.

Conformal inverted opals

In contrast to the so far considered perfectly inverted opals, air pores will remain unfilled among the host material after a conformal inversion (conformal coating of an opal template followed by a subsequently dissolution of the template). The OHS model presented in this section has been developed in correspondence with M. Peters¹ and M. Lisca². In the fcc lattice, there are two different voids and two sorts of 'vents', 2D openings between the lattice points (the spheres). In a unit cell, there are 8 tetragonal voids (built in between four spheres arranged as pyramids and $12/4+1=4$ octagonal voids in between six spheres arranged in a two layer hexahedral ring. The hexahedral voids are arranged in an fcc lattice, while the octahedral ones form an sc lattice within the opal. The vents are triangular in $\langle 111 \rangle$ planes and squared in $\langle 100 \rangle$ planes.

PhC type	ϵ_{core}	ϵ_{shell}	r_{shell}/d	ϵ_{host}	$\omega_{gap}[\frac{a}{\lambda}]$	λ_0	$\Delta\omega$	$\Delta\omega/\omega_{gap}$
opal	2.0	-	-	1.0	0.66	642 nm	0.033	5.0%
composite	2.0	-	-	2.89	0.582	728 nm	0.021	3.5%
OHS comp.	2.0	2.89	0.565	1.0	0.6	706 nm	0.001	0.2%
OHS comp.	2.0	2.89	0.583	1.0	0.59	718 nm	0.008	1.4%
inv. opal	1.0	-	-	2.89	0.73	580 nm	0.082	11.2%
OHS inv. opal	1.0	2.89	0.565	1.0	0.755	562 nm	0.055	7.3%
OHS inv. opal	1.0	2.89	0.583	1.0	0.745	569 nm	0.064	8.6%
inv. opal	1.0	-	-	6.25	0.60	589 nm	0.115	19.1%
OHS inv. opal	1.0	6.25	0.565	1.0	0.641	551 nm	0.087	13.6%
OHS inv. opal	1.0	6.25	0.583	1.0	0.623	567 nm	0.096	15.4%

Tab.3.1: Stop gaps in $\Gamma - L$ direction for different opaline PhC: spectral position, width (Δ) and relative width ($\Delta\omega/\omega_{gap}$) are presented for different PhC. Opal templates, conformal and inverted structures are calculated, perfect ones and OHS. The Bragg peak center wavelength λ_0 is obtained for $d = 300\text{nm}$ (or $d = 250\text{nm}$ in case of $\epsilon = 6.25$). The shell radius contains the conformal thickness in units of the sphere diameter d ($r_{core} = 0.5 d$); calculated with MPB.

The spectral positions of the first stop gap and its spectral width for the investigated PhC are gathered in Tab. 3.1. A conformal deposition of material on the surfaces of an opal results in a continuous filling of the voids. The smallest vents will be closed first and the voids behind them will be encapsulated from further deposition. None of the 'inner' voids will be filled after this point. The spheres building the opal template are called *core*, while the concentric *shell sphere* is laid over a core to define a radius for the deposited shell. These are no *core shell* particles as the shell is not complete. As a consequence of the shell sphere model, the structure is denoted as *overlapping hollow spheres* (OHS). The triangular vents are filled, when the shell thickness t reaches 15.4% of the core radius. This equals a shell sphere radius of 0.577. Three points of void filling are given in Tab. 3.2.

¹Fraunhofer Institute for Solar Energy Systems, Freiburg, Germany

²Institute for solid state physics and optics, University of Jena, Germany

3 Results

void/vent	$\frac{r_s - r_c}{r_c}$ [%]	$\frac{r_s}{d}$	t [nm]
triangle	15.4	0.577	23
hexahedral	22.5	0.612	34
octahedral	41.4	0.707	62

Tab.3.2: Vents and voids of the fcc opal lattice listed by the shell deposition thickness needed for their filling with conformal deposition. The relative thickness $t = r_s/r_c$, shell sphere radius r_s and the shell thickness t for an absolute core radius of $r_c=150\text{nm}$ are shown.

The square vents are a central part of the octahedral voids, therefore they will be filled at the same point. Theoretically, all vents and voids would be filled at this point. Triangular vents in contrast will be filled before the hexahedral voids.

Filling fractions in conformal inv. opals

For a conformal coating of the opal template a smaller filling fraction than $\zeta = 26\%$ will appear (host), because of the closing pores. Typically, Monte-Carlo methods or other stochastic methods are applied to calculate precise values. It is cumbersome that literature is still lacking a simple formula to compute the ζ of this structure. For the OHS system, a model of overlapping sphere shells can be equipped with the geometrical volumes of all participating objects. For the modeling of a sample, the volumes of the overlapping

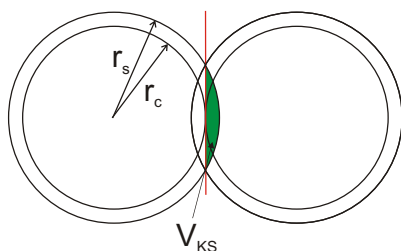


Figure 3.5: 2D schematic of overlapping hollow spheres: the overlap volume V_{KS} is a function of r_s and r_c .

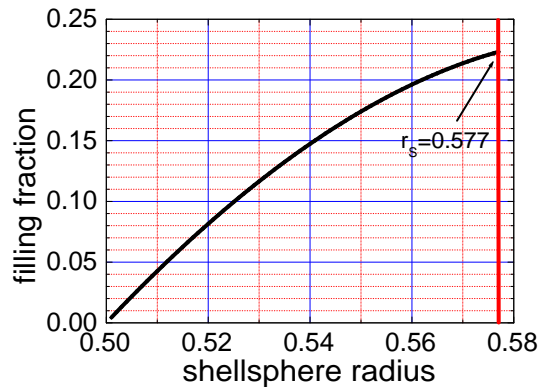


Figure 3.6: Filling fraction of the OHS shell.

shells of Fig. 3.5 are computed by reducing their ζ by the actual overlap volumes V_{KS} . This can be seen in Eq.(3.2). A graph of the filling fraction with increasing shellsphere radius is shown in Fig. 3.6. Here the overlap is only considered between the shells $r_s = r_{shell}$ of neighboring spheres with radius $r_c = r_{core} = 0.5 d$. To incorporate further neighbors, additional terms (and conditions) can be added. Equation (3.2) is only valid up to a shellsphere radius of $r_s = 0.577$, where the bent triangular 2D pores between next neighbors will close and inhibit further shell growth inside the PhC. A calculation beyond

this point is therefore not reasonable.

$$\begin{aligned}\zeta_{\text{OHS}} &= \frac{4V_{\text{shellsphere}} - 4V_{\text{core}} - 24 \cdot V_{\text{KS}}}{V_{\text{unit-cell}}} \\ &= \frac{4\frac{4}{3}\pi(r_{\text{shell}}^3 - r_{\text{core}}^3) - 24 \cdot 2\frac{1}{3}\pi(r_{\text{shell}} - r_{\text{core}})^2(3r_{\text{shell}} - (r_{\text{shell}} - r_{\text{core}}))}{(\sqrt{2}d)^3}\end{aligned}\quad (3.2)$$

Conformal inversion: influence of coating thickness

Between perfectly filled inverted opals with a host material filling $\zeta = 26\%$ and conformally coated infiltrations with lower filling fractions, there are only small theoretical differences for large deposition thicknesses. Figure 3.7 shows the first four bands between ΓL and ΓX directions for a perfect IO. The shell coatings are 10nm ($r_s = 0.53 d$) and 40nm ($r_s = 0.63 d$) of a $n=1.7$ material, the surroundings (and cores) are air ($n=1.0$).

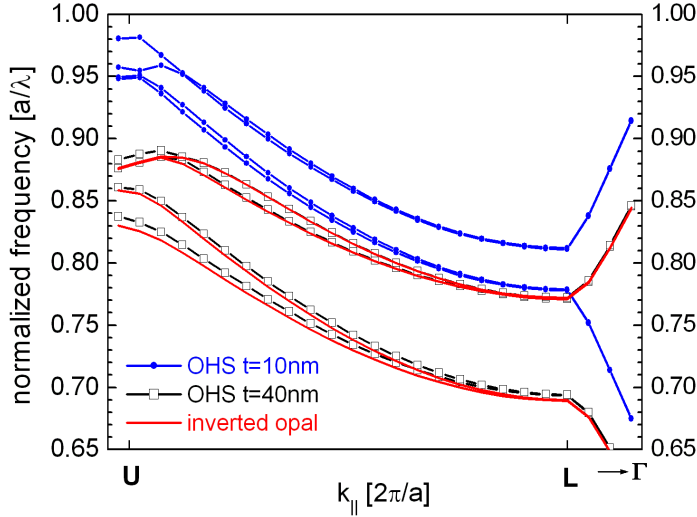


Figure 3.7: Part of the BS between L and U points for conformal inv. opals of different thickness ($t=10\text{nm}$, $t=40\text{nm}$) in comparison to a perfectly inverted opal. The difference reduces towards (theoretical) shell thickness of 40nm.

The absolute shell thickness is defined by the relative shell radius r_s/d and thus by the absolute diameter of the cores, exemplarily of $d=300\text{nm}$. From Fig. 3.7 we can see that a change in the shell thickness alters the spectral position of the stop gap. The whole band structure is shifted to lower frequencies by thicker shells. The shape of the bands however, does not experience any significant change. This influence of the shell thickness is investigated in the following. For the inverted opal, the thickness of the zinc oxide shell determines the position of the stop gap and its spectral width, as shown in Fig. 3.8 for all relevant deposition thicknesses. This calculation has also been performed for composite structures and is shown in Fig. 3.9. As Fig. 3.9 reveals, the gap position is red-shifted

3 Results

in the composite, as expected, but in between the initial opal and the resulting filled composite, the stop gap vanishes as its spectral width reaches zero at a certain coating thickness ($t=18\text{nm}$, $d=300$, with above indices of refraction). With further deposition of shell material, the stop gap width rises again, converging towards the value known from the perfect composite BS.

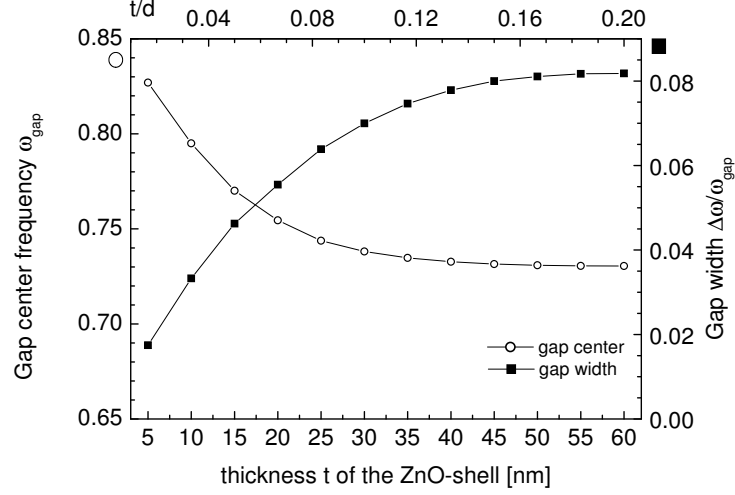


Figure 3.8: Gap map for OHS inverted ZnO opal: functions of the shell thickness $t = r_s - r_c$ ($r_c=150\text{nm}$). The gap is red-shifted to lower energies while the width increases with rising shell thickness towards the values for complete inversion for a perfect IO at $0.73a/\lambda$.

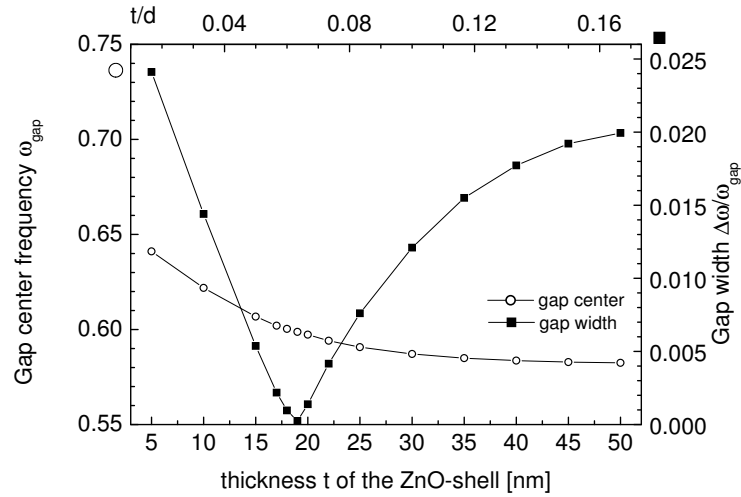


Figure 3.9: Gap map for the OHS ZnO/PMMA composite ($r_c=150\text{nm}$): the gap is red-shifted to lower energies while the width decreases to vanish at a thickness of about $t = r_s - r_c = 18\text{nm}$ and appear again. The gap approximates a perfect ZnO/PMMA composite at $0.58a/\lambda$.

3.1.2 Simulation of optical properties of inv. opal IRL

The numerical simulation of optical properties focuses on the reflectance spectra from thin-film PhC. This does not only cross the gap between the BS calculations and finite structures, but also allows the comparison of obtained simulated optical spectra with data from measurements on experimental photonic crystals. Thus, it allows a characterization and better understanding of fabricated samples.

Reflectance calculations

For a material system starting with $\epsilon_c = 2.0$, infiltrated composite with $\epsilon_h = 2.89$ and finalized inverted opal film of air spheres ($\epsilon_c = 1.0$), a 6 layer film has been modeled for SMM calculations. In comparison, the three PhC develop the spectral behavior that is expected from BS calculations. Each Bragg peak is clearly visible and their center wavelengths are found to be at $\lambda_{0,\text{opal}} = 633\text{nm}$, $\lambda_{0,\text{comp.}} = 713\text{nm}$ and $\lambda_{0,\text{inv.}} = 588\text{nm}$.

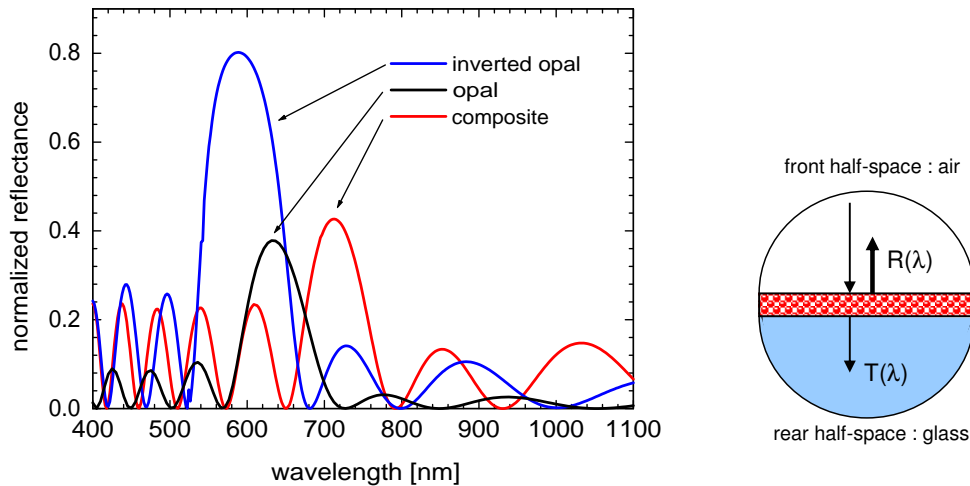


Figure 3.10: SMM calculated reflection spectra: opal, composite and inverted opal; for 6 layers ($d=300\text{nm}$) PhC on glass substrate; ($f=2$, res.64), 2nm spectral resolution. The spectral positions of template, composite and inverted thin-film structures differ significantly.

The coefficients of reflection in Fig. 3.10 can be obtained for s- and p-polarization. The effects for 90° polarized light are generally small, but they almost vanish for the composite model. The averaged index destroys the direction selectivity in the plane and introduces isotropy, leading to a certain amount of invariance against rotation of the sample.

From KKR simulations, we receive the contributions of direct (zero order) and diffracted light (here the \pm first orders) to the reflectance of the thin PhC embedded within silicon halfspaces. The resulting spectra are shown in Fig. 3.11. The contribution of first orders

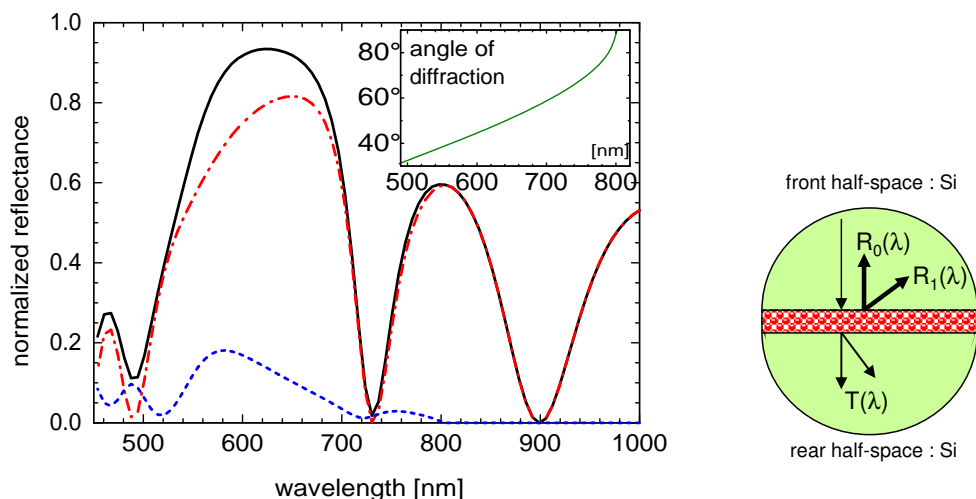


Figure 3.11: KKR calculated reflection spectra of an inverted opal; for 6 layers of ITO ($d=250\text{nm}$), zero and first order are plotted for PhC in between silicon half-spaces. The inset shows the angle of diffraction for first orders.

is lower than that of zero order, but the diffraction leads to angles that are always higher than 17° , as the inset shows between 500nm and 800nm . This makes it possible to trap light inside the a-Si top layer via total internal reflection if it can be coupled into the thin cell. The simulation uses perfectly planar interfaces and coherent excitation. As a result, the Fabry-Pérot oscillations are extremely pronounced in their magnitude.

Angle of incidence

With the calculation of bandstructures, the angle of incidence has been considered. In section 3.1.1, the course of the photonic band gap of inverted opals and the angles of incidence are treated using plane-wave expansion method along a certain crystallographic path. The influence of the angle of incidence on reflectance from the inverted opal film have also been calculated via SMM by increasing the lateral component of the incident wave vector \vec{k} (angle vs. normal incidence). For each angle, a spectrum over the visible range has been calculated, so that 2D plots are possible, as presented in Fig. 3.12. For the simulation of these spectra, the angle of incidence has been altered in the SMM code by variation of the lateral components of the incident k-vector. The PhC consists of 6 layers of an (OHS) inverted opal with shell material of refractive index $n_{\text{shell}} = 1.7$. From the BS calculations, a blue shift of the photonic reflectance peak is expected from the inverted structure. Fig. 3.12 confirms the blue-shift of the Bragg peak in finite samples. It also shows one of the neighboring thin-film oscillations which follows the blue-shift curve with increasing angles.

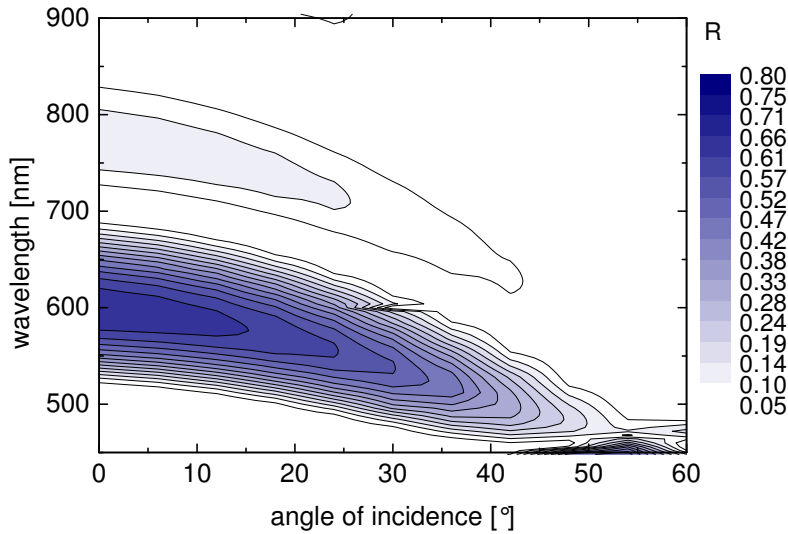


Figure 3.12: SMM calculated reflection spectra; 6 layers inverted opal: fcc ($d=300$ nm, $\epsilon_s = 2.89$) on glass substrate; $0-60^\circ$ angles of incidence.

Influence of OHS coating thickness on composite samples

For simulation of an OHS system, the virtual coating thickness of the deposited shell of $\epsilon_s = 2.89$ is being varied in small steps, covering a $\epsilon_c = 2.00$ template of $d=300$ nm core diameter. For each step of increase in thickness, a spectrum of reflectance is calculated using the scattering matrix method. The resulting family of curves is plotted in Fig. 3.13 using a false-color 2D plot.

On the left side of the graph, the opal reflectance peak is located at about 670nm wavelength. With increasing thickness of the deposited shell, this stopgap begins to close up, the reflectivity is decreasing smoothly, accompanied by red-shift. This behavior is in accordance with the predictions from the previously discussed band structure calculations, see also 3.9. At about 15 nm shell thickness the stopgap reaches a minimum while smoothly following the long-wavelength FPO. The stopgap of the inverted opal is pronounced clearly at about 8 nm in shell thickness and further increases in strength with each step to thicker shells until it becomes the dominant optical effect at about 700 nm wavelength. It follows the next FPO at shorter wavelength.

The SMM geometry features the incorporation of a glass substrate (half space) which introduces an interface of refractive index contrast at the back of the PhC. The permittivity of this substrate has been chosen as $\epsilon_{glass} = 2.25$, representing typical glasses. During infiltration the effective index of the PhC increases, as it is being filled layer by layer with high indexed zinc oxide. The effective index approximation for this scenario obeys Eq.(1.31). The squared indices (the permittivities) are as follows, shell: 2.89, core: 2.0, air: 1.0. The filling fraction of the shell can be determined with Eq.(3.2).

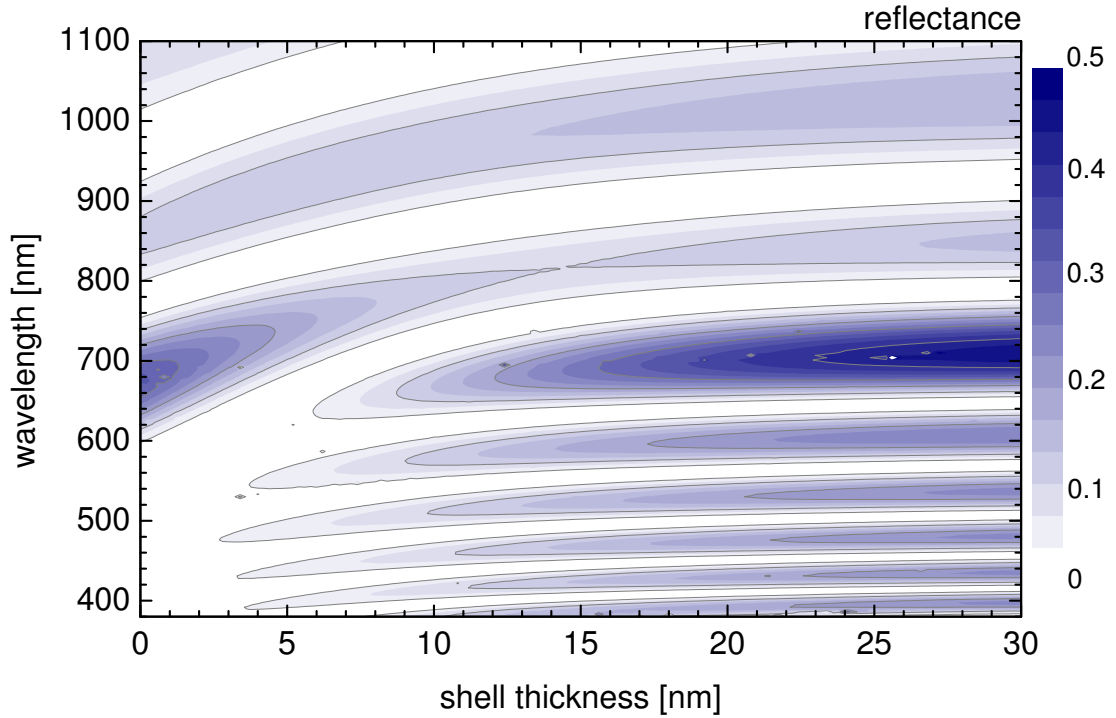


Figure 3.13: SMM reflection spectra for a composite film, 6 layers fcc ($d=300\text{nm}$, $\epsilon_c = 2.0$, $\epsilon_s = 2.89$), $f=2$, res.64, 2.91 nm spectral resolution, 0.5 nm shell increase per step. The 2D plot shows the Fabry-Pérot Oscillations (FPO) and the Bragg peak of a representative composite structure, the opaline Bragg peak starting at 670 nm at the left. Each vertical cut line is one simulated reflectance spectrum. An experimental limit to the thickness is in this case about 23 nm, according to the considerations in section 3.1.1.

The opal stopgap (shell thickness of 0 nm) is being closed while the shell grows, the inverted opal stopgap opens after that. The reflection peak red-shifts continuously with increasing shell thickness, along with the thin-film oscillations. It is displaced to shorter wavelengths between 5 nm and 10 nm of thickness, but continues to red-shift with further infiltration. Singular spots are numerical artifacts.

3.1.3 Top cell calculation: towards enhancement

To estimate the potential of enhancement by the proposed intermediate filter, a calculation of the top cell enhancement has been carried out. The resulting improvement of current-matching in a micromorph tandem will be the final goal. For now, the task of the IRL is to force an increase of the photocurrent in the top absorber and thus increase the electrical current there. The chosen photonic structure is an inverted opal made of indium tin oxide (ITO, $\epsilon=6.25$) with air voids ($\epsilon=1$). The results from KKR method (section 4.1.2) were applied to determine the reflection spectrum of a 2xABC crystal, i.e. only six colloidal layers, with the L-direction forming the face of our structure. Hereby the PhC was encapsulated between the amorphous top layer and a backside halfspace of microcrystalline silicon. Based on these optical properties of the IRL, the increase of the optical pathway inside the thin amorphous silicon top cell for normal incidence was determined. With a simple, plane-parallel model of the optical cell-cell interface we distinguish between zero order and first order effects and their optical paths. We calculate the prolongation of the path of incident photons within the a-Si:H absorber and determine additional contributions to absorption and thus quantum efficiency. Relying on experimental absorbance data of the cells and known efficiency values, we can estimate the impact on efficiency by comparison of the modified absorbance (with our PhC) to the original one (without the photonic structure). Hereby the logarithmic increase of voltage is neglected, as well as the possibility to increase the top cell voltage by re-matching the MPP.

We assume normal incidence on a plane layer geometry. The absorption of a given a-Si:H cell is $A_S(\lambda)$, the transmitted spectrum $T_S(\lambda)$. With an incident spectrum of unity (later weighted with AM1.5 spectrum), the impact of the photonic intermediate reflector is characterized simply by its reflectance in zero and higher orders R_0 , R_{1+} and the appropriate angle Θ . The absorber material is represented by an experimental absorption profile $\alpha(\lambda)$ of a-Si:H, as measured at the Forschungszentrum Jülich with thermal deflection spectroscopy³. In Fig.3.14(B), a schematic drawing of the model is shown. The use of Lambert-Beer's law of absorption leads to Eq. 3.3

$$\begin{aligned} T_S &= \exp(-\alpha t) \\ A_S &= 1 - T_S \end{aligned} \quad (3.3)$$

The spectrally selective reflectance (zero order) from the PhC leads to increased photocurrent in the top absorber, which further leads to additional absorption A_0 . The light path is the optical thickness of the cell (t). Eq. 3.4 contains the enhancement from the specular (zero order) reflectance.

$$\begin{aligned} A_0 &= \exp(-\alpha t_a) \times R_0(\lambda)(1 - \exp(-\alpha t_a)) \\ &= T_S(\lambda) R_0(\lambda) A_0(\lambda) \end{aligned} \quad (3.4)$$

The diffractive properties produce a term A_{1+} , respectively. Higher order diffraction leads to angles Θ leaving the optical axis of normal incidence. Light that re-enters the top absorber this way from the PhC experiences total internal reflection on the front of the a-Si:H layer, if the angle is large enough. After being reflected there, it hits the

³Dr. R. Carius, IEF-5, Forschungszentrum Jülich

3 Results

PhC again. So, the worst case for light coupled into the top cell (I_{1+}) by the PhC is being diffracted into the layer, experiencing one internal reflection on the front and being diffracted out again by the PhC towards the front side. This is a consequence of reciprocity of the optical path. The best case is full absorbance and being internally reflected in the absorber towards infinity. The inset in Fig.3.11 shows the spectral behavior of the diffraction angle for first order (inside the a-Si:H layer). With our region of interest lying between 500nm and 700nm, this angle is always higher than 30° . With the angle of total internal reflection in silicon being $\sim 17^\circ$, these photons remain inside the solar cell until they are fully absorbed or diffracted out again by reverse diffraction via orders $1+$. Fig. 3.14(A) shows the intensity distribution along multiple internal reflections in the absorber. For photons trapped inside the a-Si:H this way, transmission through the

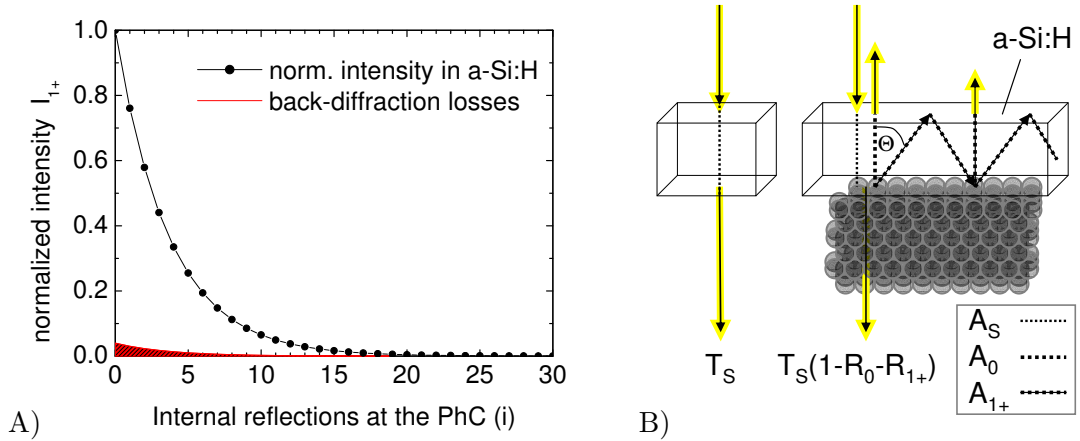


Figure 3.14: A) monochromatic intensity of diffracted light in the top absorber and related back diffraction losses, B) schematic optical paths of top-cell enhancement model with and without PhC.

PhC is about 10^{-4} and less for zero order diffraction and 10^{-3} for higher orders because of the high propagation angles and the high reflectivity: transmission is being neglected. Back diffraction at the PhC itself is the dominant loss mechanism for photons trapped in the absorber by higher orders. The equation (3.5) applies these losses every two internal reflections. The optical pathway of diffracted light in a-Si:H in between is $2t/\cos\Theta$.

$$\begin{aligned}
 A_{1+} &= 1 - \frac{I_{lost}}{I_{1+}} \\
 &= 1 - \sum_{m=0}^{\infty} (1 - R_{1+}(\lambda))^m \times \exp\left(-m \frac{2\alpha d}{\cos\Theta}\right)
 \end{aligned} \tag{3.5}$$

The numerical calculation according to (3.5) is shown in Fig. 3.14(A), after 20 internal reflections at the PhC only a small part of the light caught inside the a-Si:H layer is lost and the remaining intensity drops to 10^{-4} of the incoming. It is a result of the rather low diffraction efficiency. At $\lambda=696\text{nm}$, only 4% of incident light is caught by diffraction, but also only 4% of this intensity in the a-Si:H cell will get out again the same way. The resulting impact of the proposed photonic structure is the sum of zero (A_0) and higher

order (A_{1+}) effects on the absorbance of the standard cell (A_S), written in Eq.3.7.

$$A = A_S + T_S R_0 A_0 + T_S R_{1+} A_{1+} \quad (3.6)$$

$$\begin{aligned} A &= 1 - T_S(\lambda) \\ &+ T_S(\lambda) R_0(\lambda)(1 - \exp(-\alpha d)) \\ &+ T_S(\lambda) R_{1+}(\lambda) A_{1+}(\lambda) \end{aligned} \quad (3.7)$$

Comparison of the standard a-Si:H layer absorbance and the increased absorbance of the PhC-mounted structure is shown in 3.15. It clearly shows an enhanced absorption

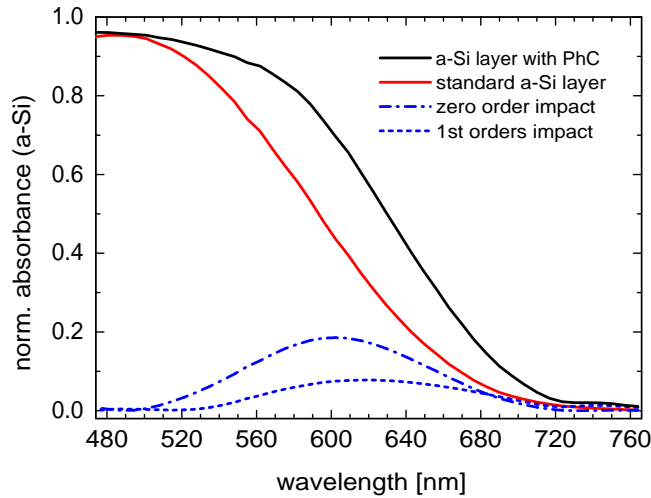


Figure 3.15: Calculated absorbance increase: the a-Si:H top-cell's normalized absorbance is shifted towards longer wavelengths. Contributions from diffraction orders 0 (dotted&dashed) and 1+ (dashed) are drawn.

profile towards the red regime, caused in 2/3 by the specular and in 1/3 by the diffractive reflectance of the IRL. Calculations with experimental absorption data and standard AM1.5 solar spectra, combined with the simulation stated above promise an increase in current density from the a-Si:H cell of about $1.8\text{mA}/\text{cm}^2$. For a single a-Si:H cell alone with $j_{sc,a}=12\text{mA}/\text{cm}^2$ and $V_{oc,a}=0.95\text{V}$ (FF=0.7) this equals an increase in efficiency from 8.0% to 9.2%. The experimental absorbance data used herein refers to a 410nm thick a-Si:H cell, while cells used in tandems are usually limited to about 250nm thickness to restrain degeneration. Since absorption decreases with smaller thickness, the impact of our structure will gain more and more weight, the thinner the a-Si:H cell is. Even in a 250nm thin cell, the current increase will still be about $1.44\text{mA}/\text{cm}^2$. Since this enhancement of a top-cell also increases the limiting current, it will furthermore increase the overall output of a tandem.

A silicon tandem cell with scattering front (random rough), with $j_{sc}=12.1\text{mA}/\text{cm}^2$ and open circuit voltages of $V_{oc,a}=0.91\text{V}$, $V_{oc,\mu c}=0.5\text{V}$ reaches 11.1% in efficiency (FF=0.65).

3 Results

The current increase of our spectral splitting diffractive layer in this cell would affect both junctions and results in an efficiency of 12.4%, i.e. an absolute increase of 1.3%. Thicknesses of the intrinsic layers here are 270nm and 1.35 μ m. Data from the results of this calculation are summarized in the following tables.

cell	thickness	V_{oc} [V]	j_{sc} [$\frac{mA}{cm^2}$]	FF	η
a-Si:H (single)	410nm	0,95	12	0,7	8,0%
a-Si:H (top)	250nm	0,85	12	0,7	10,1%
μ c-Si (bottom)	$\sim 2\mu$ m	+0,35			

Tab.4.3: typical data of both junctions in the tandem, as used for efficiency calculation

cell	thickn.(a-Si)	IRL	j_{sc} [$\frac{mA}{cm^2}$]	η
a-Si:H (single)	410nm	-	12,0	8,0%
a-Si:H (single)	410nm	✓	13,8	9,2%
a-Si:H + μ c-Si	250nm	-	12,0	10,1%
a-Si:H + μ c-Si	250nm	✓	13,4	11,2%

Tab.4.4: impact of the IRL on currents and efficiencies of a single a-Si:H cell without further back side reflector and on the tandem.

3.1.4 3D PhC IRL enhancement potential

With rigorous diffraction theory (FMM), the local absorption of an a-Si:H layer of 200 nm thickness has been calculated and integrated subsequently. The bottom cell is of μ c-Si, both cells of refractive index $n_{Si} = 3.6$. The irradiation is AM1.5. Focus lies again on the absorbance of the top cell only, since the achievement of maximized enhancement there is the primary goal of the IRL. A tailoring towards current matching, such as offered by an adjustment of the bottom cell thickness, is to be treated later. A large contrast in the refractive index of the PhC was chosen: $n_{sphere} = 1.0$, $n_{host} = 2.5$, with a six layer inv. opal film. The results of this section have been obtained in cooperation with Dr. C. Rockstuhl.

The possible enhancement is quantified in order to classify the potential of the 3D PhC IRL approach compared to a top cell without any IRL device. The plain number of absorbed photons is plotted in Fig.3.16(A) resolved for the wavelength and depending on the sphere radius as the variable design parameter. Each vertical cutline in Fig.3.16(A) is one absorbance spectrum of the a-Si:H cell. In Fig.3.16(B), the enhancement is plotted as a function of the (air) sphere radius. The obtained curve shows different parts of enhancement. They will be addressed in three zones in the following.

(1) At small radii, the enhancement oscillates around an average of about 1.12, which corresponds to the shifting of FPO by altered thickness of the PhC with changing radius. The state-of-the-art IRL addressed in section 1.2.1 can be considered operating in this enhancement regime of zone (1). The tuning of IRL thickness which is here a by-product of simulating different sphere radii can give access to optimized spectral position of one selected Fabry-Pérot Oscillation (FPO). This results in a local maximum of enhancement,

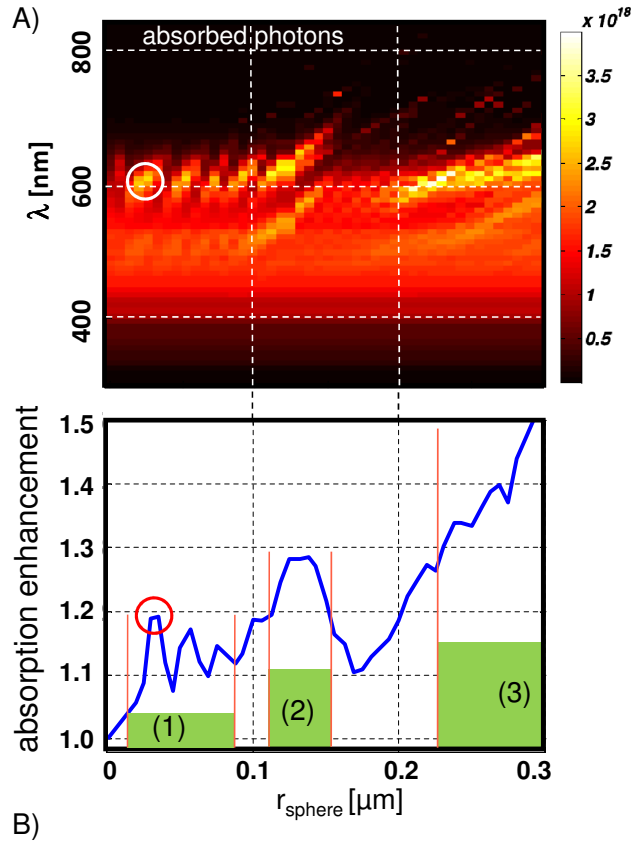


Figure 3.16: *top cell photon absorption and the enhancement caused by the 3D inverted opal PhC ($n_{\text{host}}=2.5$). In zone (1) the IRL acts analogous to a homogeneous layer of effective index: the wavelength can not resolve the periodicity of the PhC. At intermediate sphere radii ($r \approx 130 \text{ nm}$) the inverted opal IRL exhibits a selective reflectance, the corresponding enhancement is zone (2). It also produces back diffraction at the 3D PhC lattice with increasing sphere radii, leading to very strong enhancement in zone (3).*

encircled in Fig.3.16.

(2) The discussed zero order Bragg reflection of the inverted opal is evident around sphere radii of $r_{\text{sphere}} \approx 130 \text{ nm}$ and produces a plateau with an enhancement factor of 1.28, which defines zone 2. This is in focus of this work and is very well expected from the simulations presented in the sections before. This zone has been deliberately chosen to contain only enhancements above the values that are also achievable within zone 1.

(3) Interestingly, with increasing radius, the enhancement reaches even higher factors of up to 1.5 as calculated so far. This zone has been chosen to frame only enhancements above the values reached within zones 1 and 2. The observed enhancement is attributed to the strong impact of diffraction, particularly that of coupling into guided modes within the a-Si:H absorber layer (hot spots in Fig.3.16(B)). It is very likely, that the increase of enhancement with rising sphere radius is followed continuously to even larger factors.

3.1.5 Tandem cell calculation: towards current matching

After the potential of this approach has been validated for a single junction of a-Si:H and a contribution to the efficiency can be expected, the principle nature of the IRL mode of operation has to be studied for a tandem cell. With the region of interest (ROI) defined by the two EQE, the influence of a PhC reflectance spectrum $R(\lambda)$ can be investigated by a simulation of the photon distribution between top and bottom cells, in order to define a preferred spectral shape, position and width. The first goal is achieving current matching between both junctions, keeping in mind that any ‘surplus’ enhancement of the top cell is encouraged thoroughly.

The cell properties are represented by their EQE data in Fig.1.5. Together with the spectral irradiance $I(\lambda)$ from AM1.5 spectrum (ASTMG173, by NREL ⁴) they contain the amount of photons per second per wavelength interval converted to electric current by an illuminated area of 1 m^2 . The irradiance has to be recalculated to a spectral photon flux density by dividing by the photon energy as in (3.8).

$$\phi(\lambda) = \dot{n}_\gamma(\lambda) = I(\lambda) \cdot \frac{1}{E(\lambda)} = I(\lambda) \cdot \frac{\lambda}{hc} \quad (3.8)$$

The reflector influences quantum efficiency by a change of ΔEQE :

$$\Delta EQE(\lambda) = (1 - EQE(\lambda)) \cdot R(\lambda) EQE(\lambda) \quad (3.9)$$

Since the used spectrum consists of measured data, the irradiance is not a spectral differential dI , but a difference ΔI . Therefore, the integrated short-circuit current density [A/m^2] over all measured wavelength intervals is equal to the sum:

$$j_{sc} = q_e \int_{\lambda} \Delta \phi(\lambda) EQE(\lambda) d\lambda = q_e \sum_{\lambda} \frac{\lambda}{hc} \Delta I(\lambda) EQE(\lambda) \Delta \lambda(\lambda) \quad (3.10)$$

The complete tandem current in this model is given by (3.11).

$$j_{sc} = \sum_{\lambda} I(\lambda) (EQE_a(\lambda) + EQE_{\mu}(\lambda)) \quad (3.11)$$

This means, that in Fig. 3.17, the flux behind the the top cell (ϕ_1) can not be used for considerations of the bottom cell’s EQE: here ϕ_0 has to be applied again. For the reflectance calculation however, we have to use $\phi_1 = \phi_0(1 - EQE_{n,a})$, illuminating the PhC. The reflected flux is $\phi_R = \phi_1 \cdot R(\lambda)$. Here, the difference between internal and external quantum efficiencies is neglected: the flux (ϕ_1) would in a complete model also be reduced by all recombination losses in the top cell. The transmitted flux density, hitting the bottom absorber underneath the IRL, is $\phi_T = \phi_0(1 - R(\lambda))$. The $EQE_{n,a/\mu}$ are normalized efficiencies, divided by the maximum of the EQE of the a-Si:H cell ($EQE_{max} = 0.762$) for normalization. The equations (3.13), (3.14) for the resulting short-circuit currents read:

$$j_{sc,a} = q_e EQE_{max} \sum_{\lambda} [\phi_0(\lambda) \cdot EQE_{n,a} (1 + R(\lambda) (1 - EQE_{n,a})) \cdot \Delta \lambda] \quad (3.13)$$

$$j_{sc,\mu} = q_e EQE_{max} \sum_{\lambda} [\phi_0(\lambda) \cdot (1 - R(\lambda)) \cdot EQE_{n,\mu} \cdot \Delta \lambda] \quad (3.14)$$

⁴available at <http://rredc.nrel.gov/solar/spectra/am1.5/ASTMG173/ASTMG173.html>

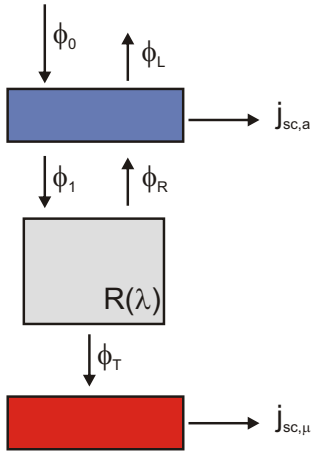


Figure 3.17: Schematic flux densities in the tandem model.

The IRL introduces the reflectance $R(\lambda)$, as shown in Fig 3.17. The resulting dimension in Eq.(3.8) is a spectral flux density of dimension $nm^{-1} m^{-2} s^{-1}$: the photon flux density ϕ . After multiplication with the EQE of dimension unity in Eq.(3.12), the investigated quantity is therefore the spectral flux density of converted photons, which is (by factor of the electron charge q_e) equal to the spectral short circuit current density $j_{sc}(\lambda)$.

$$j_{sc}(\lambda) = q_e \phi(\lambda) \cdot EQE(\lambda) \quad (3.12)$$

The experimental EQE have been measured on a tandem cell, but independently for top and bottom junction. In consequence, the bottom cell EQE data already contain the absorption of the top cell.

Generally, the assumption of $1 - EQE$ being the illumination weight on the IRL would be incorrect, because we ignore all losses in the top cell and at the front side in this term. The used EQE however, were measured at modules with cover glass (the substrate) and front contacts. In our case the EQE is additionally normalized and then applied to photons before and after reflection at the IRL. Therefore, the losses in the top absorber are included in the model in first approximation.

Current matching is simply the condition $j_{sc,a} = j_{sc,\mu}$ or $\Delta j_{sc} = 0$. To implement different filters, only the reflectance function $R(\lambda)$ has to be exchanged. The first function is an ideal square pulse (Fig.3.18, left), characterized by its reflectance R_{max} , its spectral position λ_0 and width $\Delta\lambda$.

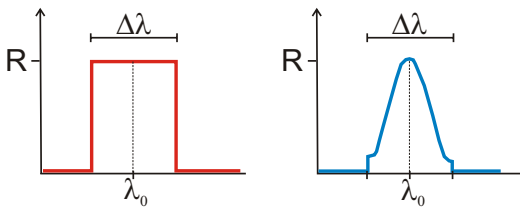


Figure 3.18: Square pulse and inverted opal pulse reflectance profile.

For constant $R = 25\%$, $R = 50\%$ and $R = 75\%$, the resulting map is plotted in the next Fig.3.19. The condition of current matching enters all plots in Fig.3.19 with a steep vertical curve. The IRL filter function is partially neutralized by the dominating absorption of a-Si in the short wavelength region. Below $\lambda = 550 \text{ nm}$, the IRL has no effect.

The plots in Fig.3.20 show furthermore, that with only 25% of reflectance, a pulse width of 150nm is necessary in order to satisfy current matching condition. It would have to be located between 650nm and 700nm in center wavelength. With increasing reflectance, the range of acceptable spectral positions can be extended from about 600nm to 750nm. A narrower reflection peak can be also sufficient: with $R=75\%$, only about 50nm width is required. An interpolation will be linear, as obviously the photon flux increase is linearly affected by both, the spectral width and the reflection coefficient.

3 Results

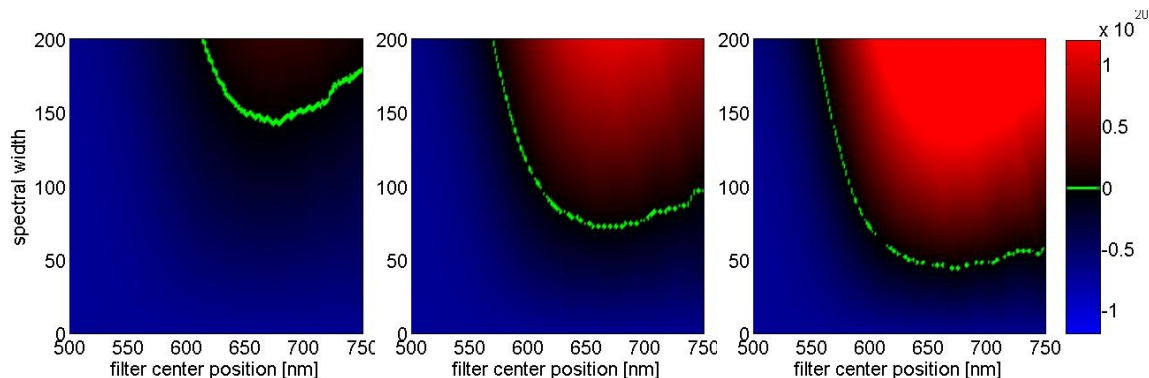


Figure 3.19: Photon flux difference map (a-Si) for a square pulse reflectance filter (colormap 'liquid pork'); R=25%, R=50%, R=75%. Spectral width and position are varied, the green line marks current matching condition.

In conclusion, a range of 50nm to 150nm spectral width and an appropriate reflectivity between 75% and 25% appears to be sufficient from the square pulse model. The formation of a flat current matching condition with constant reflectance in the red regime is remarkable.

A less ideal filter function is the measured reflectance of an inverted opal, it is cut to zero at the minima on each flank of the Bragg peak (Fig. 3.18, right). The FWHM is not suitable here, as there is a base reflectance (minima at flanks are not zero), so $\Delta\lambda$ is defined as the base width. The ratio of the spectral region covered by these functions is given by their area [nm]. The inverted opal reflectance covers 57% of the area of a square pulse of same $\Delta\lambda$. The used data shows a Bragg peak with $R_{\max} = 0.73$ and $\Delta\lambda = 175\text{nm}$. Using a constant shape of the reflectance, the parameters of maximum reflectance (peak height) and spectral position have been varied. The results are plotted in Fig. 3.20. In contrast to the ideal square filter, the opal function covers only about half the spectral-width-times-reflectance area. The back reflection losses caused by non total absorbance by the a-Si:H cell of internally reflected light can be found on the right graph of Fig. 3.20.

Here instead of the photon numbers, the normalized short-circuit current ratio ($(j_{\text{sc},a} + j_{\text{sc},\mu}) / \sum j_{\text{sc},\text{initial}}$) is shown. Assumed planar interfaces and the lack of light-trapping structures lead to strong losses at high reflectance. The further the band stop is placed in the red regime of the spectrum, the heavier these losses become. For values of $R_{\max} \approx 0.6..0.8$, a peak center position close to 550nm is suited. High reflectance and narrow bandwidth of this 'green' regime reduce the bottom cell losses down to 1%! Losses are here the reductions caused by back reflection that do not contribute to top cell enhancement. A lower reflectance of about 25% would be sufficient at longer wavelengths ($\approx 670\text{nm}$). However, increased back reflection losses of 4% in the bottom absorber are the consequence. These losses are a clear disadvantage that would have to be compensated by the bottom absorber. An advantage of this 'red' regime however, is the horizontal flat curve of current matching condition between 640nm and 700nm in Fig.3.20(A). It provides a quasi-invariance against the blue-shift of the photonic Bragg peak, as any blue-shift of the center position is tolerated within the spectral limits by the condition of $\Delta j_{\text{sc}} = 0$. The peculiarities found

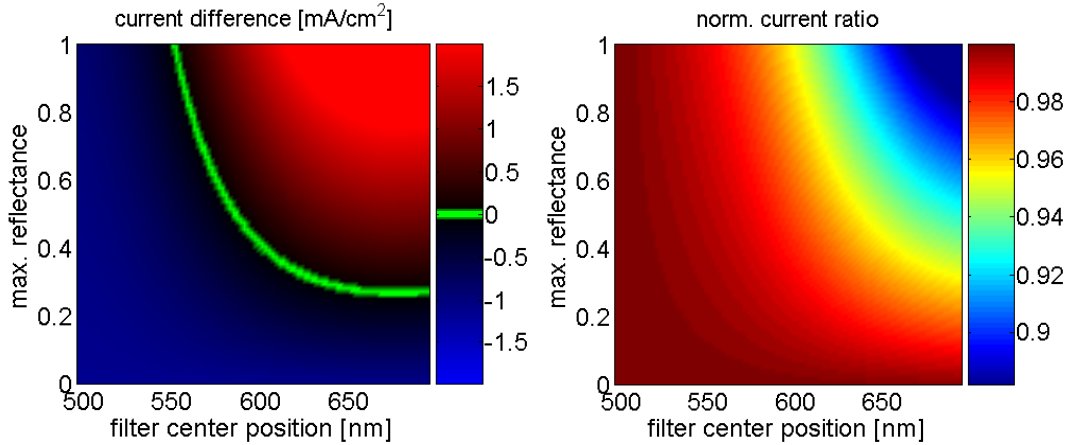


Figure 3.20: (left) Short-circuit current density difference map for use of the inverted opal filter: the green line indicates the course of current matching condition $\Delta j_{sc} = 0$. Between 650 nm and 700 nm of wavelength, an invariance of the reflectance maximum against alteration of the filter center position is observed. This spectral region is defined as the ‘red’ mode of operation and should be considered favourable for the final desing of the IRL. The second graph (right) is the according normalized short-circuit current ratio map expressing the relative current difference between the IRL equipped tandem and the bare tandem: values below unity express back reflection losses from insufficient a-Si:H absorption.

in the square pulse model are generally repeated. The developed tandem flux model is a parameterized description of the impact of zero order IRL that can incorporate arbitrary functions of reflectance. The use of a specular IRL can provide the increase of illumination (and absorption) in the top absorber of a tandem cell. Two possible working points have been identified: the green regime (close to 550nm) and the red regime (650nm-700nm).

The green regime offers low back reflection losses for the bottom cell. It slightly reduces thermalization in the bottom cell because it filters at shorter wavelengths. Also, it requires sharp band stop filtering and generally higher spectral precision of the IRL properties. After first considerations, the green regime would be preferred, as it does not introduce additional losses.

In the red regime, μc -Si illumination is reduced by higher back reflection losses, but it offers a stable region for the spectral properties. Further, the red regime needs only small amplitudes in reflectance. The 3D PhC approach offers surplus potential as it is able to provide higher reflectance than required. Thus, the red regime appears more suited to be applied in the tandem solar cell.

For an inverted opal (OHS) with a shell permittivity of $\epsilon = 2.89$, the green regime is achieved with sphere diameters of about $d = 270nm - 300nm$. The red regime is obtained with sphere diameters of $d = 340nm - 360nm$.

Intermediate summary II: Numerical results

The analysis of the **photonic band structure** of inverted opals focuses on the stop gap in Γ -L direction which allows gap width tuning via index contrast and spectral matching via the lattice constant (sphere diameter). The influence of refractive indices and filling fractions are investigated. An increasing angle of incidence leads to blue-shift and narrowing of the stop gap, but is limited within a silicon surrounding. The difference between ideal inverted opals and conformal ones was analyzed in detail. Conformal inv. opals suffer from reduced stop gap width, although sufficiently thick shells show up to 75% of the ideal relative band width. An analytical formula to connect shell thickness and filling fraction, and thus the effective index, was derived. From the results of the **optical simulations** and top-cell and tandem calculation, we can expect the inverted opal IRL to be capable of fulfilling the optical requirements of the intended application sufficiently well. The reflectance of inverted and composite samples can cover a wide range of amplitudes and widths. The selective reflectance is placed in the correct spectral regime, using an inverted opal of host index $n=1.7$ and $d \approx 300 \text{ nm}$ sphere diameter. One key feature to strong enhancement of the thin-film top cell observed in the simulations is non-specular reflectivity, as the impact of diffraction shows: back-diffraction can increase absorption in the top cell dramatically. The expected current increase in the top absorber contributes more than 1% absolute to efficiency and is therefore sufficiently high to motivate further investigation. The calculated optical current matching shows within the spectral region of interest **two spectral working regimes** ('green' and 'red'), both of which can be covered by the proposed PhC according to the numerical investigations so far.

3.2 Fabrication of the photonic crystal IRL

3.2.1 Developed technical solutions

Artificial opals have been fabricated as thin films on glass and silicon substrates via methods of dip coating, knife coating or simply controlled drying after droplet evaporation. In Fig. 3.21, the dip-coating setup is shown (left). It was constructed along with the horizontal knife coating setup in Fig.3.21 (right) which was also built.

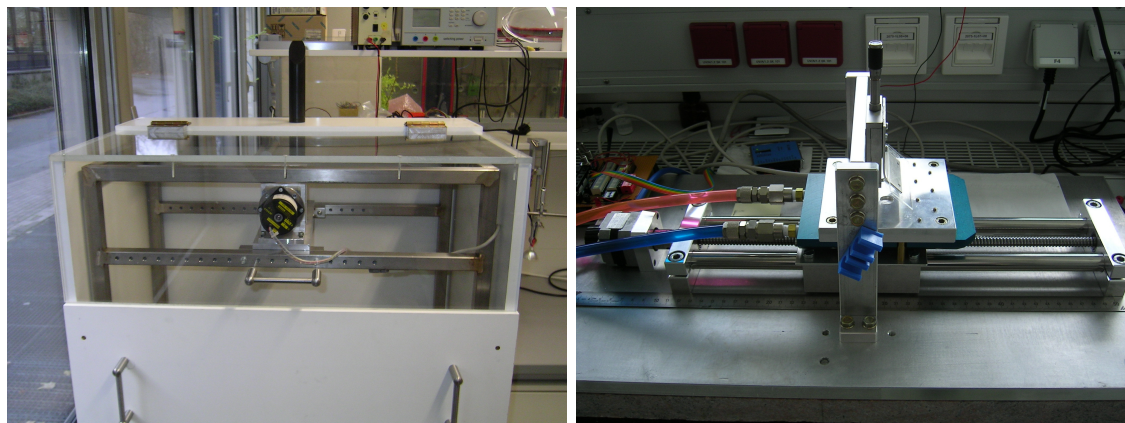


Figure 3.21: Photographs of dip-coating setup (left) and rapid coating setup (right).

The dip-coater features a stepper-driven winch on an antishock supported steel frame in an enclosed protective housing. It pulls the substrate on a $50\ \mu\text{m}$ Invar wire⁵ out of a colloidal suspension. The suspension can also be heated or carefully stirred. The velocity range of the drive unit is about $0.5\ \mu\text{m/s}$ to $2.0\ \mu\text{m/s}$. This is achieved via a special gear box setup with a 1:250000 ratio. There are five different diameters on the winch, which allow five different ranges of velocity with the same drive. Consequently, the device can process several samples parallel - with different velocities. The main task of this device is the production of high quality opal films with control of their thickness.

The knife coating setup consists of a fixed knife and a micro controller triggered linear sled on smooth polymer bearings, carrying the substrates. Constant substrate temperature control is maintained by a Haake thermostat of type K20 (DC30) which is feeding the substrate carrier. Sample sizes up to $100\text{mm}\cdot 100\text{mm}$ are possible to process within 60 seconds. Alternatively, three microslides ($75\text{mm}\cdot 25\text{mm}$) can be processed simultaneously. The main task of this device is the control of the deposited film thickness in a rapid coating process with high velocities. The device is addressed as rapid opal layer assembly setup (ROLAS).

⁵supplier: Goodfellow Cambridge Limited

3.2.2 Thin-film samples from rapid opal layer assembly setup

While dip-coating methods are considered state-of-the-art for colloid crystal growth, some results from knife coating experiments of thin-films are presented here.

The experiments from room temperature up to 50°C show a very good control of the film thickness, as the left picture below, Fig.3.22(A), shows. However, the crystalline quality strongly varies with the details of drying and the actual environmental conditions. The growth of sub mono layers (see Fig.3.22(B)) also show the good control of thickness

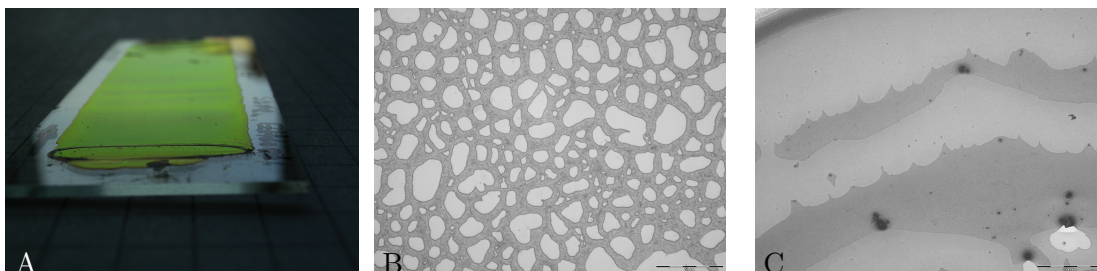


Figure 3.22: ROLAS samples: (A) very smooth film on microslide glass; microscope views (M=20): (B) sub monolayer film, (C) 1-2 layer film.

that is possible with this method. Fig.3.22(C) shows a monolayer, partially covered with a second layer (darker regions). Here the amount and concentration of colloid did not match the monolayer condition for the coated area. A stick-slip motion of the drying meniscus then forms the alternating steps in thickness. The use of rather high volume fractions (>10%wt), at high coating speeds of several mm/s with moderate temperatures close to R.T. produced the best films so far.

3.2.3 Template removal

The final sample development is achieved by a cycle of bathing in THF (tetrahydrofurane) and heating in a furnace. Samples with only a thin ZnO coating can be developed faster, as the solvent can infiltrate the PhC easier. A bathing in THF overnight followed by rinsing in fresh THF and final tempering is sufficient. For massively coated samples, the removal can take up to two days in a thermal and chemical dissolution cycle. Typical parameter ranges for these processes are listed in the following table on temperature range T and duration of exposure t .

	low T [$^{\circ}C$]	high T [$^{\circ}C$]	min t [h:min]	max t [h:min]
chemical	R.T.	75	0:30	12:00
thermal	130	220	0:15	3:00

Tab.4.6: Parameter range for the template removal, chemically and thermal.

Exposure to a heated THF is more efficient than the chemical bath at room temperature (R.T.). A glass confinement can be also used to evaporate the THF and create a saturated atmosphere of this solvent: a dynamic equilibrium of liquid and vapor phase is built. This way, the permanent exposure of the sample to THF-molecules of high kinetic energy from the vapor phase speeds up the infiltration with the THF. Bathing in liquid THF is still necessary to flush the diluted polymer out.



Figure 3.23: Microscope photographs of sample between two removal baths (left) in bright field and (right) the in dark field observed chemical removal frontier.

In Fig. 3.23 the optical change during developing the sample is obvious. From a brownish appearance in reflection microscopy, the sample changes to become highly reflective, leaving the impression of a brilliant golden color. The dark spots in the left photograph are areas of incomplete removal. In DF (right picture), the dark area is also the undeveloped zone. The removal seems to increase scattering within the sample, the nano-crystalline nature of ZnO becomes visible in dark field illumination.

3.2.4 Size parameters

With the fabrication, a brief view on the actually used structural size parameters is mandatory. The applied colloidal suspension of $d = 300 \text{ nm}$ quite matches the spectral requirements derived in chapter 1: According to Eq.(1.36), the Bragg peak of conformal inverted opal films is expected close to 600 nm in wavelength. The lattice size of the fabricated samples is therefore in general suited for the spectral region of interest which was identified in section 1.4.2.

Consequently, a single colloidal suspension has mainly been used throughout the fabrication process towards IRL to allow the comparison of samples.

3.3 Structural investigation

3.3.1 Structural disorder in opal samples

Deviations from order in the PhC occur in the bulk or at surfaces. They can be localized or global. Multi-crystallinity is not a problem for the intended application, amorphous regions are. Where the order is disturbed, the photonic band gap will not develop to its full width, it even may not even occur at all. Structural analysis of fabricated samples is therefore constantly necessary. The SEM pictures in Fig.3.24 show examples of disorder found in opal samples. The SEM graph (A) shows firstly a typical arrangement of spheres

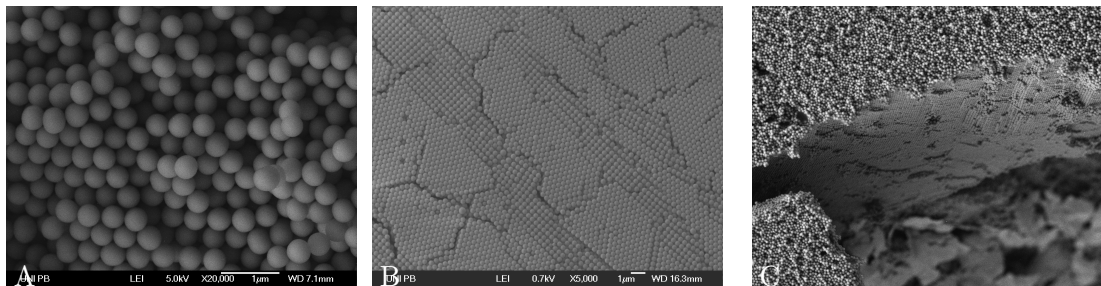


Figure 3.24: SEM graphs of opal samples: (A) broken edge of an opal crystal, (B) square-ordered intersections appear on surface of thin-film opals, (C) amorphous surface on a crystalline bulk opal.

in the 3D lattice, disorder is caused by breaking the sample to get view on this cross-section. Point defects and few line defects at grain boundaries are also captured in this picture. Second, in (B), intersections of different crystal order are neighboring in one film: instead of typical sixfold orientation, a square lattice has formed on the surface. This can be for example fcc in Γ -X direction. It occurs at steps, when the number of layers increases during fabrication, or when random variations in the crystallization velocity or concentration occur and introduce the equivalent of shear forces in the growing crystal. Graph (C) shows a bulk opal crystal of several hundreds of layers of well grown crystal lattice. The surface, however, is completely distorted and amorphous - a result from far too rapid drying at the end of a sedimentation process. Such a sample appears milky to the naked eye, as the top layers produce strong scattering. However, it also exhibits strong Bragg peaks, because its bulk lattice is highly ordered. Since these optical properties allow the verification of a success of fabrication procedures, consequences of disorder in transmission and reflection will be briefly discussed within the following section.

3.3.2 Drying cracks

The grain boundaries of opal crystallites become clearly visible under the optical microscope, even at low magnification ($M \approx 10+$). They appear as dark lines in reflection

microscopy, while they are very bright in transmission. However, to get good measure of how homogenous an opal film has grown, dark field objectives should be used. The Fig. 3.25 show a bright field ‘BF’ (A) and dark field ‘DF’ (B) photograph of the same field of view ($133\mu\text{m} \times 100\mu\text{m}$). The sample is made of PMMA beads that have been cross-linked by adding EGDMA to the suspension. The substrate is a standard microslide glass.



Figure 3.25: BF (A) and DF (B) microscope views of a PMMA opal sample: the cracks become visible in DF, but as well the very fine structures of small scratches and defects can be seen; DF illumination uses scattered light to identify inhomogeneities (Olympus BX51, M=100 objective, NA=0.9). (C) shows a thin-film opal on silicon under SEM with pronounced drying cracks.

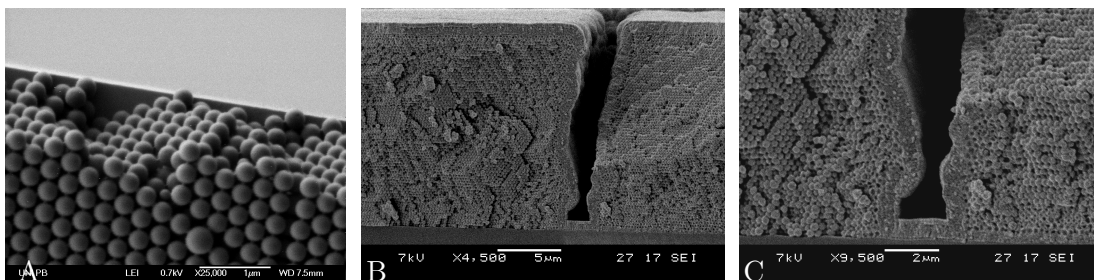


Figure 3.26: A) higher magnification of the thin-film sample; B), C) ZnO coated opal: the massive deposition (CVD) was successful from top to bottom of the film and also coated the substrate, connecting it to the top surface (JSM6060).

On the high optical magnification shown here, the fine roughness, defects and stacking faults at the sample’s surface become visible. The side illumination in (B) leaves only the scattered shares of light to the eye of the beholder and shows point defects via scattering. Even the 60° angles between boundaries within crystallites become visible, although the small size of the spheres lies below the optical resolution limit for direct observation. Drying cracks are smaller but appear more frequently with thinner samples. Fig. 3.25 (C) and 3.26 (A) show a thin-film sample observed in SEM. The film of constant thickness of eleven layers was produced with the dip-coating setup. It shows the drying cracks forming their wide-spread grid. Point defects and few line defects at grain boundaries are also captured in these pictures. A drying crack that extends from top to bottom of the (inv.) opal film can be infiltrated with TCO in a massive deposition (CVD). Fig.3.26 (B) and (C) show the successful experimental crack-filling results in SEM cross-section views of a

cleaved sample ⁶.

3.3.3 Inverted opals

The infiltration of opal templates is mostly done with liquid or vapor phase precursors. However, the host material can also be of solid phase during infiltration, which is addressed as nanoparticle infiltration. For the work presented within the scope of this thesis, only the infiltration via the vapor-based ALD and CVD is discussed. Here, the conformal deposition of the two precursors in very short sequences allows high filling fractions and prevents an early closing of the pores in a template. The use of highly pure precursors without additional organic solvents achieves extreme aspect ratios that other methods can not reach. The schematic real-space cubic unit cell of inverted opals is shown to the right → (top to bottom: tilted view, ΓL , ΓX ; drawn by J. Üpping)

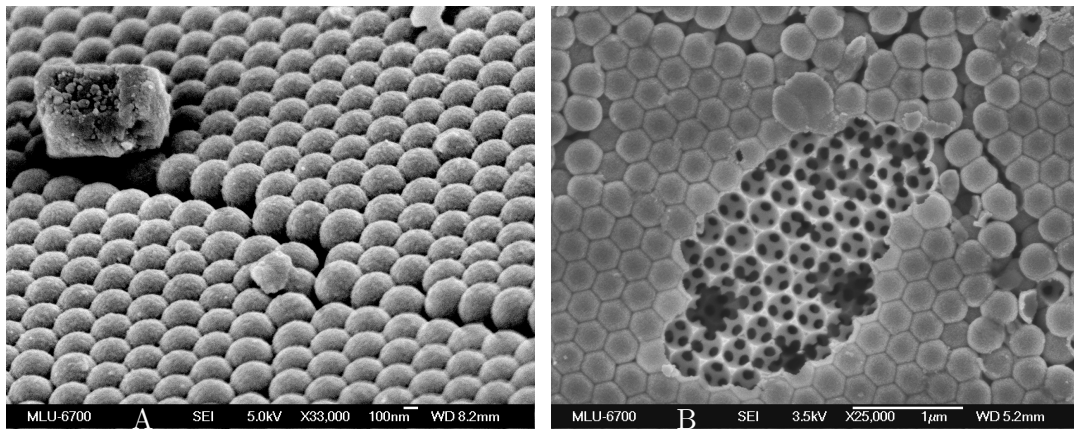
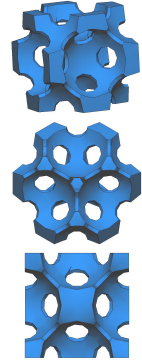


Figure 3.27: SEM surface graphs of inverted opal films: (A) surface still shows opal appearance, there is a line defect at a grain boundary; but the internals in opened zones (B) show the 3D inverted opal nature of the PhC.

In Fig. 3.27(A), the surface after deposition is recognized to be closed, looking like a slightly altered opal surface before deposition. The opened section (B) reveals the inverted nature of the sample and allows insight into the bulk of the PhC. The interconnecting tubes between the hollow spheres are shown at higher magnification in Fig.3.28(A). It is also noticeable, that the substrate surface has also been coated with ZnO, reforming the shape of bottom spheres. The ALD process successfully achieved high filling fractions and a full-depth infiltration of the opal template at sphere diameters of $d=300\text{nm}$. The Fig.3.28(B) shows a cleaved facet of a thick inverted opal film. L- and X-planes can be identified easily from the hexagonal and square symmetries. The angle of about 50° between these planes can be recognized. The tetrahedral (triangles) and octahedral (squares) voids of fcc lattice

⁶experiments performed in cooperation with Dr. B. Lange, Johannes Gutenberg Universität Mainz, AK Zentel

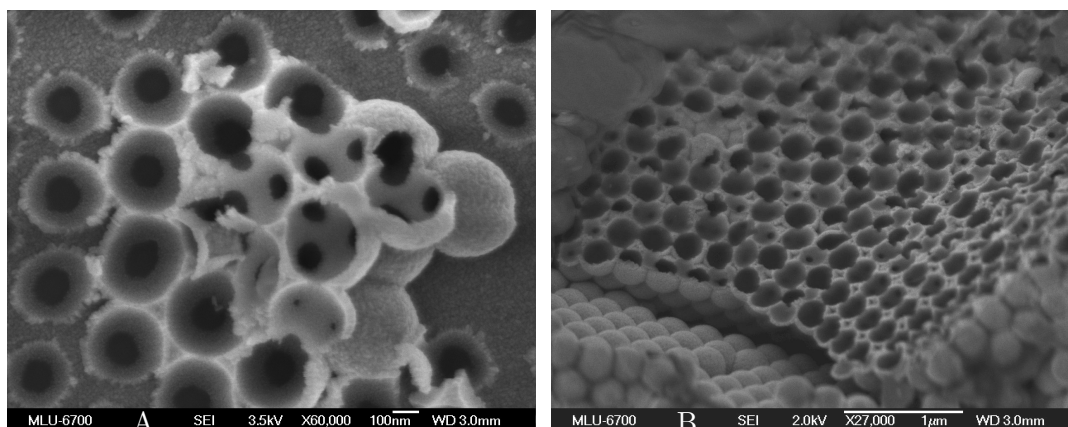


Figure 3.28: (A) Shell-spheres at higher magnification, the bottom layer imprint in ZnO can be seen, (B) a cleaved edge with L- and X-planes shows interstitial voids of the fcc crystal.

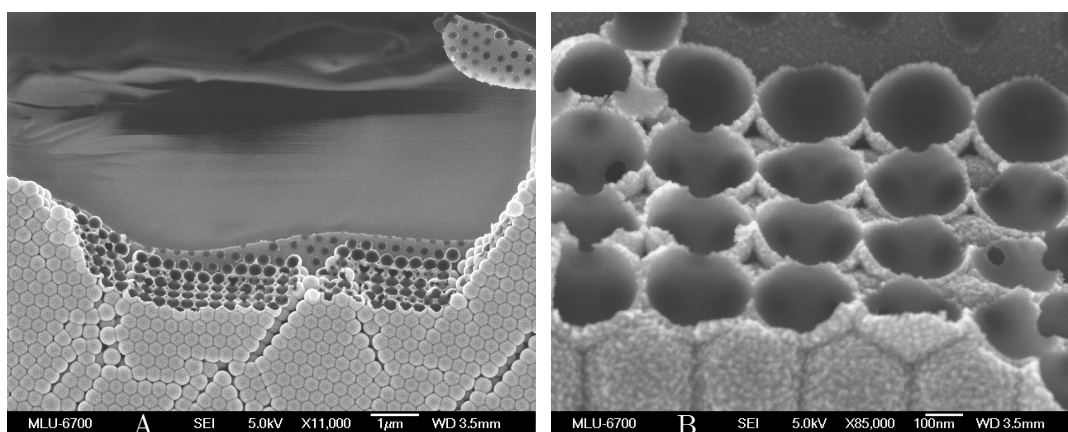


Figure 3.29: SEM graphs of ZnO inverted opal film: (A) thin-film sample of 4 layers, overview on cleaved sample edge; (B) high magnification of the $\langle 100 \rangle$ plane shows the octahedral voids and the touching tetrahedral ones in detail.

are clearly visible. The ALD infiltration succeeded to infiltrate into the full depth without visible gradient or inhomogeneity.

A thin-film inverted opal of 4 layers thickness is shown in Fig.3.29. At a cleaved edge it presents a clear view at the ΓX lattice planes. At higher magnification, the voids can be identified. The uppermost deposition is again remarkably thicker, than the in-depth shell thickness of the conformal deposition.

In Fig.3.30, the nano-scaled roughness of the ZnO coating presented at high magnification. Analysis of the shell thickness delivers values of (39 ± 3) nm for 'outer' spheres, while those embedded by neighbors are only about 20nm thick and thus within the predicted limits of inner conformal deposition. This fits the intended deposition of 200 cycles at 0.2nm per

3 Results

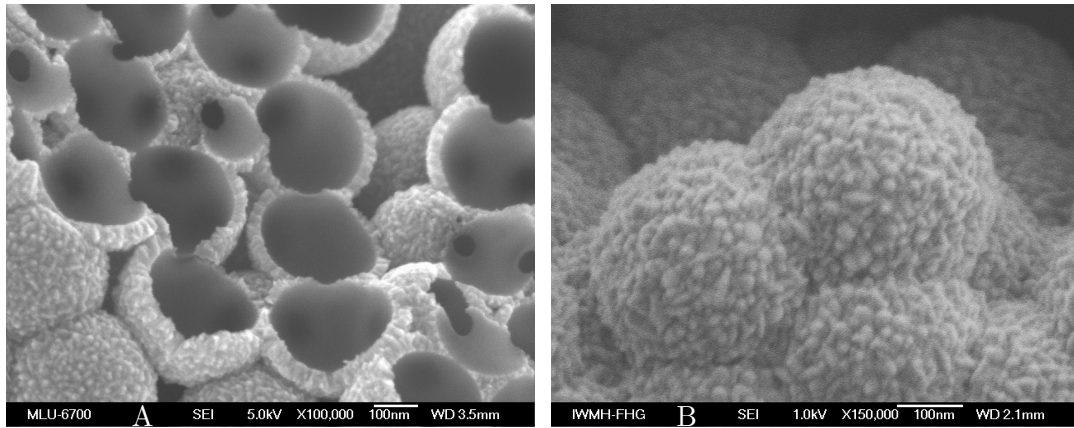


Figure 3.30: SEM graphs of ZnO shell spheres: (A) high magnification view on cleaved ZnO shells, the inner sidewalls of the shells are perfectly smooth. (B) High magnification of outer spheres with thick coating shells where the surface is very rough and covered with randomly oriented ZnO crystallites; ZnO crystallite's size is in order of magnitude of 4nm-15nm.

ALD cycle. In Fig.3.30(B), the granular surface of the ZnO shell is emphasized. The zinc oxide has grown multi-crystalline, a consequence of the spherical surfaces of the PMMA spheres. The insides of the shells are perfectly smooth, but during growth in ALD, a mono-crystalline spherical shell is not possible, leading to multiple orientations and thus rough surface on the nanoscale. The shells are evidently porous enough to allow the dilution of the PMMA cores with THF.

3.4 Optical characterization

Microscopy and near-field microscopy have been performed. The different states of the fabrication process are investigated spectroscopically in analogy to the simulated optical properties, so that numerical and experimental results can be compared.

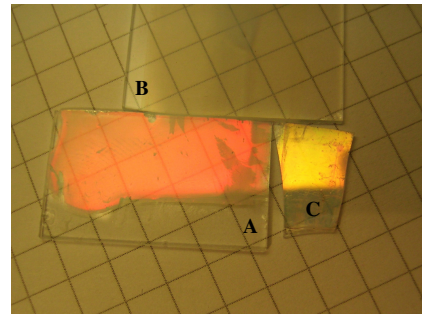
The main feature of the fabricated samples is their spectrally selective reflectance and transmission profile. In Fig.3.31, this is emphasized in a 42.5° beamsplitter configuration. An inverted ZnO opal is illuminated with white light from a 75W Xenon source from the right. The color-selective Bragg reflection in green is coupled out at about 85° while the transmitted part of the spectrum produces an orange beam straight through the sample. The bright white glare on the sample indicates scattering.



Figure 3.31: inverted opal beamsplitter on glass.

The investigation of the photonic thin-film is focused on the intended application in between the junctions of a tandem solar cell. Therefore, the required thickness of the IRL, thin-film properties and effective index approximations, the selective reflectance and its angular dependency, as well as the half-space transmission in an integrated setup are discussed in the following sections. Spectroscopy focusses on opal templates and inverted opal films, but has also been performed on composite samples. In Fig.3.32, a photograph of three samples at the three stages of processing the PhC film is shown. The samples are all made of $d=300\text{nm}$ PMMA spheres, *A* being the template in red. The upper sample *B* is the composite, the nearly vanished refractive index contrast leaves only a weak brownish color impression. Sample *C* is the inverted one, with a brilliant golden reflection.

Figure 3.32: Photograph of samples at the three fabrication stages (color) with:
 A) thin-film opal on microslide glass (PMMA, $d=300\text{nm}$),
 B) composite (PMMA,ZnO),
 C) inverted (ZnO).
 Samples B,C are processed from the same template series (A).



3.4.1 Reflectance of thin-film PHC samples

The reflectance of the opal template, composite and inverted samples have been measured. The according spectra are shown in Fig.3.33. Main focus of interest is of course the spectral position of the Bragg peak from the inverted opal thin-film, as well as its spectral width. These measurements are the experimental analogy to the spectral simulations performed with scattering matrix method, presented in section 3.1.2.

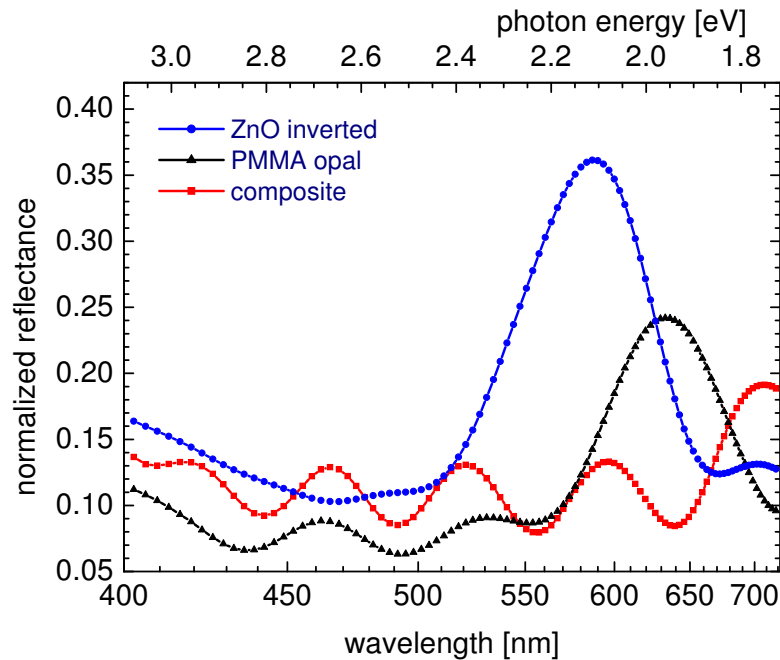


Figure 3.33: Reflectance spectra, measured at the three stages of sample processing. The opal stop gap at about $\lambda_{0,\text{opal}} = 630 \text{ nm}$ is red-shifted during infiltration. Depending on the filling fraction, a certain reflectance amplitude and position ($\lambda_{0,\text{comp}} = 714 \text{ nm}$) of the resulting composite is reached. After removal of the PMMA template, the inverted sample is measured: the obtained peak is placed at $\lambda_{0,\text{inv}} = 588 \text{ nm}$.

The obtained spectral data for the reflectance peak of the inverted sample in Fig.3.33 are of interest. The average maximum is 0.36, located at $\lambda_{0,\text{inv}} = 588 \text{ nm}$. The according base width (-1st min. to +1st min.) measures 177 nm, the FWHM measures 74 nm (understood as half the width between the maximum and averaged ± 1 st minima on either side). The spectra have been measured under the BX51 microscope with $\text{NA}=0.45$ at $M=20$, normalized against a reflection standard. The spectral range of the microscope is technically limited to 720 nm.

The measurements of the influence of PhC thickness are presented in the following section.

3.4.2 Reflectivity vs. crystal thickness

With a BX51 microscope (Olympus), reflectance spectra of local areas of constant film thickness are obtained, using constant NA and irradiance each time for comparison. Normalization of the reflectance is achieved with a standard sample calibration. This is present case a front surface aluminium mirror. Two thin-films (opal and inverted sample) of increasing thickness are placed on glass and placed under the microscope at magnification of twenty. In Fig.3.34 and Fig.3.35 the resulting spectra are shown.

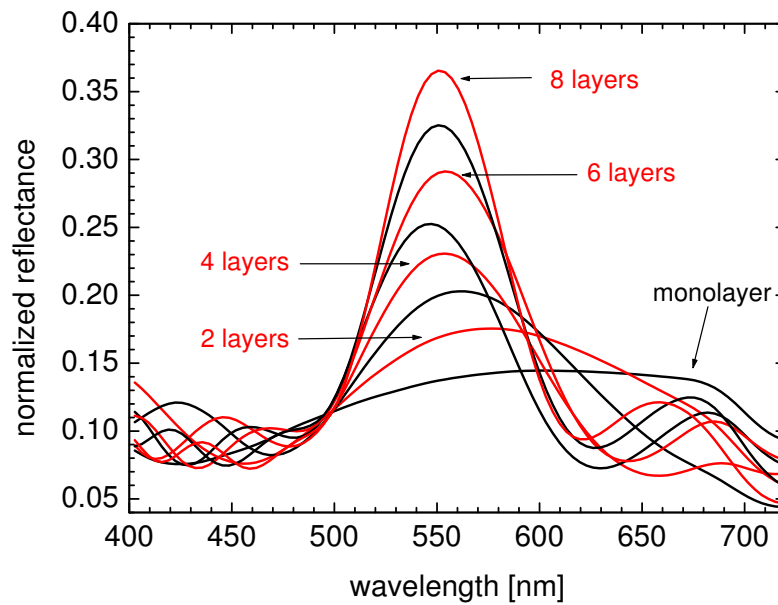


Figure 3.34: Reflectance of thin opal films ($d=254\text{nm}$) on glass substrate have been measured for 1..8 layers of thickness. Spectra measured under Olympus BX51 microscope with $\text{NA}=0.45$, $M=20$.

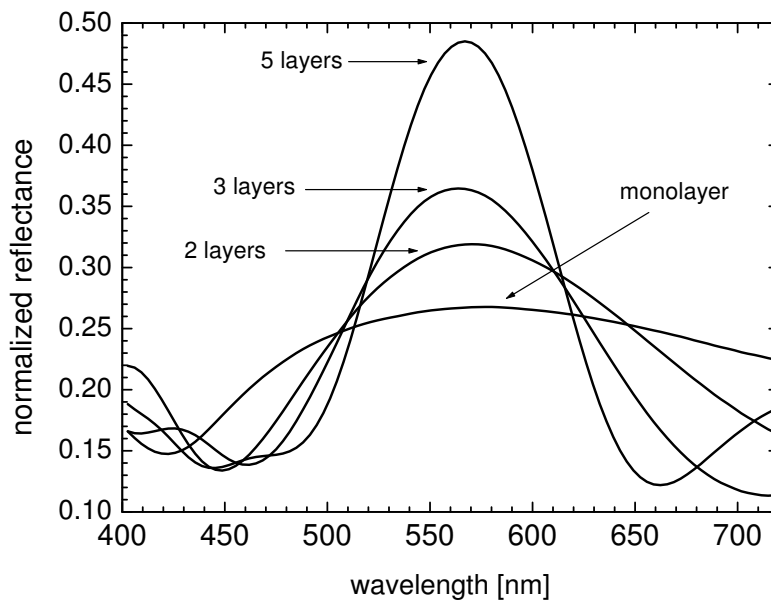


Figure 3.35: Reflectance of thin inverted opal films (OHS, ZnO, $d=300\text{nm}$, $t_{shell} = 40\text{nm}$) have been measured for 1,2,3 and 5 layers of thickness. Spectra measured under Olympus BX51 microscope with $\text{NA}=0.45$, $M=20$.

3 Results

By carefully scanning the sample's surface, the current number of layers can be monitored. In the regime of only few monolayers in thickness, a subsequent increase in reflectance amplitude is observed for every additional layer that contributes to the attenuation of the complete PhC. A saturation of this effect starts at about 13 layers [66], for a permittivity of $\epsilon \approx 2$. Inverted samples show a similar behavior, but with a more pronounced effect on reflectance due to the larger dielectric contrast as shown in Fig.3.35.

A good example of the clear visibility of the steps in height, the sequence of monolayers grown on one another, is shown in Fig.3.36. It shows a dark-field (reflectance) photograph of an opal sample using the 100x DF-objective of a Olympus BX51. Besides the layers, which clearly differ in color, also the transition zones of each layer can be seen. In the small zone along the rim of each layer, the fcc lattice has not grown. We can confirm these zones within the (2D) monolayers to be of square lattice type using SEM, see Fig.3.24(B) for reference.

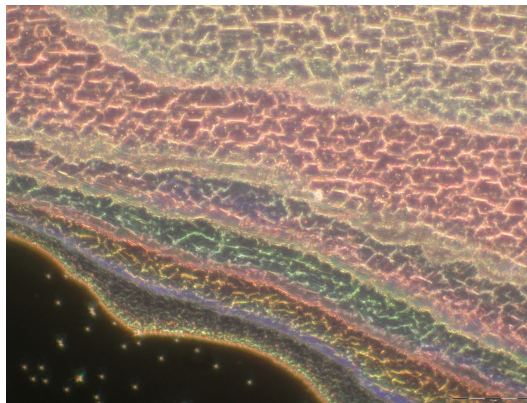


Figure 3.36: This DF image of an opal film on glass shows the ease of thickness determination with optical methods and the transition phase at the beginning of each layer.

3.4.3 Angular spectroscopy: Bragg reflection

The angular dependence of the reflection of incident light is caused by reflection of different modes at different planes of the crystal, that act as flat mirrors. The periodically reproduced distances between parallel planes produce a reoccurring phase difference between these modes that sum up to a sometimes brilliant reflection peak.

The Bragg condition links the wavelength of a Bragg-reflection λ_{111} from an $\langle 111 \rangle$ plane of the fcc crystal to the angle of incidence for incoming light, as introduced in chapter 2, Eq.(1.37). For an opal sample ($d=300\text{nm}$) on a glass substrate, the angular reflectance behaves like the spectra in Fig. 3.37.

The visible lattice constant d_{hkl} of an arbitrary plane of the opal is indexed with the Miller indices h, k, l of a plane and calculated from the lattice geometry, as done for the $\langle 111 \rangle$

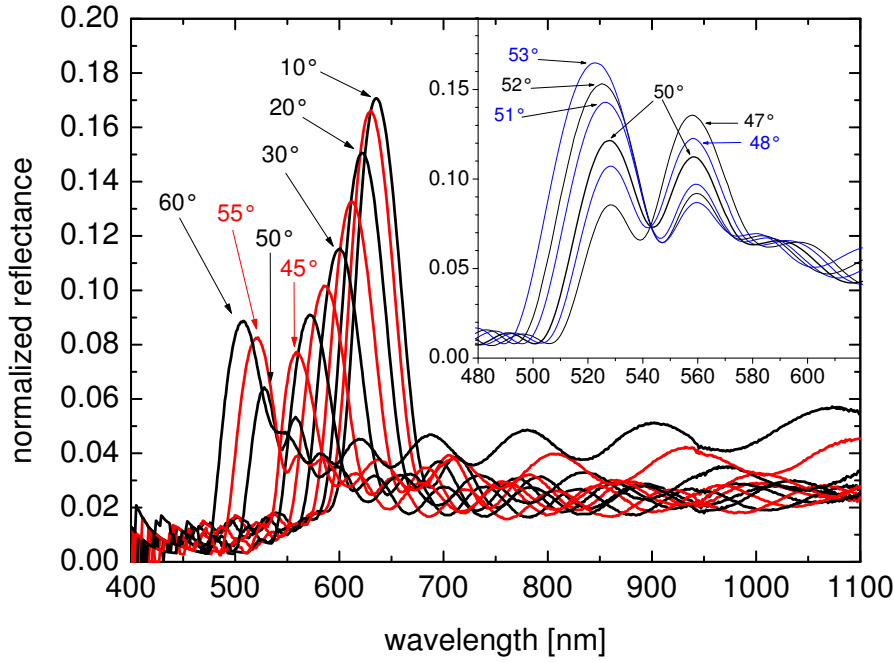


Figure 3.37: Angular reflectance measurement on an opal sample (PMMA/air): the blueshift is obvious (also for FP-oscillations), around $\Theta = 45^\circ$. The inset shows the anti-level crossing magnified around 50° .

plane in (3.15):

$$d_{111} = \sqrt{\frac{2}{3}} \cdot d \approx 0.816 d \quad (3.15)$$

Of course, any other plane of the crystal can produce Bragg diffraction. At higher angles, we can experimentally observe the interference on a $< 200 >$ plane of the fcc lattice as the inset in Fig. 3.38 shows at 50° .

For ALD infiltrated inverted ZnO samples (processed from the same colloidal suspension with $d=300$ nm), the measurement of angular reflectance resulted in the spectra shown in Fig.3.38. At first glance, three important differences are visible between the two Bragg analyses. First is the difference in reflectance. The inverted sample has a by factor of about two higher reflectance than the opal. Second, the spectral width (FWHM=96 nm) of the inverted opal (IO) is also larger, the base width between the 1st minima on either side measures 169 nm. The peak is centered at 596 nm. Third, the FPOs clearly differ in their number and distances: in the inverted sample, only two oscillations occur on the red side of the main peak, while the opal produces four to five. The presented spectra in figures 3.37 and 3.38 are from two different samples (opal/IO) of unequal thickness at the investigated spot. The measured opal film is about twice as thick as the inverted film. The IO sample is five layers thick, in average over the used illumination spot size, while the opal is in average eleven layers thick. Thickness has been determined from FPO, as stated in section 3.4.4 on thin-film properties, using equation (3.19). The effective index

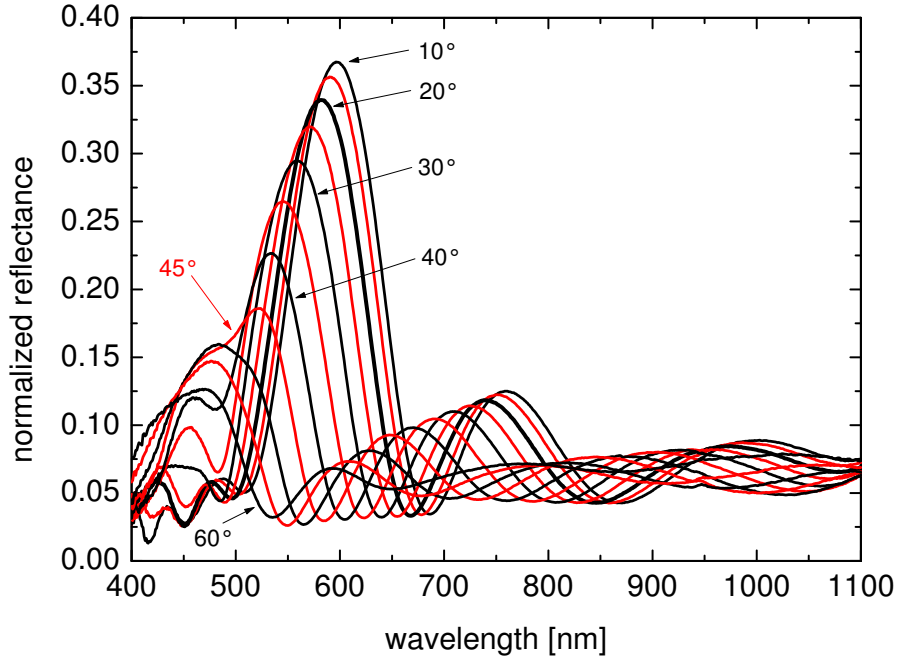


Figure 3.38: Angular reflectance measurement on an inverted opal sample (air/ZnO): around $\Theta = 45^\circ$, antil-level crossing occurs; the amplitudes are significantly higher than those of the opal reflectance, the FPO distances are wider than in the opal spectra.

of the inverted sample is also lower than in the opal template, as discussed with Fig. 3.42. This explains the smaller number of observed oscillations. However, the incident light still hits the interface between air and a massive ZnO layer first: the conformally coated surface. Here the index contrast between air and ZnO increases overall reflectance from about 4% to ca. 7%, according to (1.3). At the bottom of the PhC layer, there is not a massive layer of zinc oxide on the glass substrate, but a mixture with the air cores. So here an effective index for the PhC has to be applied. This adds another 2-3%, depending on the actual filling fractions at the bottom of the crystal. These two interfaces cause the increased baseline of reflectance, when compared to the results from the opal sample.

To verify, whether the blue-shift obeys Bragg's law from equation (1.37), the maxima of reflectance are identified for all measured angles and the peak positions are plotted squared against the squared sine of their individual angle. A linear regression as in (3.16) is now possible in the form of $y=A+Bx$, with $\sin^2 = x$, $4d^2 \cdot n_{fit}^2 = A$ and $4d^2 = B$.

$$\lambda_{111(peak)}^2 = 4d^2 n_{fit}^2 - 4d^2 \sin^2 \theta \quad (3.16)$$

The obtained parameters A and B give us access to the effective index n_{fit} and the sphere

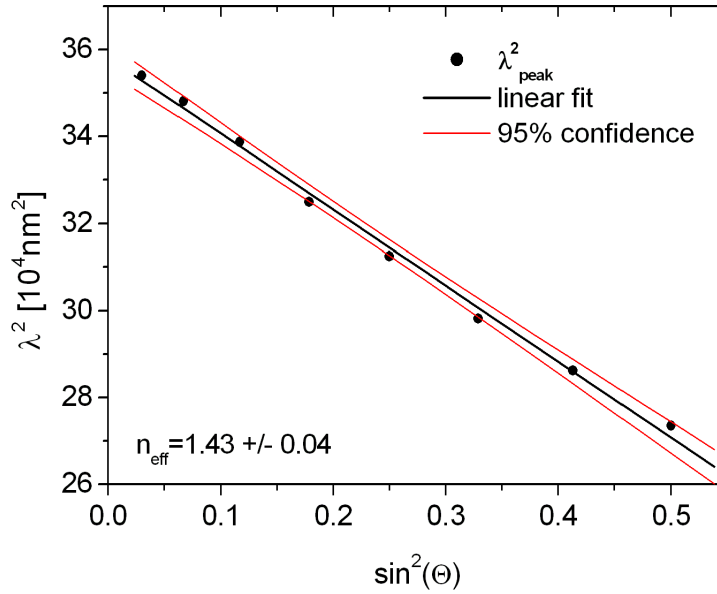


Figure 3.39: Bragg fit of the angular scan for a $d=300$ nm opal: Fit parameters lead to an effective index of about 1.43 and a mean diameter of 296 nm for the spheres.

diameter d , the sign of B is negative.

$$n_{fit} = \sqrt{\frac{A}{-B}} \quad (3.17)$$

$$d = \sqrt{\frac{3}{2}} \frac{1}{2} \sqrt{-B} \quad (3.18)$$

For the investigated ZnO sample, the Bragg fit is shown in Fig. 3.39. The obtained effective index is $n_{fit} = 1.43 \pm 0.04$. The average sphere diameter of $d = 296 \text{ nm} \pm 2 \text{ nm}$ is obtained from the position of the Bragg peaks with Eq. (3.16) and (3.18). The BS of an inverted opal of higher permittivity than the often used 2.0 for PMMA reveals (see Fig.3.3), that the standard Bragg fit does not work for higher angles. For the presented analysis of my samples, I used only values obtained from angles up to 45° . The index parameter n_{fit} is not the effective index of the PhC in terms of the approximations of n_{eff} introduced in chapter 1. Since we are spectrally not in the long wavelength limit but at the photonic stop gap, an effective index approach would be valid only, if we introduced anomalous dispersion and treated the imaginary part of the refractive index between the edges of the photonic stop gap[53]. The set of spectra obtained in angle resolved reflectance measurements can be compared to the simulation results from SMM. Using the 2D colormap, the comparison between experimental data and calculated data for the tilted angles of incidence becomes easier in Fig.3.40 For small angles of up to $5^\circ - 10^\circ$, reflectance is nearly invariant against tilt. Thus, measurements at such angles can be considered representative for normal incidence.

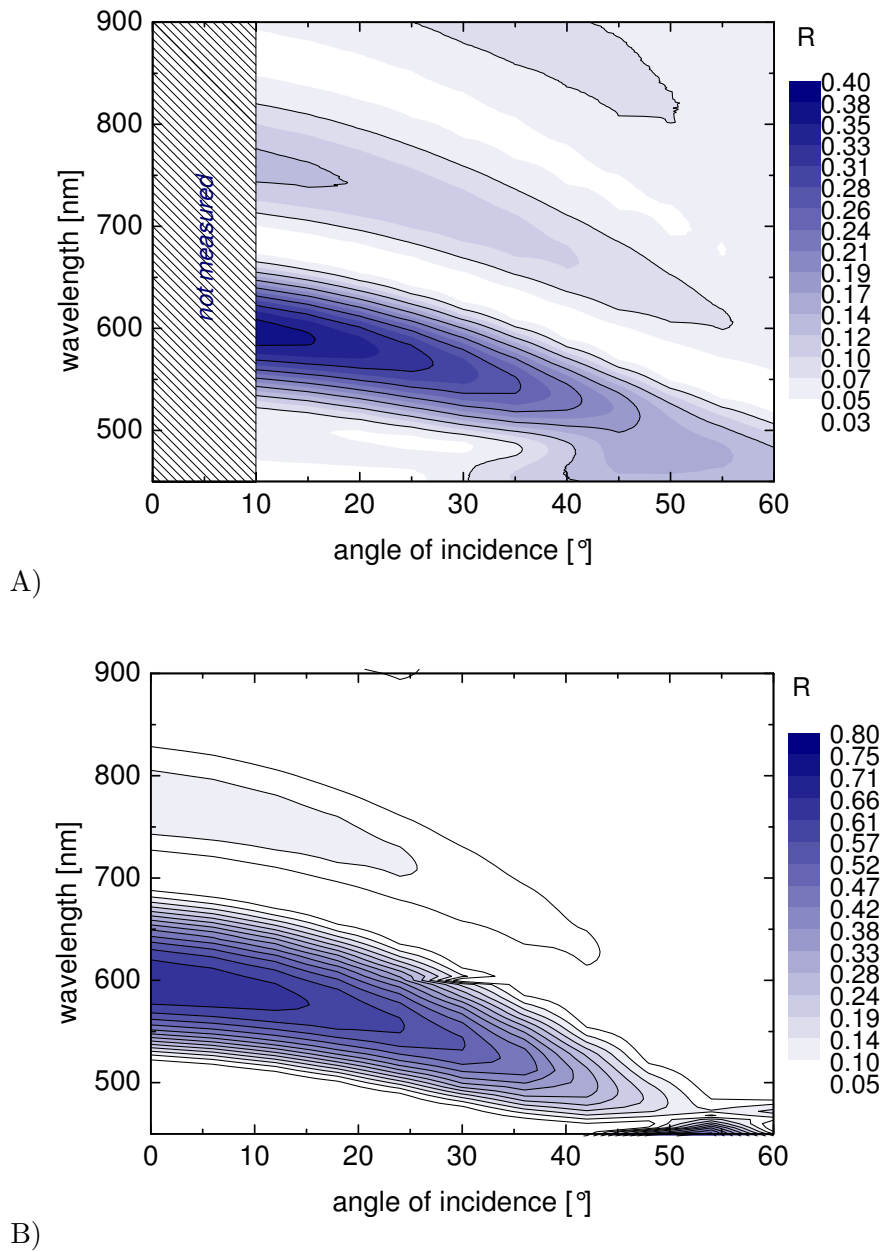


Figure 3.40: A) Measured angular spectra of ZnO IO (as in Fig. 3.38) but in a 2D map. The according SMM calculation (B) of the tilted angle of incidence (Θ) from Fig.3.12 is in very good agreement. Measurements with $\Theta < 10^\circ$ are not possible with the setup. A factor of 2 between measured and simulated amplitudes is observed.

3.4.4 Optical thin-film properties and effective index

Fabry-Pérot oscillations (FPO) appear on both sides of the Bragg peak in reflection spectra of thin opaline films, as Fig.3.41 shows. They also superimpose the main peak which may lead to a more asymmetric shape. Towards the long-wavelength limit, on the red side

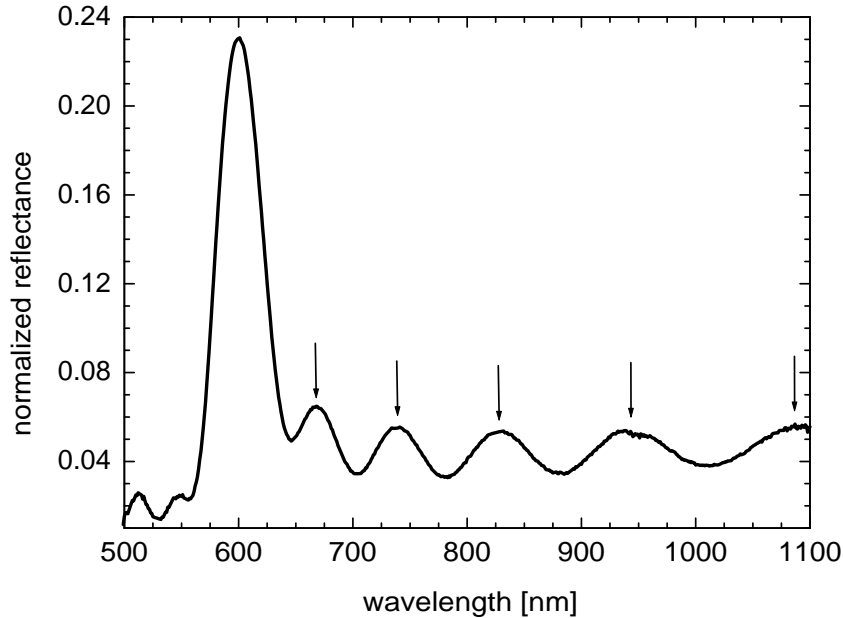


Figure 3.41: Reflectance of thin film opal, PMMA on glass, measured at $\theta = 30^\circ$ angle of incidence. The Fabry-Pérot oscillations are clearly pronounced along with the dominating Bragg peak at 600 nm wavelength.

of the Bragg peak, we move into the effective index regime. Here the photonic band structure provides smooth bands without stop gaps, because the larger wavelengths can no longer resolve the fine photonic structure. We can now treat the crystal film like a slab of homogenous refractive index n_{eff} . With sufficiently smooth films, a determination of film thickness d_F is possible here to a certain extent. Information about d_F is provided by the FPO, more precisely their spectral distance, which is constant in energy. Smoothness is necessary for the internal reflections to build up, roughness leads to scattering, scattering destroys the conditions for FPO formation. With basic thin-film optic considerations we can produce the thickness equation (3.19):

$$d_S = \left[2\sqrt{n^2 - \sin^2 \theta} \cdot \left(\frac{1}{\lambda_m} - \frac{1}{\lambda_{m+1}} \right) \right]^{-1} \quad (3.19)$$

With a known spectral distance of two neighboring FPO maxima and the angle of incidence θ , two variables are unknown: the films thickness d_F and the effective index n_{eff} .

We can determine either of them externally. The thickness can be obtained in SEM investigations or by repeated FPO analysis at different angles. The effective index can also be calculated using known filling fractions and refractive indices of the participating materials. Preparing a film of massive dielectric as a standard, this method can be calibrated to a certain sample process and the specific material's refractive index, which may vary between different preparations. The investigation of FPO in the reflection spectra of a sample of known thickness delivers experimental values for the effective indices. The effective indices discussed in the following sections have been obtained through thin-film analysis. In general, filling fractions have impact on the effective indices. For the discussed

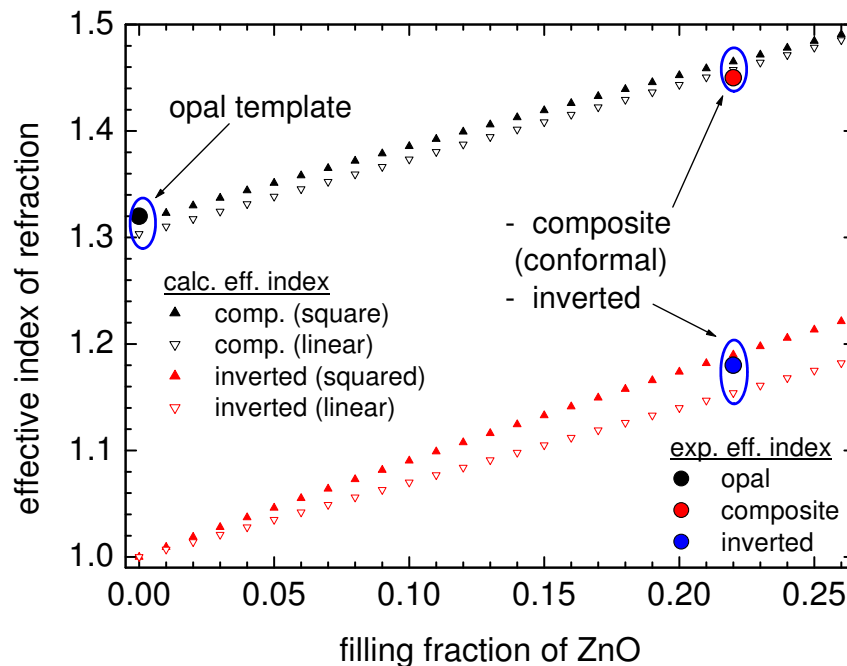


Figure 3.42: Calculated effective indices of refraction as a function of filling fractions of completely inverted and composite structures are shown. The points of the bare opal template and the maximum conformal infiltration are encircled. The inverted opal reveals a rather low effective index. Experimental values are marked (circles).

types of samples, the possible n_{eff} are shown in Fig. 3.42. They are based on Eq.(1.30) and Eq.(1.31) and make use of the linear and squared index approximations. Experimentally observed n_{eff} do not differ significantly from the OHS model. Actually, all observed effective indices are in the vicinity of the predictions. Strong differences would indicate altered refractive indices of the contained materials or incorrectly processed deposition. Measured and calculated values of the three sample types in comparison are also listed in Tab.4.5.

Sample type	core	shell	host	$n_{eff}(\text{exp.})$	$n_{eff}(\text{lin.})$	$n_{eff}(\text{sq.})$
opal	PMMA	air	air	1.32	1.315	1.303
composite	PMMA	ZnO	air	1.45	1.457	1.465
IO	air	ZnO	air	1.18	1.154	1.190

Tab.4.5: Effective indices of opal, composite and inverted PhC, from thin-film analysis and effective index approximations, following linear Eq.(1.30) and squared Eq.(1.31).

3.4.5 Impact of disorder in opal thin-films

A good optical film features constant thickness and homogenous and isotropic optical constants. In the case of opals, isotropy is conveniently broken by the lattice symmetry and homogeneity replaced by periodic modulation of the refractive index. A smooth colloidal film with constant thickness but undeveloped crystalline order will behave like an optical thin-film with an effective refractive index. The film will not develop photonic stop gaps or periodic diffraction patterns. Instead, a very high ratio of scattered intensity will occur dependent on the size distribution of the spheres and the wavelength of light. Thus, such samples will be opaque to the eye. Examples of transmission spectra of such films are shown in Fig.3.43(A).

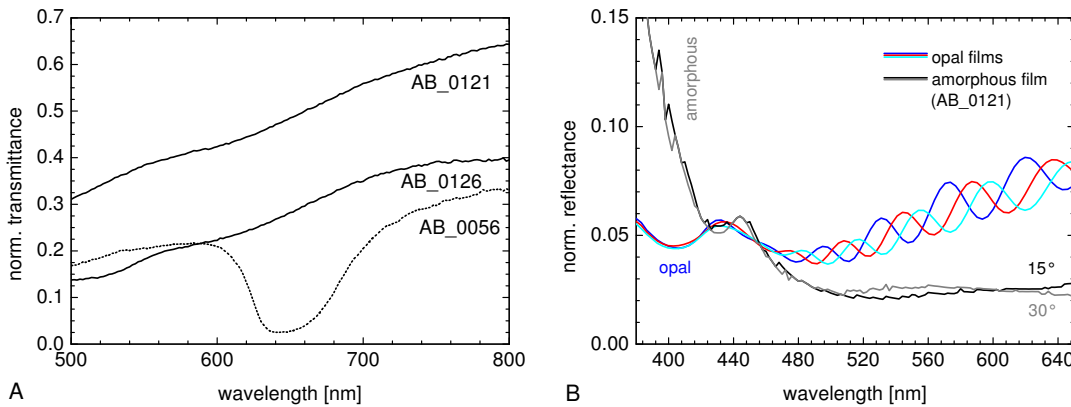


Figure 3.43: Specular transmittance spectra (A) through amorphous films reveal opaque character of the samples, only opalized films show the Bragg-dip in transmission (dot curve). In reflection (right), the films differ not only by the dominating Bragg peak, but also scattering strongly increases at shorter wavelengths in amorphous films. Films of good quality exhibit clear FPO, amorphous or incomplete films do not show specific angular dependency.

The samples differ in grade of disorder and thickness: sample AB0121 has been dip-coated at a velocity of 1090nm/s and is a sub-monolayer (like Fig.3.22 B), sample AB0126 processed at 300m/s. The optical stop gap of opal films will only show if crystallization was successful, which is represented by a spectrum of the opaline sample AB0056. In reflectance, thin-film oscillations (FPO) will be measured only, if a sample is homogeneous enough and does not destroy the coherence conditions with scattering. Fig.3.43(B) shows both cases for rapidly processed thin-films. The spectra of the amorphous sample (also

3 Results

No. AB0121, measured at 15° and 30° angle of incidence) do not differ significantly. The reflectance increases dramatically towards shorter wavelengths, which can be attributed to Rayleigh scattering. The crystalline films however, show clean thin-film oscillations. Main influence on disorder and the stop gap has the polydispersity of colloidal solutions [59]. Amorphous films can be considered as (diffusive) anti-reflection coatings for the glass substrate, their effective index depends on the degree of disorder and is found between the optimal 1.22 (for glass of $n=1.5$) and 1.32 of opals. Light of short wavelength however, can resolve the disorder in the small size range and is therefore exposed to scattering at single particles.

3.4.6 NSOM

Insight into the local influence of cracks on the transmission of opal thin films can be gained by near-field microscopy. The use of near-field scanning optical microscopy (NSOM or SNOM) gives access to the distribution of the optical fields at the location of the sensing tip. Sensing is done with an aluminum coated tapered fibre tip, featuring an aperture smaller than 100nm in collection mode, detected with a PMT. The sample is illuminated with a slightly focused laser beam through the glass substrate. Since the NSOM microscope is (besides the optical part) basically an atomic force microscope, the topology of a sample can also be recorded in force feedback mode. Then, a constant distance of about 20nm is kept by the automatic feedback control of the z-axis piezo-driver. In the case of larger distances than 20nm, the plane of detection is no longer conformal, but planar above the sample's surface. Illumination has been realized with wavelengths of 488nm and 658nm supplied by an Ar ion-laser. Two measurements showing roughly the same field of view on an opal sample are presented below in Fig. 3.44. Left pictures are topologies, on the right the according field intensities in 'contact' mode (distance of 20nm). A detailed analysis of the NSOM data from my opal samples and a theoretical description and prediction of the observed diffraction pattern has been published by Bittkau [92]. The chosen FOV on the measured sample features an upside-down Y-shaped groove and several linear and point defects, as well as the differences in height (number of layers) and extended defects of a more complex shape. It is clearly visible by comparison of the optical data to the topology graphs that the surface pattern and the diffraction pattern coincide in the local distribution of minima. The diffraction at major defects dominates the near-field distribution of the optical intensities. Directly above the grooves, the intensity is very low. Around the groove centers, a pattern of maxima is built up. The periodicity of this pattern does not match the photonic crystal lattice and is caused by diffracted light at the defects, comparable to the diffraction at an optical slit. The intensity is increased at the edges, pattern lines of second and higher order are weaker. Between the two measurements, no significant difference in the optical properties can be found.

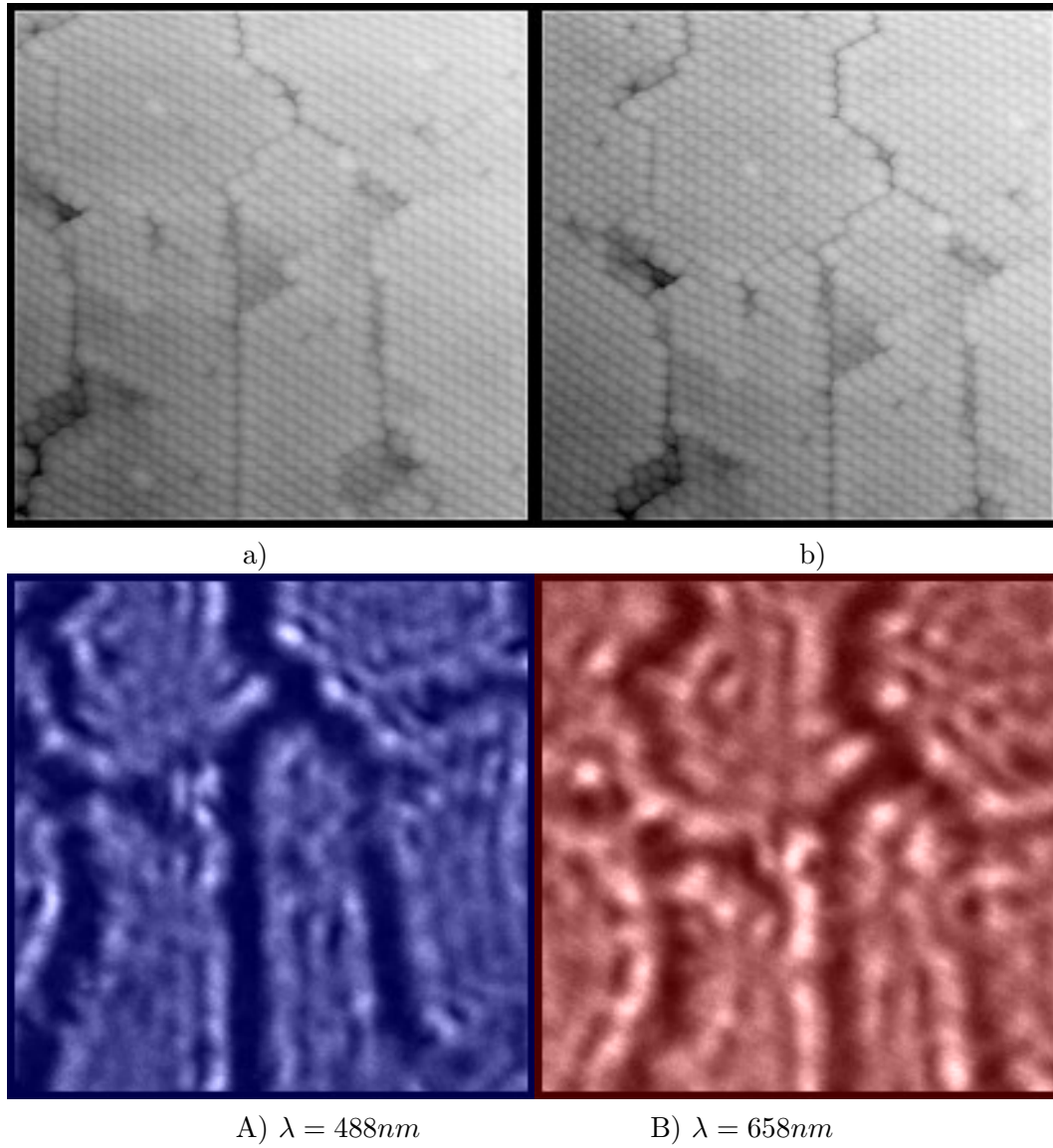


Figure 3.44: NSOM graphs of an opal thin-film: AFM topologies (a,b) of the field of view and related NSOM measurements in contact mode (A) and (B): the defects dominate the near-field pattern in transmission at both wavelengths.

3.5 Electrical characterization

Simple measurements for DC resistance have been carried out with Multi- and Sourcemeters. To characterize the frequency dependence of conductivity of the fabricated structures, electrical impedance spectroscopy (EIS) has been performed with a Zahner IM6 at the FMF Freiburg with M. Peters. The obtained spectra deliver the impedance of a sample over a wide range of frequencies, from GHz range to DC resistance. This reveals the electrical nature of the material.

To measure the lateral conductivity of a (thin) sample, the application of top contacts with known geometry on the surface is a typical method for measuring current at a given voltage. Thickness of the sample d , distance of the contacts a and the length of the contact line l are the geometrical parameters. Conductivity is defined via Ohm's law:

$$\sigma = \frac{1}{R} = \frac{a}{ld} \frac{I}{V} \quad (3.20)$$

For vertical conductivity measurements, a conductive substrate is needed at the bottom, as well as a top contact. Highly doped silicon wafers or TCO coated glasses (ITO) are convenient options. Also sputtered metal on a substrate, deposited prior to sample preparation, can serve as acceptable contact.

Alternatively, two top contacts can be fabricated to measure lateral conductivity. Special measurement tips can directly contact accessible surfaces on a sample, but the electrical connection is rather poor in most cases. The sample itself can take damage by mechanical stress from contact tips. A schematic negative of the interdigitated contact mask is printed right. The 'fingers' are 3 mm in length and 1 mm wide, four of them on each line, 3mm away from one another. The lines are also 1mm in width and are terminated with a larger contact plate for easier use of mechanical contacts. The whole mask is made of two lines and measures 27 mm in length and 10 mm in width.



Prior to the sophisticated EIS, technically simpler I(V) characteristics have been recorded. For repeated measurements of the resistance, a constant voltage was applied to the sample (compliant). The current was measured using a Keithley 2400 source meter that also supplied the compliant voltage. The results for the ALD inverted ZnO sample with interdigitated contacts as described above are shown in Fig. 3.45(B).

3.5.1 Electrochemical impedance spectroscopy

Besides the pure ohmic value of an electric resistance, its dependence on frequency is of interest. It does not only characterize the function of a device for AC circuits, but gives information on the character of a sample. The electrochemical impedance spectroscopy (EIS) measures the impedance over a wide range of frequencies. It also reads the phase of the circuit for the device under test. Together both pieces of information reveal a lot more about the nature of a material than a simple measurement of resistance does. The

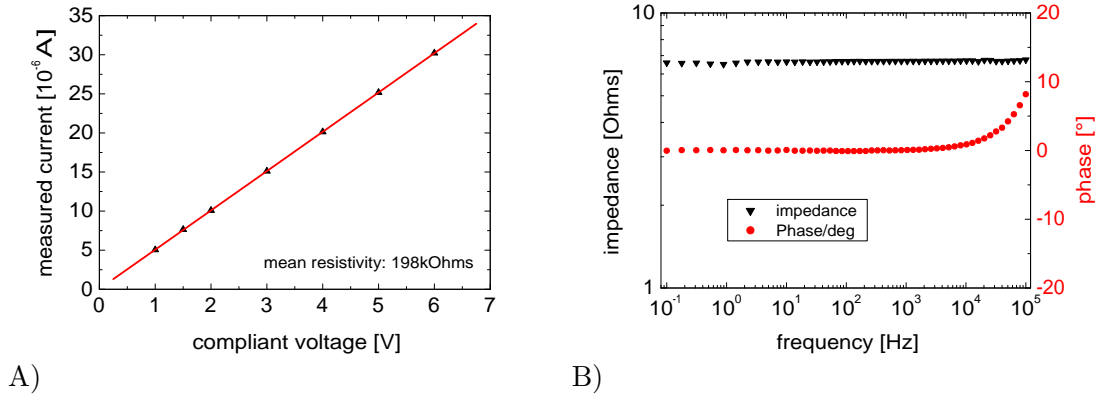


Figure 3.45: (A) I/V characteristic of sample AB206F (ZnO, $d=300\text{nm}$, $t_{\text{ZnO}}=40\text{nm}$) with interdigitated surface contacts shows: Current rises perfectly linear with increasing voltage; a purely ohmic behavior with negligible deviations. EIS test spectrum (B): one sputtered gold contact on ZnO inverted opal sample is measured. The resistance behaves purely ohmic, the phase is very stable, with a hint on inductivities at very high frequency; $R \approx 6.5\Omega$.

results of the EIS measurements on a CVD infiltrated ZnO sample (IO) are shown on Fig. For comparison, measurements on gold-sputtered glass slides have been conducted, with results comparable to those from sputtered gold contacts. The spectra are shown in Fig. 3.45. The orders of magnitude of the resistances measured differ extremely, although the conditions have been kept as equal as possible between the measurements. A gold sputtered standard microslide glass shows 63Ω , more or less independent of the frequency applied: a purely ohmic result for nearly all frequencies, see Fig.3.46.

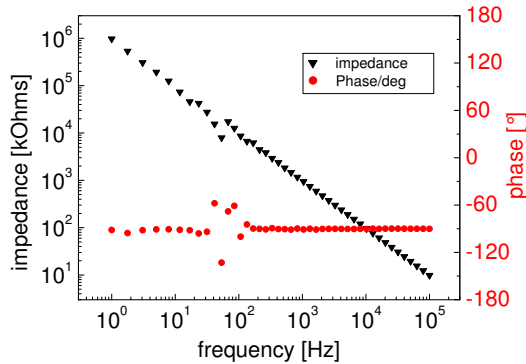


Figure 3.46: EIS spectrum of a ZnO inverted opal sample: capacitor-profile with rising resistance for decreasing frequency to DC voltages. The sample behaves purely dielectric.

An inverted opal sample of zinc oxide in contrast rises in resistance linearly with decreasing frequency, until we arrive at roughly $10^7\Omega$ in DC resistance. This behavior is characteristic of capacitors. The small noise in 3.46 is still caused by uncompensated power grid noise around 50Hz. For a massive ZnO layer, the resistance for DC voltage rises up to $10^9\Omega$. These results are shown briefly in Tab.4.6.

Sample type	$R_{\rightarrow DC}$	type
gold, thin film	63Ω	ohmic
ZnO, thin film	$10^7\Omega$	dielectr.
ZnO, inv. opal	$10^9\Omega$	dielectr.

Tab. 4.6: Orders of magnitude for resistance measurements from EIS spectra.

3 Results

For a second set of measurements soft contacts have been built from thin copper wires. These were bent and used like thin springs to enable a stable mechanical contact on possibly fragile samples and to reduce the probability of damaging the thin sputtered gold films on top. The copper wires have been mounted onto mechanical arms which can be finely positioned above the sample. This way, a very precise positioning of the point of contact is possible and short circuits or misaligned contacts have been avoided successfully. To further protect the samples from damage, they were fixated with rolled adhesive tape acting as a dampening spring at the backside of the sample. As an additional feature of this simple aid, the moment of contact of a copperwire with the sample's surface was clearly determined by a slight but very well observable movement of the flexibly held sample. For the following measurements, soft contacts have been prepared with copperwires. For ALD processed inverted opals, made of zinc oxide, EIS measurements show different results. This is shown in Fig. 3.47(A).

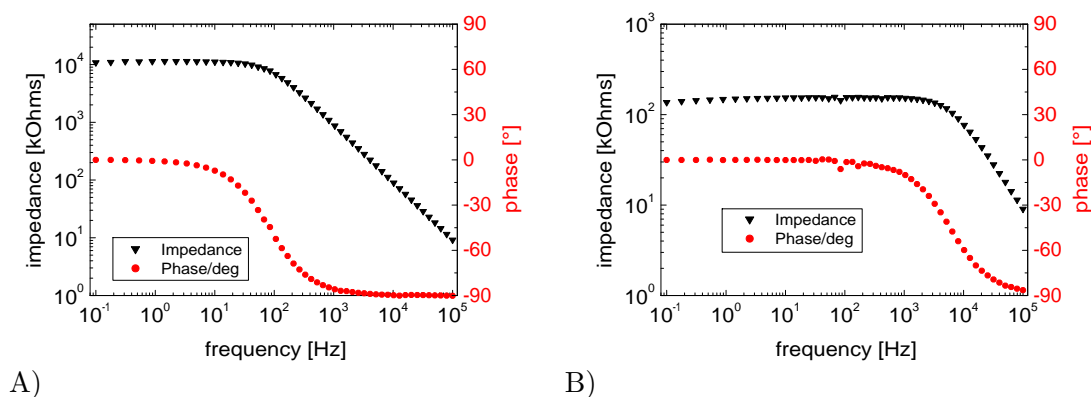


Figure 3.47: EIS spectrum of a ZnO inverted opal sample: (A) High impedance and capacitive character at higher frequencies, but saturated towards DC; (B) contact fingers pressed on (interdigitated) gold contacts. Measured impedance behaves ohmic below 1kHz in frequency. Resistance is about $10^5\Omega$.

The application of front gold contacts, sputtered with a mask of interdigitated fingers - directly onto the sample - achieves a far better electrical conductivity between the contact fingers. These fingers are pressed against the gold film, that conformally cover the periodic surface of the PhC. The poor mechanical contact faces are avoided this way. The resulting frequency spectrum is presented in the following Fig. 3.47(B). For comparison, a measurement on one of the gold-sputtered contacts of the sample has again been conducted to receive the answer of the electrical connections and the EIS setup. It is shown in Fig. 3.45(A). It becomes clear, that the contact with the sputtered gold films is purely ohmic. Resistance is about $6\Omega - 7\Omega$ for a distance of about 0.5cm between the contact fingers. The resulting resistance from this measurement is $198\text{ k}\Omega$ for the used geometry of contacts and at a room temperature of $21\text{ }^\circ\text{C}$.

Knowing the contact geometry, resistivity can be deducted. The contact line is 25 mm in length, and the sample of $2\text{ }\mu\text{m}$ thickness with the interdigitated contacts being 1 mm apart from each other. Assuming bulk conductivity over the complete thickness, this leads

to a specific resistance of about $100 \text{ k}\Omega\text{cm}$. The other extremum would be an assumed conductivity of the uppermost ZnO film on top of the structure. The outer ZnO coating is about 40nm thick, this leads to a resistivity of $200 \text{ }\Omega\text{cm}$.

The obtained resistivity is supposed to have values between $0.2 \text{ }\Omega\mu\text{m}$ and $10 \text{ }\Omega\mu\text{m}$.

Intermediate summary III : Experimental results

Structural analysis of the produced opals and inverted thin-film shows besides the lattice structure, conformal in-depth infiltration, and defects also a nanocrystalline growth of the ALD deposited zinc oxide. Further, in-depth filling of cracks down to the substrate with TCO is possible using CVD methods.

The results from **optical experiments** treat several aspects: the reflectance of the photonic IRL is tunable in amplitude (and width) by the number of deposited opal monolayers. Reflectance can easily reach values of more than $R=0.4$ (at 5 layers of ZnO inv. opal) at the peak position within the photonic stop gap. The angular dependency of the reflectance is well described and follows Bragg's law for relevant angles: a blue-shift with increasing angle of incidence is observed. The measured properties are in accordance with predictions from BS and SMM simulations. Classical thin-film investigations are suited for characterization of such films and provide access to effective indices, film thickness, or filling fractions. Disordered or inhomogeneous colloidal samples can be clearly distinguished from crystallized samples of homogeneous film quality. Using NSOM, the near-field transmittance of opals has been shown to depend strongly on defects, but not on the lattice structure of the PhC.

Electrical characterization of the fabricated samples shows ohmic behaviour (DC), but the determination of resistance with a defined contact geometry points to a rather high resistivity range, up to $10 \text{ }\Omega\mu\text{m}$.

3.6 Integration into thin-film solar cell

The designed IRL has so far been fabricated on glass and silicon waver substrates, also on standard a-Si:H films on glass (on the backside). The final step towards integration is the integration in a tandem device, the deposition on a top cell. Preliminary to this, a spectroscopical setup has been built to investigate the transmission properties of the fabricated IRL onto a silicon solar cell directly attached to the photonic crystal.

3.6.1 Transmission through the PhC to solar cell absorber

To approximate the conditions of transmission onto a half-space absorber, a special detection setup has been built. Instead of usual detectors a silicon PV-cell was arranged with collimating optics behind the exit slit of a monochromator. The monochromatic output was imaged on the solar cell with a lens, while an additional iris controlled the illuminated spot and reduced stray light that could deliver an unwanted offset on the solar cell output current. The schematic setup is shown embedded in Fig. 3.48.

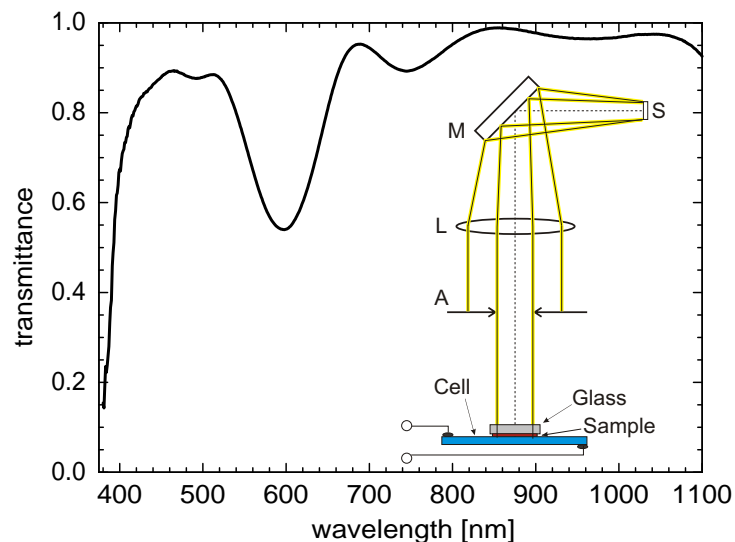


Figure 3.48: Transmission through an inverted ZnO sample ($d=300$) of 8 layers average thickness; sample is oriented upside down; spectral resolution $\Delta\lambda = 1\text{nm}$, Halogen illumination, grating blazed 500nm with 600l/mm. The setup scheme for small WD / wide area transmission measurements with collimated output is also shown; intensity is detected with a monocrystalline silicon solar cell. Samples are directly mounted on top of the uncovered cell. (S: monochromator exit slit, M: plane mirror, L: DCX lens (75mm efl), A: field stop.

The cell measures $25 \times 25 \text{mm}^2$ and the sample is placed on top of it but upside down, so

that the substrate glass becomes the front side towards illumination. This corresponds to a bottom cell with IRL and cover glass on top, but without the a-Si:H top cell. To normalize the results, a clean substrate glass has been measured on top of the detection cell. With this setup, an approximation of the transmittance into a half-space absorber (onto the solar cell) was obtained. The resulting transmittance spectrum is plotted in Fig. 3.48.

3.6.2 Integration on thin-film top-cell

The substrate for PhC deposition is a superstrate a-Si:H top cell with flat geometry, consisting of a front glass, planar transparent front contact and the a-Si:H absorber layer (p-i-n). The opal template is grown on the backside of the a-Si:H. PMMA nanospheres of $d=360\text{nm}$ are used, in order to place the Bragg reflection of the inverted sample in the red regime ($\lambda_{\text{Bragg,inv.}} \approx 700\text{nm}$), where experimental identification is expected to be easier due to the already low absorption in the top cell. It is then infiltrated with ZnO via ALD and inverted by a chemical dissolution cycle using heated THF in a mixture of liquid and vapor phase. The sample is processed with a second silicon layer on the PhC in order to produce the same refractive index interface as a bottom cell and it is finalized with a metallic back-contact⁷. The sandwich structure is drawn in Fig.3.49.

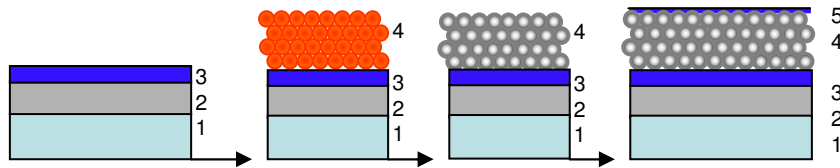


Figure 3.49: *Schematic structure of the integrated photonic IRL, in sequence of deposition: (1) front glass, (2) front contact (TCO), (3) a-Si:H cell (p-i-n), (4) photonic intermediate reflector: inverted structure from opal template, (5) silicon bottom layer and back metal contact.*

The fabricated device has been investigated with SEM along a cleaving edge to get an insight into the sandwich structure. The two SEM graphs in Fig.3.50 show the thickness relations between the top absorber (here at the bottom) and the PhC and the layer structure as far as possible by contrast. The device structure of the schematic in Fig.3.49 can be recognized. The ALD process has been extended with additional cycles of ZnO deposition in order to produce a massive ZnO layer on top of the PhC (towards the bottom of the cell, finally). This increases the mechanical stability for handling and transport of otherwise unprotected samples.

To find out whether the integration process is successful and to verify a proper function of the PV device, its quantum efficiency has been measured in the visible spectrum. The results of this measurement are shown in Fig. 3.51. The measurement of the EQE was

⁷processed by A. Lambertz at Forschungszentrum Jülich, IEF-5

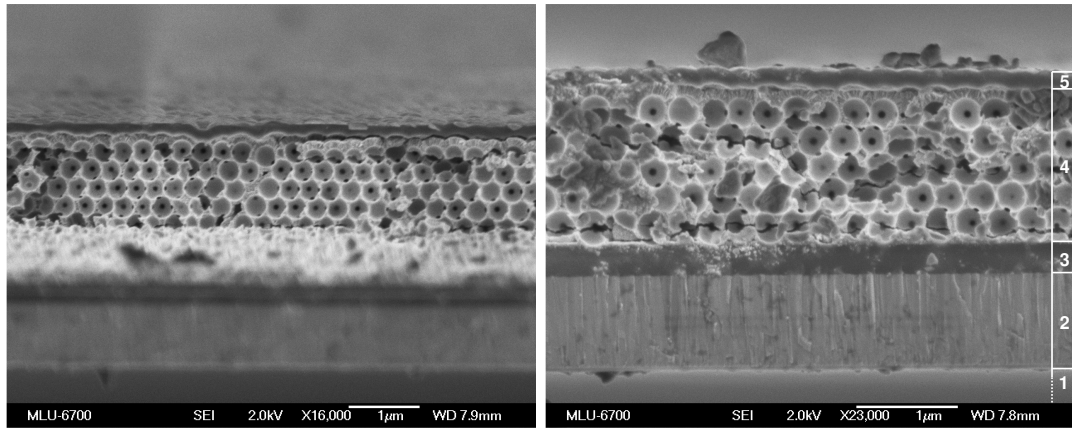


Figure 3.50: SEM graphs of the integrated photonic IRL prototype, view at cleaved edge: (B) uses enumeration of Fig.3.49. The inverted opal IRL is of 5 monolayers thickness ($1.3\mu\text{m}$). The massive ZnO deposition between the PhC (4) and the terminal silicon back layer (5) enhances mechanical stability.

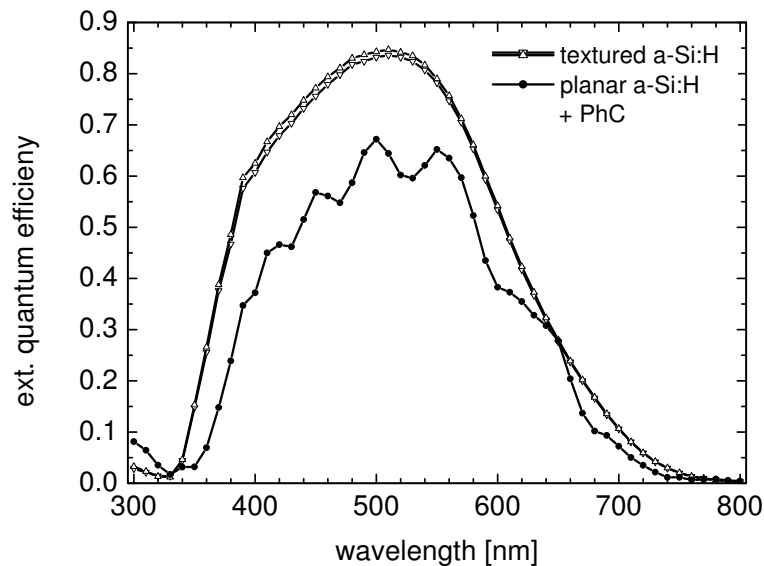


Figure 3.51: EQE measurement of the prototype; for comparison, two textured cells have been plotted. Thin-film FPO from the flat geometry are clearly pronounced. The IRL device stays 10%-20% below the currently best reference cells.

performed at reverse bias voltage. Bias influence saturates between 2V and 3V. In comparison to two highly efficient reference cells with randomly textured light-trapping front, the flat a-Si:H cell with the new 3D PhC IRL suffers from reduced quantum efficiency over nearly the complete absorption region. Thus, an impact of the IRL on enhancement of the efficiency above standard cells could not be confirmed in this first prototype.

Intermediate summary IV : Integration

The integration of the developed photonic IRL into thin-film solar cells is pursued in three experiments. Firstly, the **integrated transmission** of a reverse inverted opal sample onto a bottom absorber is investigated. The results show a high transmittance in the red / NIR spectral range: $\langle T \rangle \approx 0.95$ from 700 nm to 1100 nm.

Secondly, a **prototype** inverted opal IRL has been fabricated on the backside of a planar a-Si:H top cell and was processed to a contacted solar cell. This device has been characterized electrically: the measurement of an external quantum efficiency succeeded. Although the obtained EQE shows a reduced efficiency in comparison with state-of-the-art optimized standard cells, these results are the first experimental proof of an electrically conductive photonic crystal device that has been successfully produced in combination with a mass-production solar cell: Compatibility with the photovoltaic thin-film technology has been demonstrated!

4 Discussion

4.1 Comparison with other IRL concepts

In the introductory chapter, I have indentified the enhancement by the photonic IRL as an increase in current matching efficiency. This need not necessarily be the only valid classification. One can also distinguish between two separate absorption efficiencies or quantum efficiencies of the top cell and the bottom cell, as it is done in the calculations of enhancement and current matching in this thesis. Thus, the IRL could simply be described to enhance the absorption in the top cell at cost of absorption in the bottom cell.

The IRL rearranges the photon flux distribution between the two absorbers. The collective absorption of a given tandem cell is in principle not altered by an IRL. However, the electrical current that can be extracted from the cell is affected. Therefore, the utilized definition denoting an improved η_{cm} is reflecting the above relations very well. It further allows to clearly distinguish between the impact of the novel IRL and the individual absorption efficiencies of the absorbers in the tandem.

In contrast to other possible approaches, the proposed IRL has been designed as a separate layer between the absorbers. This is to some extent motivated by the already existing IRL, but was deliberately chosen to make compatibility with the existing processes of fabrication more probable. Because of the already poor electrical properties of a-Si:H the structuring of absorber layers is not favorable to avoid undesired increase of the recombination losses. Therefore, the creation of a separate interlayer made of transparent conductive oxide in between the two absorbers was chosen.

Criteria for a successful IRL concept are besides the physical requirements stated in the first chapter also the potential for mass production and the cost-effectiveness. After all, photovoltaic applications require large areas to be covered.

4.1.1 Numerical comparison of different intermediate reflectors

In section 3.1.4, the enhancement by the inverted opal IRL has been estimated according to the evaluation of rigorous numerical simulation of absorption in the top cell. In order to classify these results, two additional types of IRL are addressed here for comparison. A detailed analysis of the following issues has been published recently[93].

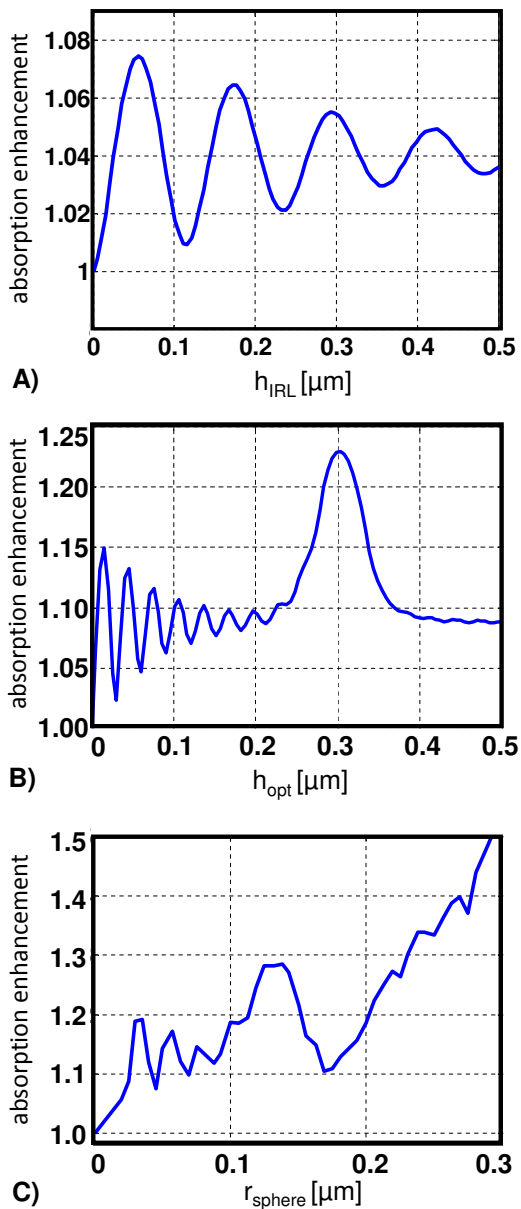


Figure 4.1: *top cell enhancement by homogeneous IRL (A), 1D PhC (B), and 3D inv. opal PhC (C) [93]; the IRL show increasing functionality of thin-films, dichroic filtering (Bragg reflection) and diffraction; they differ strongly in enhancement potential: (A) 7.5%, (B) 23%, (C) 28% (Bragg) / $\geq 50\%$ (diffr.).*

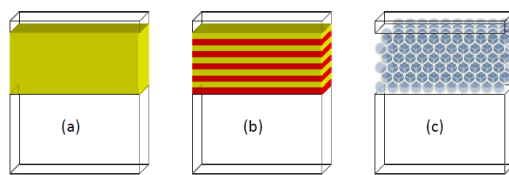


Figure 4.2: *schematic IRL types: (a) homogeneous, (b) 1D PhC, (c) 3D PhC.*

Fig.4.2 schematically shows the types of IRL numerically investigated. (a) Homogeneous IRL of thickness h_{IRL} represent state-of-the-art interlayers of spatially constant refractive index. (b) A one-dimensional PhC of ten layers of two refractive indices $n_1 = 1.7$, $n_2 = 2.0$ each and thicknesses ($h_1 + h_2 = h_{\text{opt}}$) represents dichroic filters that exhibit spectrally selective (specular) reflection. (c) An inverted opal thin-film of six layers with a variation of the sphere radius r_{sphere} , host index $n_{\text{inv}} = 2.5$ with air spheres.

Fresnel reflection and thin-film oscillations cause the enhancement of the homogeneous IRL. Several peaks subsequently occur in the graph in Fig.4.1(A). The maximum enhancement of 7.5% is observed at a thickness of about 60 nm, the incoherent reflection causes the background reflectivity of about 4%. The additional feature of one-dimensional periodicity of the Bragg-stack produces the enhancement in Fig.4.1(B). The enhancement is maximized to 23% at $h_{\text{opt}} = 0.3\mu\text{m}$. The impact of a photonic stop gap filtering clearly outweighs the enhancement potential of a simple homogeneous interlayer. The 1D PhC of 10 unit-cells is thicker than the IRL in (A), the average index is lower. This leads to increased incoherent reflectance of about 8% and a higher oscillation frequency, also of the enhancement.

The inverted opal approach adds a third feature to the IRL concept. Similar to the 1D PhC, the stop gap filtering here creates a maximum of about 30% of enhancement at $r_{\text{sphere}}=130\text{nm}$, as Fig.4.1(C) shows. But for large sphere radii, an even larger enhancement can be obtained when the 3D lattice planes diffract light at flat angles into the top cell, eventually coupling into guided modes. This is typically approached with one- or two-dimensional grating structures. The effect strongly increases the optical path inside the a-Si:H towards complete absorption of the diffracted photons. Further, the 3D structure allows for high porosities (e.g. $\psi=0.76$). Therefore the effective index is strongly reduced in comparison to massive material. Thus, incoherent reflectance and the amplitudes of interference-effects at the interfaces are higher than those in massive or 1D IRL.

The 3D PhC IRL offers the largest variety of effects and accessible parameters: stop gap filtering, back-diffraction and very low effective index of refraction. The possibility to incorporate very low refractive indices (air) allow high index contrast and thus, stronger amplitudes and increased enhancement. However, with the actual spectral region of interest of the micromorph solar cell, a fixed sphere diameter emphasizes either the specular (zero order) Bragg-reflection or the (higher order) diffractive properties. From 700 nm to 1100 nm of wavelength, any reflectance is causing loss of bottom cell irradiance. Therefore, either small structural sizes (bragg reflection between 500 nm - 700 nm) or sufficiently large structures (diffraction between 500 nm - 700 nm, but Bragg resonances only above 1100nm) are applicable for the PhC. Within the scope of this thesis, the Bragg-reflection approach is promoted. The developed experimental techniques and selected obtained results are explicitly applicable for the diffraction-based 3D PhC IRL approach as well.

4.1.2 Comparison with state-of-the-art IRL

As stated in the first chapter, state-of-the-art intermediate reflectors exist and already provide significant enhancements of the tandem efficiency. Thin ZnO films are easily produced, even with very precise thickness and sufficient conductivity (ZnO:Al, ZnO:B), for example via (VHF-)PECVD. They successfully excite thin-film oscillations and manage the photon distribution in the cell. A current difference shift of up to $3\text{mA}/\text{cm}^2$ has been reported, so has been a minimodule of 15% outstanding efficiency (initial). In terms of current matching or reflectivity, these IRL seem to provide a sufficient change to the photon distribution.

So far, it was shown that the Bragg reflectance of a 3D photonic IRL can compete with this in numerical simulations and contribute at least the same top cell improvement. The purely diffractive approach of large sphere radii offers here an even stronger enhancement, which could lead to much thinner absorber layers. Thinner cells are more cost effective - not only because of reduced demand for raw materials, but also because of less energy consumption due to quicker fabrication. The latter allows higher production capacities, because the fabrication time of a module is strongly affected by the deposition rates of absorber materials. This would be considered an important advantage for the industrial application.

One drawback of the homogeneous IRL approach lies in its operational mode. The thin-film oscillations it relies on are also excited in the long-wavelength regime and reduce transmission onto the bottom absorber without a contribution to top-cell performance

there. Homogeneous IRL do enhance the top-cell efficiency, but always at an increased cost of bottom cell illumination (back-reflection losses). This reduces the theoretical efficiency limits of the tandem. Here, the fabricated 3D PhC IRL has experimentally shown superior properties with its very high red and NIR transmittance. It can therefore be assumed that the optimized photonic crystal IRL can achieve higher efficiencies of the tandem cell than the optimized homogeneous IRL.

The 3D PhC IRL, however, offers some unique additional features which none of the so far proposed IRL concepts incorporate. These are (a) the drying crack conduction grid, (b) the smooth angular dependency and (c) the diffusive scattering properties caused by disorder.

(a) If a drying crack or other defect that extends from top to bottom of the (inv.) opal film is infiltrated with TCO, it can be used as an electrical interconnect between top and bottom of the PhC. This is another approach to increase conductivity, since drying cracks are formed in a rather dense network and easily possess thicknesses of one or more sphere diameters. They can be turned into an electrical contact grid to increase the effective electrical cross section of an IRL. The CVD crack filling with ZnO on thick opal films has been investigated in section 3.3.2. It can be seen from Fig.3.26(B,C) that the massive ZnO layer has been conformally deposited on the opal crystallites on both sides and reaches down into the crack and also covers the substrate. The formation of a TCO grid for the connection of top and bottom solar cell is therefore possible. Such feature is not available in homogeneous optical films.

(b) As the angular dependence of the photonic stop gap in section 3.1.1 and the measurements shown in section 3.4.3 show, the angle of incidence is well understood. In the high indexed silicon environment of the tandem cell and with respect to the red working regime proposed in section 3.1.5, the blue-shift of the Bragg peak is on the one hand not very strong, on the other hand it is no issue for the proper function of the IRL. Thus, the proposed device can be considered only weakly angle-dependent, with no expected drawbacks on the operation.

(c) Diffusing of light at the IRL and the resulting enlargement of the optical paths in a solar cell is an important and promising issue in many aspects. Thus, it is discussed in more detail in section 4.3.

The fabrication of the 3D photonic IRL, however, is obviously more complicated than the deposition of a homogeneous IRL. Further research and the improvement of techniques for opal thin-film crystallization is in demand now, especially upscaling. Only a few promising lab-scale methods exist world-wide, and with the prospect of applications such as in photovoltaics becoming obvious, it is more likely that an up-scaling and development into an artificial opal thin-film technology will be engineered in the near future.

4.2 IRL properties & fabrication methods

4.2.1 Properties in numerical analysis: coating thickness

The process of inversion is described by BS and SMM methods by solving multiple models of increasing shell thickness. Along the plotted curves or the map, we follow the temporal proceeding of a conformal deposition. The treated structures are therefore (OHS) composite PhC (thin-films, in case of SMM).

The course of the spectral position obtained from BS calculation in Fig.3.9 is expected, while the strong decrease in the spectral width is at first glance surprising. The cause for the vanishing of the stop gap however is, that index matching occurs at one certain point of infiltration. The index matching takes place when the effective index (a function of the filling fraction) of the ZnO shells meets the effective index of the PMMA opal cores. The index contrast approaches unity and the photonic stop gap can not develop.

This is of course not observed in the gapmap for inverted opals in Fig.3.8 since the effective index of air spheres is always lower than that of the ZnO shells.

In SMM simulation however, a displacement occurs in the spectral position during the transition from opal to inverted, which is not expected from the photonic BS of the composite. The peak position would be expected to close in on its final spectral position asymptotically (from above BS considerations), but instead it performs a rather sudden displacement during an early stage of the infiltration, shown in Fig.3.13. Cause for this behavior is the influence of an aspect that is not part of BS calculations: the finite thickness of the implemented virtual sample.¹

The explanation is, that the minima of the thin-film oscillations (FPO), which are red-shifted with increasing shell thickness, simply cut through the path of the stop gap that is predicted in BS calculations, forcing destructive interference and reducing reflectance amplitudes down to almost zero. This is independent of the index matching within the PhC. The effective index of the composite samples at reasonable ZnO shellthickness ($\leq 23 \text{ nm}$ at $d=300 \text{ nm}$) is still below that of even a glass substrate, assumed $n=1.5$ (see Fig.3.42). Contributions from a possible index matching of the PhC thin-film with the substrate are therefore not possible.

The discovered effect is not of importance for the final IRL application and has not been investigated in more detail. However, the optical properties of composite samples contain information about the refractive indices and filling fractions and make these accessible during the inversion process and not only after the finalization of a sample, thus allowing to optically monitor and control the growth process.

4.2.2 Spectral positions in simulations and experiment

For a comparison of band structure calculations (via MPB), the optical simulations (SMM) and the spectroscopical data on reflection obtained from the three stages of sample preparation in terms of the spectral position of the reflectance peak, three spectra are summarized in one graph, each: opal, composite and inverted opal. The amplitudes of the measured

¹in correspondence with M. Peters, FMF, University of Freiburg

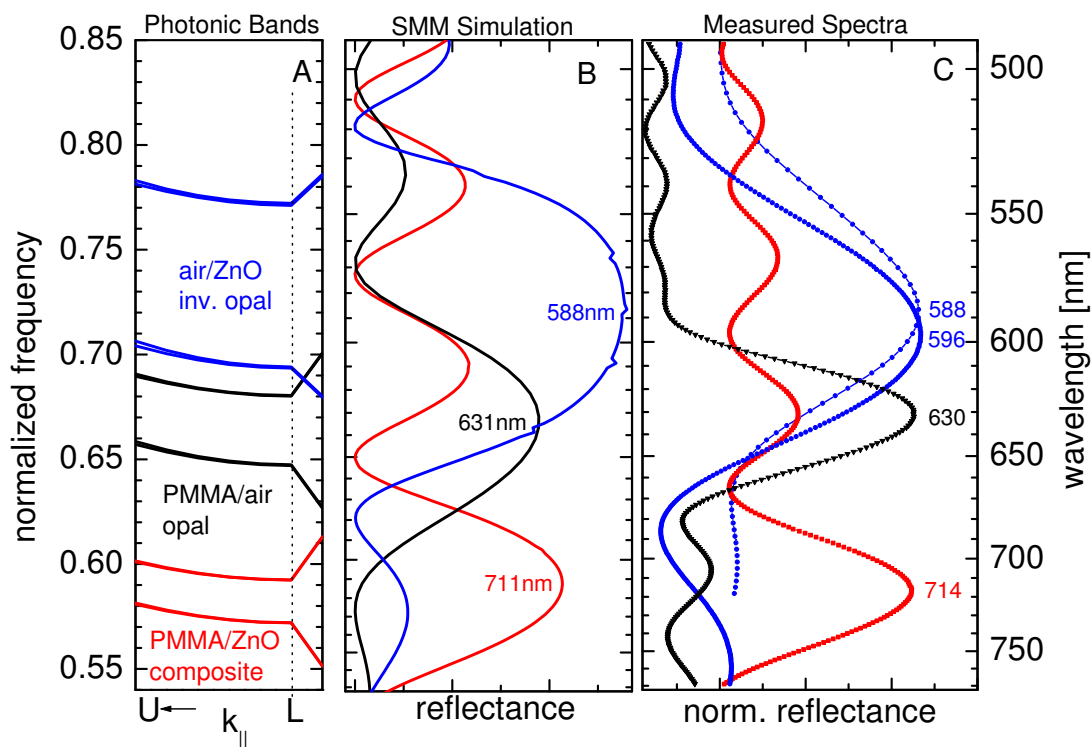


Figure 4.3: Calculated photonic bands, simulated SMM reflectance spectra and measured reflectance in comparison of the spectral positions. Inverted opal (6 layer film) made of ZnO ($n=1.7$) on glass substrate ($n=1.5$). Reflectance data are normalized to equal peak maxima. The photonic BS provides sufficient orientation in the spectral positions, but only finite SMM results are very close to the experimentally obtained data. The inverted sample shows in specular measurements ($NA=0.01$) a slightly higher peak wavelength of 596 nm than the 588 nm of the prediction. The measurement using a microscope objective ($NA=0.45$) delivers precisely the wavelength of 588 nm.

reflectances have been normalized to the maximum value of the inverted opal Bragg peak. This allows for an easy comparison of relative background reflectance and Bragg peak contribution.

The photonic stop gap of the opal template fits very well to the predictions from the (coherent) scattering matrix method and the measured reflectance. It is red-shifted in the composite structure after infiltration of high index material (ZnO, $n^2 = 2.89$). The difference between experimental reflectance of white light and the perfectly coherent simulation, where each thin-film oscillation reaches zero, becomes obvious. The relative contribution of incoherent reflectance of the composite is significantly higher than from the other samples, also the FPO amplitudes are generally much smaller than predicted. After template removal, the inverted opal stop gap is blue-shifted again and increases its width due to the increased index contrast.

The SMM Bragg peak positions differ from BS stop gap positions. They show a weaker pronounced blue-shift of the inverted and weaker red-shift of the composite, an effect of the finite thickness of the sample model (6 layers) - compared to the infinite crystal from BS calculations. The measurement, however, shows additionally a mismatch: the reflectance peak is located at 596nm (specular), while 588nm is predicted from SMM. From measurements at higher numerical aperture however, a wavelength of 588 nm is obtained: with the inverted opal of high index contrast, the NA effects turn out to be stronger than with the opal samples of lower index contrast.

4.2.3 Imperfections of the inverted opal IRL

All fabricated samples possess a certain amount of disorder and imperfection, as for example the SNOM measurements show very well. Only a bidirectional scattering distribution function developed from experimental measurements would represent the complete characteristics. Yet, the measured optical properties so far match the predicted ones sufficiently well. However, in contrast to communication technology for example, the disorder within an artificial (inverted) opal is not necessarily a problem for photovoltaic applications. On the contrary: it is even helpful here! Scattering or diffusing of light will contribute to light trapping, since the developed photonic filter is placed between the two silicon absorbers. A multi-crystalline photonic crystal for example will smooth out the already negligible polarization effects with its randomized PhC-crystallite rotation around Γ -axis. Furthermore, the typical cracks at grain boundaries of these crystallites can be an advantage in inverted opals, as already discussed in 4.1.2. The fabrication of opal thin-films is based on self-organization processes, and with the drawback of imperfect crystalline quality not being an issue here, the proposed device appears suited to become a mass product for large-area applications such as photovoltaic ones.

4.2.4 Electrical resistivity

Measurements of the electrical resistance in defined geometries have led to a reasonable estimation of the resistivity. However, the exact resistivity and conduction mechanism has not been determined. Zinc oxide is well known for surface conduction processes and its electrical properties are also very sensitive to adsorption of gas molecules on aforesaid surfaces[94, 95]. Thus, the issue of conductivity is very complex, especially since the effective surfaces of the fabricated nanocrystalline ZnO coatings are much larger than those in planar geometries. It is an important problem of the proposed photonic IRL, as also the prototyping has shown. The two ideal cases of bulk vs. surface film conduction that are assumed in section 3.5 provide good boundaries for the possible range of the resistivity. The fabrication of the inverted opal was performed using intrinsic ZnO from a low temperature ALD process. Two promising approaches to improved conductivity are higher temperature and doping. A limiting factor for the process temperature is the a-Si:H cell. Temperatures above 200°C are terminal for the hydrogen within the solar cell. Unfortunately, all processes of depositing TCO in order to achieve high conductivities involve temperatures of 350°C to 500°C or above, so this option is not available in the current

application. During the bottom to top fabrication of a tandem cell (e.g. on steel foil), the $\mu\text{c-Si}$ cell would be the substrate for the IRL. It can stand higher temperatures than the a-Si:H top cell. For this type of cell, a tempering step could be included in the process cycle to provide higher conductivities, even of the intrinsic ZnO. The second approach of doping can be performed using a multi-precursor process in ALD (or CVD). Instead of the two-precursor-cycle described in section 2.3.3, an additional precursor (pair) as for example trimethylaluminum (TMA) and water can be added in controlled amounts to incorporate aluminum directly in the growing inverted opal skeleton to achieve doping. A more elegant version of the same approach would be a pre-mixed precursor solution that already includes the dopant in correct volume fraction. It depends on compatible vapor pressures and solubility of the precursor materials. These approaches appear to be very promising and are applicable also in large scale CVD processing.

4.2.5 Materials and processes: technology transfer

The processes involved in the fabrication make use of available technologies and materials. Upscaling of the opal coating process is not considered a problem from the fabrication experience so far. The self-organized growth of artificial opals makes them in general well-suited for large scale applications. The used PMMA nano beads are easily resolved chemically, alternatively polystyrene (PS) nano beads can be used. These can be produced with higher chemical and thermal stability, offering advantages for ALD infiltration. But this would also increase the effort necessary to destroy them. Although wet chemical infiltration methods have certain advantages in application (e.g. room temperature), the use of vapor-based methods clearly has to be preferred. The infiltration by CVD or ALD leads to very good filling fractions, as the spectroscopic measurements and SEM investigations have proven. The deposition processes have not been driven for high deposition rates so far, but have been carried out rather slowly due to the very low temperature. For infiltration, zinc oxide has become the material of choice. It can be deposited very well with the used methods and the refractive index contrast is sufficiently high to generate the required photonic properties. Further, it is a rather cost effective resource. This gives an advantage over the optically more tempting but also more expensive indium tin oxide. The so far unsatisfying conductivity of the as-deposited ZnO can be addressed via doping.

4.3 Compatibility with textured substrates: roughness

Since the randomly rough surface of HCl etched ZnO on the front glass is currently the best available light trapping structure for the tandem cell, the possibility to grow an opaline IRL directly on this conformal roughness would allow a direct introduction of the novel interlayer in the fabrication process of the micromorph tandem cell. It is mandatory to emphasize, that the texture is a key component for an efficient micromorph tandem. In contrast to this demand, rough substrates are typically avoided for self-organized growth of photonic crystals. Flat or periodically patterned substrates are common. In case of opals, roughness of the substrate usually leads to amorphous colloidal films with a highly disordered arrangement of the spheres. Crystal long-range order is impossible for thin-films in contact with such a surface. Local crystallization however, may be possible depending on the actual size parameters of roughness. Growth experiments with PMMA opal films on the backside of randomly rough HCl etched ZnO of (superstrate) a-Si:H top-cells show, that the self-organization process of opals is capable of healing out the distortion caused by the actual substrate roughness. After few layers of randomly distributed spheres, the opal crystalline phase prevails and the distortion caused by the substrate is compensated. This is shown in Fig.4.4.

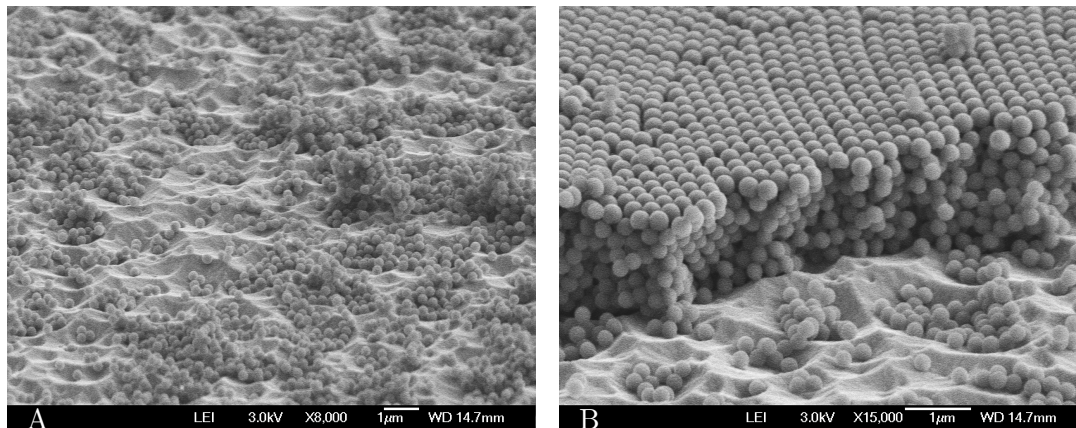


Figure 4.4: SEM photographs of opals grown on a textured a-Si:H backside: the disorder of bottom layers close to the substrate is obvious (A), but a crystal lattice develops after few layers already (B).

Interestingly, the typical drying cracks turn out much weaker in width, than in samples of high crystalline quality. The amorphous colloidal part close to the substrate does not contribute to formation of a photonic stop gap. Such opals show for example lower reflectance than their flat-grown counterparts. Nevertheless, a stop gap is pronounced, if the opal can establish enough lattice planes with sufficient crystalline order, as discussed in section 3.4.2. In Fig. 4.5 the impact on transmittance can be seen. The typical stop gap of templates (here again with $d=300$ nm) is weakened, but clearly visible. Additionally, the diffusing texture destroys the conditions needed for the formation of thin-film oscillations. No FPO's are observed here, which is helpful for illumination of the bottom cell. The relative impact of the opal template film is a 30% drop in relative transmittance through the a-Si:H substrate. The texture changes the angular distribution of light incident on the

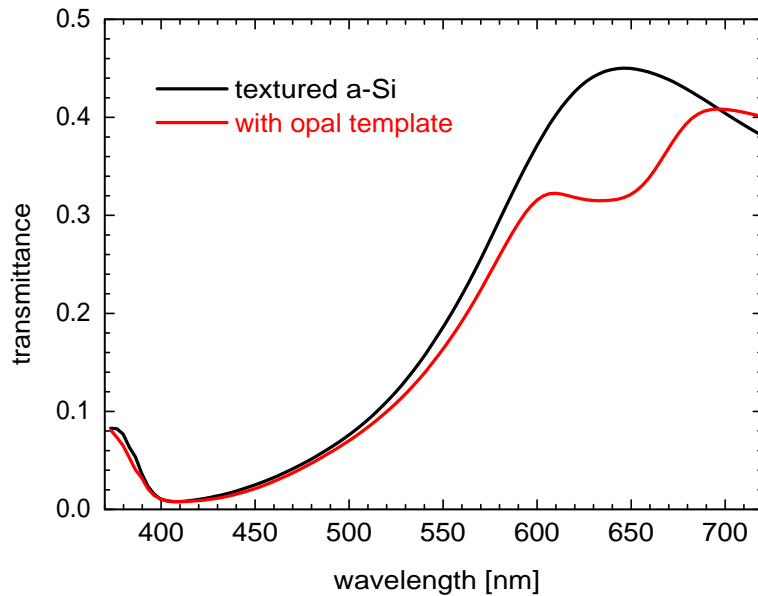


Figure 4.5: Transmission through textured a-Si sample, before and after deposition of an opal template ($d=300\text{nm}$) on the a-Si side (BX51, $M=20$). Absorption of 80nm a-Si:H is limiting T_{max} to about 50%.

PhC. Thus, the Bragg peak is asymmetrically widened by contributions of blue-shift.

4.4 The prototype

The processed IRL within the prototype cell has an average thickness of five layers. The film is of good quality, meaning a homogeneous thickness over large areas without macroscopic defects. A thicker PhC would deliver a stronger reflectance, but also must be expected to show worse electrical resistance. Therefore, only five layer instead of for example eight or ten have been grown for this experiment. Two major effects can be observed in the measured EQE of this prototype and have to be interpreted.

Firstly, the gap in performance between the fabricated prototype and standard cells is caused by the difference in light-trapping. The IRL-equipped cell is of planar type, while standards possess efficient light-trapping textures. The random rough texture of the front contact is capable of a more efficient harvest of light than the planar interfaces of the prototype. It has a higher η_{opt} , in terms of Eq.(1.40). This explains the overall reduction of 10%-20% of the prototype's EQE: the flat cell with the PhC suffers from front-side reflection losses and reduced absorbance over the whole absorption range. Here, the shown compatibility of random roughness and opal growth can provide a solution to this problem and will be investigated further. Also, the fabrication of special planar standards is an option to allow the identification of the IRL enhancement, as a proof of principle, under

experimental conditions that allow a valid comparison.

Secondly, the EQE measurement was performed with a small reverse bias voltage, which leads to the interpretation of a too large series resistance in the newly developed IRL. The intrinsic (or rather slightly n-doped) zinc oxide from ALD processing at very low temperatures forms nanocrystalline structures that can not compete with PECVD grown aluminum-doped bulk films in terms of conductivity. The exact conduction processes of the nano-structured material deposited here are not yet understood, but a further reduction of the resistance is necessary. Possible methods to achieve this are discussed in section 4.2.4.

It is important to note, that these very first experiments, the integration of a 3D photonic intermediate filter in a prototype solar cell and the successful measurement of its EQE, have shown the compatibility of the proposed PhC device with the micromorph thin-film technology. Also they underline two important device properties: the electrical conductivity of the IRL and the need for an highly efficient light-trapping component in the cell.

4.5 Compliance of results with requirements

The aim of this research to develop a photonic intermediate reflector has been reached. The developed photonic intermediate filter fulfills the ab-initio requirements, that have been defined in the first chapter, according to the following table.

Requirement, critical detail	Achieved results	Status
Reflectivity, high reflectance spectral selectivity spectral position current matching	>35%, tunable by thickness FWHM: 96 nm, base: 169 nm tunable, set to $\lambda_0 \approx 588$ nm surplus potential ('red' conf.)	(theor./exp.) ✓ (theor./exp.) ✓ (thero./exp.) ✓ (theor.) ✓
Transmittivity, transmittance 90% - 95%+ in spectral range for $\mu\text{c-Si}$?	>95%, integrated range: 700 nm - 1100 nm	(exp.) ✓ (exp.) ✓
Conductivity, tandem connection $R_{\text{irl}} < 2\Omega$ at 10 mA/cm^2	EQE measured $0.2 \Omega\mu\text{m} < R_{\text{spec.}} < 10 \Omega\mu\text{m}$ EQE bias voltage: $R \gg 2 \Omega$	(exp.) ✓ (pot.) \diamond (exp.) \boxtimes
Integration, consistent design process complete fabrication process process compatibility comp. to rough textures	BS, SMM, experiments match developed, established prototype: EQE -10%..-20% templates processed	(theor./exp.) ✓ (exp.) ✓ (exp.) ✓ (exp.) ✓

Tab.4.1: Status of requirements and achievements, theoretical and experimental

It shows the initial requirements and the solutions provided within this thesis. The actual status is either met (✓), partially met (\diamond) or unfulfilled (\boxtimes), distinguished between exper-

4 Discussion

imentally proven (exp.) and potentially at close range (pot.) according to calculation. The design process consequently follows the stages of the fabrication and can describe all observed optical effects with satisfying accuracy. The predicted optical properties of thin-film opals are observed at the produced samples without exception. Conductivity, however, is a critical issue. Although prototyping has not yet lead to the verification of an enhancement in comparison with state-of-the-art micromorph tandem cells, the very first working prototype cell with an integrated photonic IRL between the a-Si:H top cell and a silicon backside termination has successfully been fabricated. Thus, compatibility of the developed IRL with existing PV technology has been demonstrated.

5 Summary

The topic of this thesis is the development of photonic intermediate reflective layers for the micromorph tandem solar cell. This silicon tandem is composed of two cells, an a-Si:H front absorber and a $\mu c - Si$ bottom absorber. The absorption profiles of the series-connected cells at feasible thickness lead to an unbalanced distribution of the absorbed photon flux: the front cell produces a lower electrical current than the bottom cell which reduces the overall efficiency.

A three-dimensional thin-film photonic crystal has been investigated as an integrated reflector to optically match the current distribution by appropriate photon management between the two absorbers. The inverted opal PhC offers spectrally selective reflection and a high transmittance in the bottom cell illumination regime. With focus on the approach of Bragg-reflection aiming at the integration to random rough textured cells, the impact of diffraction from the PhC itself has not been investigated in full depth. The peculiarities of a 3D periodic device however, have been investigated with numerical methods of rigorous diffraction theory. In pre-design of infinite PhC via photonic band structure calculations, possible structural sizes of inv. opal IRL have been identified. Using a transparent conductive oxide of refractive index $n=1.7$, a sphere diameter between $d \approx 280nm$ and $d \approx 360nm$ matches the absorption profiles. The optical properties of finite PhC thin-films, on glass as well as in silicon, have been simulated. A first impact of the proposed device on the top cell performance has been estimated and working parameters (optical properties) of the reflectance profile have been obtained in current-matching calculations. To avoid the sensitivity of spectral parameters of the angle of incidence, a so-called 'red' configuration with spectral filtering with the spectral center regime of the Bragg-peak in reflectance at about $\lambda_0 = 675nm$ is preferred.

An analytical model of determining filling fractions for conformal deposition methods has been derived to correctly describe the produced samples after atomic layer deposition. To prepare for an in-situ monitoring of the growth processes, also composite samples have been investigated.

The fabrication of templates was based on a highly monodisperse colloidal suspension of $d = 300nm$. The infiltration and final inversion have been performed using low temperature CVD and ALD. Techniques to grow thin-film opals and the necessary equipment have been developed or improved. The structural properties of the inv. opal IRL have been investigated with SEM, confirming thickness and crystalline quality of the films. The ALD processed zinc oxide has been shown to be nano crystalline with a grain size in the order of magnitude of $10nm$.

The predicted optical features have been verified in microscopic and spectroscopic characterization. Reflectance amplitude and width can be altered within certain limits with the thickness of the layer and have been placed in the correct spectral regime. The functionality of the photonic IRL is not influenced significantly by the angle of incidence with appropriate design. In integrated transmission measurements the transmitted intensity

5 Summary

onto a bottom cell absorber has been quantified. The result shows outstanding transmission values of about 95% in the important red and NIR regime (700nm-1100nm).

For the first time, an integrated photonic IRL prototype has been fabricated at the back side of an a-Si:H top cell. It was finalized with a back silicon layer and back contact. The first spectral characterization (EQE) has been performed. Although the performance is 10%-20% below that of state-of-the-art tandem cells, the technological feasibility of the approach has been proven. The observed reductions in EQE are attributed to the planar interfaces in prototyping and are accompanied by insufficient conductivity of the photonic IRL so far. Consequently, electrical measurements have been performed at the IRL, showing rather high resistivities up to $10\Omega\mu m$. Finally, the combination of textured solar cells with the self-organized template growth processes have been investigated. The compatibility of the different processes was tested, and it has been shown that the applied methods of self-organized growth can be combined with the randomly textured light-trapping structure of the micromorph tandem cell: The first optical measurement of templates on rough solar cells reveal a well-developed photonic stop gap.

The development and investigation of a novel 3D photonic intermediate layer for photon management in thin-film silicon tandem solar cells has shown the very promising potential of this approach in theory and experiment and has also proven the compatibility with existing processes in photovoltaic cell fabrication.

6 Outlook

After the first integration of a 3D PhC intermediate reflector has been successfully performed, the improvement of processes and prototypes will follow. After having shown the potential and feasibility of this approach, experimental proof of an increase in the EQE and tandem efficiency is the aim of future work.

The influence of diffuse transmission from partially disordered PhC films on bottom cell absorption can be addressed with computational methods and in experiments. Especially the combination of the highly efficient textured superstrates (FZJ) with thickness-optimized PhC films will be an important experimental step, since the best available light trapping component is crucial to an efficient solar cell. Tailoring of such interfaces is accessible via the monodispersity of colloidal suspensions, while the mean sphere diameter defines the spectral range of filtering. The resulting combined texture-lighttrapping/inverted opal IRL tandem will have an additional diffusive layer - the amorphous colloidal phase close to the texture. This diffusor can be expected to broaden the angular distribution of light transmitted into the bottom cell. Consequently, the optical path in $\mu c - Si$ will increase, which allows to reduce the bottom cell thickness. So, this IRL would also fulfill one task of a backside diffusor or backside diffraction grating.

A strong motivation for further research on 3D PhC interlayers is the contribution of diffraction. Only of minor importance for the approach focused on Bragg-reflection, the diffraction at the photonic crystal lattice planes at larger sphere radii can excite guided modes in the a-Si:H top cell and generally produce high diffraction angles. This can allow for a reduction of the thickness of the a-Si:H absorber, a consequence of enlarged optical paths inside the absorbing layer. The electrical properties (e.g. small diffusion length) of a-Si:H make thinner cells favorable. Interesting will also be the issue of the required thickness of inverted opal films for such a purely diffractive application. Therefore, the diffraction efficiencies and angular distributions of light will be investigated.

The issue of conductivity will be addressed with in-situ doping of the so far intrinsic ZnO for the inverted opal films or via post-processing. Also, the contact grid approach can be used with follow-up (CVD-mode) reinforcement of the processed PhC. Alternative materials and liquid phase methods can be explored in order to find additional methods of large scale fabrication. Up-scaling of the methods and processes so far will initially focus on sizes of $100\text{ mm} \times 100\text{ mm}$, which can be considered as mini-modules.

A Acknowledgements

Here I would like to acknowledge the persons and entities, who supported my work during the preparation of this thesis.

My grateful thanks to

Prof. Ralf Wehrspohn, for the opportunity to work on this fascinating topic, for his unrivaled motivation, and for his confidence in me to handle scientific challenges

Dr. Reinhard Carius, for his unique questions and answers, and for keeping track

Dr. Paul Miclea, for his teachings, patience and invaluable knowledge about SEM

Dr. Carsten Rockstuhl, for many fruitful discussions and his outstanding work on the theoretical part of our projects

Dr. Andreas von Rhein, for his rare problem solving attitude of a giant in the playground

Dr. Mato Knez and Seung-Mo Lee from the ALD crew of MPI at Halle, for introducing me to ALD and for their time and effort spent on my crystals

Dr. Karsten Bittkau, for teaching me his pool of tricks in optical near-field microscopy

Johannes Üpping, for his encouraging support, for unlimitedly firing the right questions at me, and for our brilliant teamworking-efficiency of $\eta_{LP} = 1.01$

Marius Peters, for his efforts with EIS, our OHS concept, and the many levels of challenging monday evening discussions

my colleagues at both universities, Halle and Paderborn, for the motivating inducement and releasing disport, but especially Claudia Stehr for her commitment to the polymerization process, and the Swiss Guard who shared my delocalization

my colleagues in the DFG and BMBF research projects "nanoSun" and "nanoVolt" at Oldenburg, Aachen, Jülich, Paderborn, Jena, Halle, Mainz, Stuttgart, and Freiburg for the lively project work and, fair enough, 'because I can',
special thanks go to Prof. Rudolf Zentel, Lorenz Steidl and Dr. Birger Lange for the cheerful research visits and our joint missions on tiny plastic beads

I gratefully acknowledge the financial support by the German Science Foundation (Deutsche Forschungsgesellschaft DFG) within *Pak 88*.

B Optical Properties: Technical Details

Beside the important features and results discussed within the presented thesis, there are some additional aspects of the optical properties that should be mentioned. The amplitudes of reflection, the numerical aperture in any optical measurement on opal samples and their impact on the presented experimental data are addressed in this appendix for sake of completeness.

B.1 Measured amplitudes of reflection

The inverted opal samples do not perform as well as the theoretical ones in terms of reflection amplitudes of the bragg peak. The numerical aperture of the used spectrometer setup (section 2.1.2) is very small (typically about $NA=0.01$). Thus, the light collected by the optical fiber contains only the specular part with negligible diffuse contributions. An undefined but probably rather small share of intensity is also caught by the substrate (in case of glass): illuminated samples are typically dimly lit along the sides. The light is diffracted or scattered into the microslide glass and some of it is guided by internal reflection within the glass plate towards the edges. The measured amplitudes are consequently lower than expected from the (halfspace) simulations, which contain all the reflected light from a half-space.

Effects of the numerical aperture are treated in detail in the following section B.2.

B.2 Effects of numerical aperture

In general, results that are obtained from optical investigations of artificial opal samples have to be checked for effects of the numerical aperture (NA), since photonic crystals are angle-sensitive optical devices.

Placing an opaline sample in an optical microscope and measuring the reflection spectra with different numerical apertures, we can observe an increase in reflectivity as the NA is increased. In general this is expected, since the field of view (FOV) of our instrument will be enlarged if the NA is set to higher values. In consequence we collect contributions of diffusely (non-specularly) reflected light from the sample which is added to the specular reflectivity. The amount of scattered light that reaches the aperture of our objective increases, as a larger area of the sample fills our FOV.

Contributions from large angles (edges of the FOV) leave the opal at angles, that are no longer related to the ΓL direction: they will experience blue shift and might even leave the angular range of the main stop gap! The angular behavior of the crystal (as already

discussed with the band structure) dominates the NA effects, when higher angles are involved. This leads to a measurable decrease in the normalized reflectivity of a sample, if viewed at with a high enough numerical aperture. From microscopic investigations and bandstructure calculations for inverted opals, we do not expect significant blue shift and may perform measurements of opal samples (at normal incidence) up to a numerical aperture of at least $NA \leq 0.3$ (mostly up to $NA \leq 0.45$) without the need to take spectral NA effects into account. This is backed up by the experimental results reported by Lee [96]. The influence of the NA on the reflectance amplitude, however, strongly depends on the crystalline and optical qualities of the individual PhC sample, which is decisive for the ratio of diffusing behaviour, as described above.

As an important conclusion, the use of higher NA can bear some representation of the difference between specular and half-angle optical properties. Very low NA have been used for high precision, e.g. in angular measurements, while larger NA (microscope) were chosen for general spectra and for comparison. The difference for an inverted opal film is shown in Fig.4.3.

B.3 Reflectance and transmittance

With more than 35% of reflectance from 8 layers of ZnO inverted opal, there is already excess reflectance for the proposed ‘red’ configuration which required about 25% (see section 3.1.5) at comparable spectral width. Adjustment of the PhC film thickness will tune the reflectance (peak height and spectral width) to the desired magnitude easily. In consequence, the spectral filtering can be considered more than sufficient.

The integrated transmittance measurement does not suffer from any NA effect and therefore results in more representative spectra of transmission, containing the specular and diffuse shares. Measurements of the specular properties are nevertheless well suited for the characterization because the ratio of specular and diffuse transmission and reflection is related to film quality and imperfections of the PhC.

C Publications and Presentations

C.1 Publications related to this thesis

A. Bielawny, P.-T. Miclea, A. v. Rhein, R. B. Wehrspohn, S. van Riesen, S. Glunz,
Dispersive elements for spectrum splitting in solar cell applications. Proc. SPIE 6197,
619704 (2006)

A. Bielawny, P.-T. Miclea, R.B. Wehrspohn, A. v. Rhein, C. Rockstuhl, M. Lisca, F. L.
Lederer B. Lange, R. Zentel, and R. Carius,
Diffraction and energy-selective photonic crystals for thin-film tandem solar cells. Photo-
voltaic cell and module technologies, Proc. SPIE 6651, 665106 (2007)

R. B. Wehrspohn, A. Bielawny, C. Rockstuhl, F. Lederer,
*3D Photonic Crystals as Diffraction and Energy Selective Filter for Tandem Thin Film
Solar Cells,* Conf. Proc. MRS spring meeting, 1014-AA05-01 (2007)

A. Bielawny, P.-T. Miclea, R.B. Wehrspohn, S. M. Lee, M. Knez, C. Rockstuhl, M. Lisca,
F. L. Lederer and R. Carius,
Three-dimensional photonic crystals as intermediate filter for thin-film tandem solar cells.
Photonics for Solar Energy Systems II , Proc SPIE 7002, 700208 (2008)

K. Bittkau, R. Carius, A. Bielawny, and R. B. Wehrspohn,
*Influence of defects in opal photonic crystals on the optical transmission imaged by near-
field scanning optical microscopy.* J. Mater. Sc.: Mater Electron (2008).

A. Bielawny, J. Üpping, Paul T. Miclea, R. B. Wehrspohn, C. Rockstuhl, F. Lederer, M.
Peters, L. Steidl, R. Zentel, S. Lee, M. Knez, A. Lambertz and R. Carius,
3D photonic crystal intermediate reflector for micromorph thin-film tandem solar cell,
Phys. Stat. Solidi A, 205, 2796-2810 special issue on Photonmanagement in Solar Cells,
(2008).

A. Bielawny, R. Wehrspohn, C. Rockstuhl, and F. Lederer,
Intermediate reflectors for enhanced top cell performance in photovoltaic tandem cells,
Opt. Expr., 17(10), 8439-8446, (2009).

A. Bielawny, J. Üpping, and R. Wehrspohn,
Spectral properties of intermediate reflectors in micromorph tandem cells, to be published:
Solar Energy Materials and Solar cells, (2009)

C.2 Selected talks and posters

70. Frühjahrstagung der Deutschen Physikalischen Gesellschaft,
March 26.-30. 2006, Dresden (Germany)

Manufacture of photonic crystals for photovoltaic applications

SPIE Photonics Europe 2006, Strasbourg, France

Dispersive elements for spectrum splitting in solar cell applications

71. Frühjahrstagung der Deutschen Physikalischen Gesellschaft March 26.-30. 2007, Regensburg (Germany), *Spectrally Selective Photonic Structures for Photovoltaic Applications*

SPIE Optics and Photonics August 26.-30. 2007, San Diego, CA, USA *Diffraction and energy selective photonic crystals for thin-film tandem solar cells*

398. Wilhelm-und-Else Heräus Seminar: Photonmanagement in Solar cells, October 29.-November 1. 2007 Bad Honnef, Germany

Poster: Spectrally Selective Photonic Structures For Photovoltaic Applications

72. Frühjahrstagung der Deutschen Physikalischen Gesellschaft, February 25.-29. 2008, Berlin (Germany)

Photonic intermediate layer for silicon tandem solar cells

SPIE Photonics Europe 2008, April 6.-10. 2008, Strasbourg, France

Three-dimensional photonic crystal as intermediate filter for thin-film tandem solar cells

D Curriculum Vitae

Personal

Family name:	Bielawny
First name:	Andreas
Date of birth:	March 30, 1979
Place of birth:	Paderborn, Germany
Citizenship:	German
Family status:	Married, one daughter
e-mail:	Andreas.Bielawny@physik.uni-halle.de A.Bielawny@gmx.de

Educational and professional

Aug. 1989 to Jun. 1998	Secondary school Gymnasium Theodori- anum, Paderborn, Germany
Oct. 1998 - Jul. 1999	Military Service, 21st Armored Brigade, Germany
Oct. 1999 to Sep. 2001	undergraduate courses in physics (Vordiplom), University of Paderborn, Germany
Oct. 2001 to Sep. 2003	adv. courses in physics, University of Paderborn
Sep. 2003 to Sep. 2004	Master's thesis (Diplomarbeit) on <i>Disper- sive structures for tandem solar cell sys- tems</i> , University of Paderborn
Oct. 2004 to Dec. 2004	Assistant employment for spectroscopy and irradiation experiments, University of Paderborn
Jan. 2005 to Dec. 2008	PhD thesis on <i>photonic crystal intermedi- ate reflectors for tandem solar cells</i> , Uni- versity of Paderborn and Martin-Luther- Universität Halle-Wittenberg (Germany)
Jan. 2009 -	Optical Engineering, Brandenburg- GmbH, Paderborn, Germany

E Eidesstattliche Erklärung

Ich erkläre hiermit an Eides Statt, dass ich die vorgelegte Arbeit selbstständig und ohne Benutzung anderer als der angegebenen Hilfsmittel und Quellen angefertigt habe. Die aus fremden Quellen übernommenen Inhalte und Beiträge zu dieser Arbeit sind als solche kenntlich gemacht. Diese Arbeit wurde zuvor noch keiner anderen Prüfungskommission vorgelegt.

.....

Andreas Bielawny

E Eidesstattliche Erklärung

Bibliography

- [1] P. Würfel. *Physik der Solarzellen*, volume 2. Spektrum Akademischer Verlag GmbH, Heidelberg, Berlin, 2000.
- [2] M. A. Green. *Third Generation Photovoltaics*. Springer, Berlin, 2003.
- [3] A. Luque, S. Hegedus, X. Deng, and E. A. Schiff. *Handbook of Photovoltaic Science and Engineering*. John Wiley & Sons, Ltd, London, 2003.
- [4] Fuchs, Stiebig, and Reber. Dünnschicht-solarzellen aus silicium. FVS Themen 2003, HMI Berlin, 2003.
- [5] A. W. Bett, C. Baur, F. Dimroth, G. Lange, M. Meusel, S. van Riesen, G. Siefer, V. M. Andreev, V. D. Rumyantsev, and N. A. Sadchikov. Flatcon-modules: technology and characterisation. In *Photovoltaic Energy Conversion, 2003. Proceedings of 3rd World Conference on*, volume 1, pages 634– 637. IEEE, May 2003.
- [6] M Green, K. Emery, Y. Hisikawa, and Warta W. Solar cell efficiency tables (v.30). *Prog. Photovolt: Res. Appl.*, 15:425–430, 2007.
- [7] J. Zhao, A. Wang, M. Green, and F. Ferrazza. Novel 19.8% efficient honeycomb textured multicrystalline and 24.4% monocrystalline silicon solar cell. *Appl. Phys. Lett.*, 73:1991–1993, 1998.
- [8] W. Shockley and H. J. Queisser. Detailed balance limit of efficiency of p-n junction solar cells. *J. Appl. Phys.*, 32:510–519, 1961.
- [9] T. Trupke, M. A. Green, and P. Würfel. Improving solar cell efficiencies by up-conversion of sub-band-gap light. *J. Appl. Phys.*, 92:4117, 2002.
- [10] T. Trupke, M. A. Green, and P. Würfel. Improving solar cell efficiencies by down-conversion of high-energy photons. *J. Appl. Phys.*, 92:1668, 2002.
- [11] D. B. Bushnella, N. J. Ekins-Daukes, K. W. J. Barnham, J. P. Connolly, J. S. Roberts, G. Hill, R. Airey, and M. Mazzer. Short-circuit current enhancement in bragg stack multi-quantum-well solar cells for multi-junction space cell applications. *Sol. Energy Mater. Sol. Cells*, 75:299–305, 2003.
- [12] B. Ahrens, C. Eisenschmidt, J. A. Johnson, P. T. Miclea, and S. Schweizer. Structural and optical investigations of nd-doped fluorozirconate-based glass ceramics for enhanced upconverted fluorescence. *Appl. Phys. Lett.*, 92:061905, 2008.
- [13] I. Tobias and A. Luque. Ideal efficiency of monolithic, series-connected multijunction solar cells. *Prog. Photovolt: Res. Appl.*, 10:323–329, 2002.

Bibliography

- [14] R. L. Moon, L. Wl. James, H. A. Vander Plas, T. O. Yep, G. A. Antypas, and Y. Chai. Multigap solar cell requirements and the performance of algaas and si cells in concentrated sunlight. In *Conference Record of the 13th Photovoltaic Specialists Conference, Whashington, 1978*, number 17-44 in A79-40881, pages 859–867. New York, Institute of Electrical and Electronics Engineers, Inc., U.S. Department of Energy, June 1978.
- [15] S. Fahr, C. Ulbrich, T. Kirchartz, U. Rau, C. Rockstuhl, and F. Lederer. Rugate filter for light-trapping in solar cells. *Opt. Expr.*, 16(12):9332, June 2008.
- [16] J. Müller, G. Schopel, B. Rech, H. Schade, P. Lechner, R. Geye, H. Stiebig, and W. Reetzl. Role of the glass/tco substrate in thin film silicon solar cells. In *Photovoltaic Specialists Conference, 13th, Washington, D.C., Conference Record on*, volume 5P-D4-3 1. Photovoltaic Energy Conversion, 3rd World Conference on, May, 11-18 2003. Poster: 1839.
- [17] K. R. Catchpole and M. A. Green. A conceptual model of light coupling by pillar diffraction gratings. *J. Appl. Phys.*, 101:063105, 2007.
- [18] H. Nagel, A. G. Aberle, and R. Hezel. Optimised antireflection coatings for planar silicon solar cells using remote pecvd silicon nitride and porous silicon dioxide. *Prog. Photovolt: Res. Appl.*, 7:245–260, 1999.
- [19] S. Lo, C. Chen, F. Garwe, and T. Pertsch. Broad-band anti-reflection coupler for a : Si thin-film solar cell. *J. Phys. D: Appl. Phys.*, 40:754–758, 2007.
- [20] S. Fahr, C. Rockstuhl, and F. Lederer. Engineering the randomness for enhanced absorption in solar cells. *Appl. Phys. Lett.*, 92:171114, 2008.
- [21] C. Rockstuhl, F. Lederer, K. Bittkau, and R. Carius. Light localization at randomly textured surfaces for solarcell applications. *Appl. Phys. Lett.*, 91:171104, 2007.
- [22] C. Wu, C. H. Crouch, L. Zhao, J. E. Carey, R. Younkin, J. A. Levinson, E. Mazur, R. M. Farrell, P. Gothoskar, and A. Karger. Near-unity below-band-gap absorption by microstructured silicon. *Appl. Phys. Lett.*, 78(13):1850–1852, March 2001.
- [23] J. Üpping, A. Bielawny, P. T. Miclea, and R. B. Wehrspohn. 3d photonic crystals for ultra-light trapping in solar cells. In A. Gombert, editor, *Opt. Eng. Proceedings of SPIE 0277-786X*, number 7002-01. SPIE Photonics Europe, 2008.
- [24] H. Stiebig, y, N. Senoussaoui, C. Zahren, C. Haase, and J. Müller. Silicon thin-film solar cells with rectangular-shaped grating couplers. *Prog. Photovolt: Res. Appl.*, 14:13–24, 2006.
- [25] N. Feng, J. Michel, L. Zeng, J. Liu, C. Hong, L. C. Kimerling, and X. Duan. Design of highly efficient light-trapping structures for thin-film crystalline silicon solar cells. *Electron Devices, IEEE Transactions on*, 54(8):1926–1933, Aug. 2007.
- [26] H.F.Sterling R.C. Chittick, J.H. Alexander. The preparation and properties of amorphous silicon. *J. Electrochem. Soc.*, 116:77, 1969.
- [27] J. I. Pankove and D. E. Carlson. Electrical and optical properties of hydrogenated amorphous silicon. *Annu. Rev. Mater. Sci.*, 10:43–63, 1980.

- [28] S. Klein, L. Houben, R. Carius, F. Finger, and W. Fische. Structural properties of microcrystalline sic deposited at low substrate temperatures by hwcvd. *J. Non-Crystal. Sol.*, 352:1376–1379, 2006.
- [29] T. Chen, Y. Huang, D. Yang, R. Carius, and F. Finger. Microcrystalline silicon-carbon alloys as anti-reflection window layers in high efficiency thin film silicon solar cells. *phys. stat. sol. (RRL)*, 2:160–162, 2008.
- [30] D. L. Staebler and C. R. Wronski. Reversible conductivity changes in discharge-produced amorphous si. *Appl. Phys. Lett.*, 31:292, 1977.
- [31] H. Keppner, J. Meier, P. Torres, D. Fischer, and A. Shah. Microcrystalline silicon and micromorph tandemsolar cells. *Appl. Phys. A*, 69:169–177, 1999.
- [32] A. V. Shah, J. Bailat, E. Vallat-Sauvain, M. Vanecek, J. Meier, S. Fay, L. Feitknecht, I. Pola, V. Terrazzoni, and C. Ballif. Microcrystalline and micromorph solar cells and modules: Status and potential. In *Proc. of the 31th IEEE Photovoltaic Specialist Conference*, pages 1353–1358, January 2005. Lake Buena Vista, FL, USA.
- [33] U. Kroll. Abscheidung von zno-schichten mittels der lpcvd-technik für die anwendung in der dünn-schicht-photovoltaik. FVS Workshop, Session III, 2005.
- [34] Sang Jik Kwon and Hyun Jae Lee. Variation in the properties of zno:al films grown by using atomic layer deposition with the precursor-pulse ratio. *Journal of the Korean Physical Society*, 43(5):709–713, November 2003.
- [35] M. J. Alam and D. C. Cameron. Preparation and properties of transparent conductive aluminium-doped zinc-oxide film by sol-gel process. *J. Vac. Sc. Techn.*, 19(4):1642, 2001.
- [36] A. de Vos. Detailed balance limit of the efficiency of tandem solar cells. *J. Phys. D: Appl. Phys.*, 12:839–846, 1980.
- [37] A. Gregg, T. Parker, and R. Swenson. A real world examination of pv systems design and performance. In *Photovoltaic Specialists Conference, 2005. Conference Record of the 31st IEEE*, pages 1587–1592. IEEE, 2005.
- [38] T. Roschek, J. Müller, S. Wieder, B. Rech, and H. Wagner. High rate deposition of microcrystalline silicon solar cells using 13.56 mhz. In *Proceedings of the 28th IEEE Photovoltaic Specialists Conference*, pages 150 – 153. IEEE, September 2000.
- [39] T. Repmann, J. Kirchhoff, W. Reetz, F. Birmans, J. Müller, and B. Rech. Investigations on the current matching of highly efficient tandem solar cells based on on amorphous and microcrystalline silicon. In *Proceedings of 3rd World Conference on Photovoltaic Energy Conversion*, volume 2, pages 1843–1846, 2003.
- [40] J. Meier, U. Kroll, J. Spitznagel, S. Benagli, A. Huegli, T. Roschek, C. Ellert, M. Pop-peller, G. Androustopoulos, D. Borello, W. Stein, O. Kluth, M. Nagel, C. Bucher, L. Feitknecht, G. Buechel, J. Springer, and A. Buechel. Amorphous silicon single-junction and micromorph tandem solar cells prepared in unaxis kai pecvd single-chamber reactors. In *Proceedings of the 20th EU Photovoltaic Solar Energy Conference*, pages 503–508, June 2005.

Bibliography

- [41] K. Yamamoto, A. Nakajima, M. Yoshimi, T. Sawada, S. Fukuda, T. Suezaki, M. Ichikawa, Y. Koi, M. Goto, T. Meguro, T. Matsuda, T. Sasaki, and Y. Tawada. High efficiency thin film silicon hybrid cell and module with newly developed innovative interlayer. *Photovoltaic Energy Conversion, Conference Record of the 2006 IEEE 4th World Conference on*, 2:1489–1492, 2006.
- [42] D. Dominé, J. Steinhauser, L. Feitknecht, A. Shah, and C. Ballif. Effect of zno layer as intermediate reflector in micromorph solar cells. In *Proceedings of the 20th EU Photovoltaic Solar Energy Conference, Barcelona, Spain*, pages 1600–1603, 2005.
- [43] D. Dominé, J. Steinhauser, L. Feitknecht, A. Shah, and C. Ballif. Effect of zno layer as intermediate reflector in micromorph solar cells. *Photovoltaic Energy Conversion, Conference Record of the 2006 IEEE 4th World Conference on*, 3:1465–1468, 2006.
- [44] D. Dominé, J. Bailat, J. Steinhauser, A. Shah, and C. Balli. Micromorph solar cell optimization using a zno layer as intermediate reflector. In *Proceedings of the 4th WCPEC Conference*, pages 1465–1468, 2006. , Kona Island, Hawaii, USA, pp. 1465-1468, 2006.
- [45] F.-J. Haug, V. Terrazoni-Daudrix, T. Söderström, X. Niquille, and C. Ballif. Development of micromorph tandem solar cells on flexible low cost plastic substrates. In *17th International Photovoltaic Solar Energy Conference, Fukuoka, Japan*, 2007.
- [46] J. Krc, F. Smole, and M. Topic. Advanced optical design of tandem micromorph silicon solar cells. *J. Non-Cryst. Sol.*, 352:1892.1895, 2006.
- [47] K. Busch and S. John. Photonic band gap formation in certain self-organizing systems. *Phys. Rev. E*, 58(3):3896, 1998.
- [48] J. Joannopoulos. *Photonic Crystals*. Princeton University Press, 1995.
- [49] Sakoda. *Optical Properties of Photonic Crystals*. Springer, Berlin, 2001.
- [50] J. C. Maxwell. A dynamical theory of the electromagnetic field. *Philosophical Transactions of the Royal Society of London*, 155:459–512, 1865.
- [51] J. Üpping. Ultra light trapping with 3d photonic crystals for thin film solar cells. Master’s thesis, University of Paderborn, Sep. 2007.
- [52] Abrarov. Equations for filling factor estimation in opal matrix. *Opt. Commun.*, 259(1):378–384, 2006. arXiv:physics/0508152v1 (Addendum to the article).
- [53] J. F. Galisteo-Lopez, M. Galli, M. Patrini, A. Balestreri, L. C. Andreani, and C. Lopez. Effective refractive index and group velocity determination of three-dimensional photonic crystals by means of white light interferometry. *Phys. Rev. E*, 73:125103, 2006.
- [54] P. A. Hiltner and I. M. Krieger. Diffraction of light by ordered suspensions. *J. Phys. Chem.*, 73(7):2386–2389, July 1969.
- [55] R. M. De La Rue M. A. McLachlan, N. P. Johnson and D. W. McComb. Domain size and thickness control of thin film photonic crystals. *Journal of Materials Chemistry*, 15:369–371, 2004.

- [56] J. Vermant and M. J. Solomon. Flow-induced structure in colloidal suspensions. *J. Phys: Condens. Matter*, 17:R187–R216, 2005. A large REVIEW on flow induced structuring in colloidal suspensions. very interesting, but ”beyond the scope”.
- [57] S. H. Park and Y. Xia. Assembly of mesoscale particles over large areas and its application in fabricating tunable optical filters. *Langmuir*, 15:266–273, 1999.
- [58] Y. Ye, F. LeBlanc, A. Hache, and V. Truong. Self-assembling three-dimensional colloidal photonic crystal structure with high crystalline quality. *Appl. Phys. Lett.*, 78(1):52, 2001.
- [59] M. Allarda and E. H. Sargent. Impact of polydispersity on light propagation in colloidal photonic crystals. *Appl. Phys. Lett.*, 85 (24):5887–5889, 2004.
- [60] M. Egen and R. Zentel. Tuning the properties of photonic films from polymer beads by chemistry. *Chem. Mater.*, 14:2176–2183, 2002.
- [61] M. Egen, R. Voss, B. Griesebock, R. Zentel, S. Romanov, and C. Sotomayor-Torres. Heterostructures of polymer photonic crystal films. *Chem. Mater.*, 15(20):3786–3792, 2003.
- [62] F. Fleischhaker and R. Zentel. Photonic crystals from core-shell colloids with incorporated highly fluorescent quantum dots. *Chem. Mater.*, 17:1346–1351, 2005.
- [63] Y. Ye, T. S. Mayer, I. Khoo, I. B. Divliansky, N. Abrams, and T. E. Mallouk. Self-assembly of three-dimensional photonic-crystals with air-core line defects. *J. Mater. Chem*, 12:2637–3639, 2002.
- [64] J. F. Galisteo-Lopez, E. Palacios-Lidon, E. Castillo-Martinez, and C. Lopez. Optical study of the pseudogap in thickness and orientation controlled artificial opals. *Phys. Rev. E*, 68:115109–1, 2003.
- [65] J. F. Galisteo-Lopez and W. L. Vos. Angle-resolved reflectivity of single-domain photonic crystals: Effects of disorder. *Phys. Rev. E*, 66:036616, 2002.
- [66] J. F. Bertone, P. Jiang, K. S. Hwang, D. M. Mittleman, and V. L. Colvin. Thickness dependence of the optical properties of ordered silica-air and air-polymer photonic crystals. *Phys. Rev. Lett.*, 83(2):300–303, 1999.
- [67] N. V. Dziomkina and G. J. Vancso. Colloidal crystal assembly on topologically patterned templates. *Soft Matter*, 1:265–279, 2005.
- [68] Mariko Yamaki, Junichi Higo, and Kuniaki Nagayama. Size-dependent separation of colloidal particles in two-dimensional convective self-assembly. *Langmuir*, 11:2975–2978, 1995.
- [69] A. S. Dimitrov and K. Nagayama. Continuous convective assembling of fine particles into two-dimensional arrays on solid surfaces. *Langmuir*, 12:1303–1311, 1996.
- [70] E. von Rhein, A. Bielawny, and S. Greulich-Weber. Control of colloidal crystal growth by external fields. In *Mater. Res. Soc. Symp. Proc.*, volume 901E. MRS, 2006.

Bibliography

- [71] L. A. Villaescusa, A. Mihi, I. Rodriguez, A. E. Garcia-Bennett, and H. Miguez. Growth of mesoporous materials within colloidal crystal films by spin-coating. *J. Phys. Chem. B*, 109:19643–19649, 2005.
- [72] A. Mihi, M. Ocana, and H. Miguez. Oriented colloidal-crystal thin films by spin-coating microspheres dispersed in volatile media. *Adv. Mater.*, 18:2244–2249, 2006.
- [73] J Johnson, Steven G. Joannopoulos. Block-iterative frequency-domain methods for maxwell’s equations in a planewave basis. *Opt. Expr.*, 8:173–190, 2001.
- [74] I. Rodriguez, P. Atienzar, F. Ramiro-Manzano, F. Meseguer, A. Corma, and H. Garcia. Photonic crystals for applications in photoelectrochemical processes photoelectrochemical solar cells with inverse opal topology. *Photonics and Nanostruct. Ú Fundam. and Appl.*, 3:148–154, 2005.
- [75] A. Rugge, J. S. Becker, R. G. Gordon, and S. H. Tolbert. Tungsten nitride inverse opals by atomic layer deposition. *Nano Lett.*, 3(9):1293–1297, 2003.
- [76] M. Scharrer, X. Wu, A. Yamilov, H. Cao, and R. P. H. Chang. Fabrication of inverted opal zno photonic crystals by atomic layer deposition. *Appl. Phys. Lett.*, 86:151113, 2005.
- [77] D. P. Gaillot and C. J. Summers. Photonic band gaps in non-close-packed inverse opals. *J. Appl. Phys.*, 100:113118, 2006.
- [78] J. F. Galisteo, F. Garcia-Santamaria, D. Golmayo, B. H. Juarez, C. Lopez, and E. Palacios. Self-assembly approach to optical metamaterials. *J. Opt.*, 7:S244–S254, 2005. impressive review on self organized systems and their properties!
- [79] Yu. A. Vlasov, M. Deutsch, and D. J. Norriss. Single-domain spectroscopy of self-assembled photonic crystals. *Appl. Phys. Lett.*, 76:1627, 2000.
- [80] E. Pavarini, L. C. Andreani, C. Soci, M. Galli, and F. Marabelli. Band structure and optical properties of opal photonic crystals. *Phys. Rev. B*, 72:045102, 2005.
- [81] F. Garcia-Santamaria, J. F. Galisteo-Lopez, P V. Braun, and C. Lopez. Optical diffraction and high-energy features in three-dimensional photonic crystals. *Phys. Rev. B*, 71:195112, 2005.
- [82] R. V. Nair and R. Vijaya. Observation of higher-order diffraction features in self-assembled photonic crystals. *PhysRev. A*, 76:053805, 2007.
- [83] M. Centini, C. Sibilia, M. Scalora, G. DAguanno, M. Bertolotti, M. J. Bloemer, C. M. Bowden, and I. Nefedov. Dispersive properties of finite, one-dimensional photonic band gap structures: Applications to nonlinear quadratic interactions. *Phys. Rev. E*, 60:4891, 1999.
- [84] P. Jiang, J. F. Bertone, K. S. Hwang, and V. L. Colvin. ”single-crystal colloidal multilayers of controlled thickness”. *Chem. Mater.*, 11:2132, 1999.
- [85] Sang Hyuk Im, Mun Ho Kim, and O Ok Park. ”thickness control of colloidal crystals with a substrate dipped at a tilted angle into a colloidal suspension”. *Chem. Mater.*, 15:1797, 2003.

- [86] Z. Gu, A. Fujishima, and O. Sato. Fabrication of high-quality opal films with controllable thickness. *Chem. Mater.*, 14:760, 2002.
- [87] R. L. Puurunen. Surface chemistry of atomic layer deposition: A case study for the trimethylaluminum/water process. *J. Appl. Phys.*, 97:121301, 2005.
- [88] J. Turunen. *Diffraction Theory of Microrelief Gratings, Micro-Optics: Elements systems and applications*, chapter 2, pages 31–52. H. P. Herzig, 1997.
- [89] S. F. Su and T. K. Gaylord. Calculation of arbitrarily diffraction efficiencies of thick gratings with arbitrary shape. *J. Opt. Soc. Am.*, 65:59.64, 1975.
- [90] M. G. Moharam and T. K. Gaylord. Rigorous coupled-wave analysis of planar-grating diffraction. *J. Opt. Soc. Am.*, 71:811–818, 1981.
- [91] D. M. Whittaker and I. S. Culshaw. Scattering-matrix treatment of patterned multi-layer photonic structures. *Phys. Rev. B*, 60:2610, 1999.
- [92] K. Bittkau, R. Carius, A. Bielawny, and R. B. Wehrspohn. Influence of defects in opal photonic crystals on the optical transmission imaged by near-field scanning optical microscopy. *J. Mater. Sc.: Mater Electron*, 2008.
- [93] A. Bielawny, C. Rockstuhl, F. Lederer, and R. B. Wehrspohn. Intermediate reflectors for enhanced top cell performance in photovoltaic thin-film tandem cells. *Opt. Expr.*, 17(10):8439–8446, 2009.
- [94] I. V. Tudose, P. Horvath, M. Sucheai, S. Christoulakis, T. Kitsopolous, and G. Kiriakidis. Correlation of zno thin film surface properties with conductivity. *Apl. Phys. A*, 89:57–61, June 2007.
- [95] N. Golego, S. A. Studenikin, and M. Cocivera. Sensor photoresponse of thin-film oxides of zinc and titanium to oxygen gas. *J. Electrochem. Soc.*, 147(4):1592–1594, December 1999.
- [96] Y. Lee, S. A. Pruzinsky, and P. V. Braun. Diffraction response of colloidal crystals: effect of numerical aperture. *Opt. Lett.*, 30:153, 2005.